DAMAGE INITIATION AND POST-DAMAGE RESPONSE OF COMPOSITE LAMINATES BY MULTIAXIAL TESTING AND NONLINEAR OPTIMIZATION

by

James Tyler Schmitt

A thesis submitted in partial fulfillment
of the requirements for the degree

of

Master of Science

in

Mechanical Engineering

MONTANA STATE UNIVERSITY
Bozeman, Montana

November 2008

APPROVAL

of a thesis submitted by

James Tyler Schmitt

This thesis has been read by each member of the thesis committee and has been found to be satisfactory regarding content, English usage, format, citation, bibliographic style, and consistency, and is ready for submission to the Division of Graduate Education.

Dr. Douglas S. Cairns

Approved for the Department of Mechanical & Industrial Engineering

Dr. Christopher H.M. Jenkins

Approved for the Division of Graduate Education

Dr. Carl A. Fox

STATEMENT OF PERMISSION TO USE

In presenting this thesis in partial fulfillment of the requirements for a master's degree at Montana State University, I agree that the Library shall make it available to borrowers under rules of the Library.

If I have indicated my intention to copyright this thesis by including a copyright notice page, copying is allowable only for scholarly purposes, consistent with "fair use" as prescribed in the U.S. Copyright Law. Requests for permission for extended quotation from or reproduction of this thesis in whole or in parts may be granted only by the copyright holder.

James Tyler Schmitt

November 2008

ACKNOWLEDGEMENTS

The author would like to give thanks to Dr. Cairns for his continuing support and insight and to Dr. McKittrick and Dr. Mandell for their knowledge and patience. He would also like to thank the Air Force Office of Scientific Research for their belief in this project.

In addition, this project would not have been possible without the technical expertise of John Parker, Jay Smith, and Dan Samborsky. Finally, this thesis would never have come into existence if not for the diligent efforts of Carol Anderson, Eileen Baker, Terry Kennedy, Joanne Wilke, Kayla Hunt, and Cheryl McNicholas.

TABLE OF CONTENTS

1. INTRODUCTION 1

Contemporary Composites in Aircraft Structures 3
Damage Tolerant Design 6
Design Hierarchy 7

2. STRENGTH AND STIFFNESS OF LAMINATES 10

Stiffness 10
Strength 13
Maximum Stress 14
Maximum Strain 15
Tsai-Hill Failure Criterion 15
Tsai-Wu Tensor 16
Hashin Failure Modes 18
Progressive Damage and Residual Strength 19

3. TESTING VIA MULTI-AXIAL LOADING 22

In-Plane Loader 24
Image Correlation 28
Asymmetrically Notched Coupon 30
Material Selection 30

4. OPTIMIZATION OF ELASTIC PROPERTIES 33

Materials 33
General Optimization 35
Nonlinear Optimization 39
Modeled Coupon 44
Optimized Results 49
CDB200 Triaxial Fiberglass 51
IM7 8552 Carbon Fiber Pre-Preg 52

5. DISSIPATED ENERGY DENSITY 55

Piecewise and Global Approximations 55
Deconvolution 57
Data Distribution 60
Constraints 65
Distribution of Nodes 66
Comparison of Solution Sets 68
Damage Initiation Isosurface 71

TABLE OF CONTENTS—CONTINUED

Inconsistencies and Modifications 73
Finite Difference Weighted Average 74
Symmetry in Shear Strain 76
Constrained Gradient 78
Unresolved Issues 81
Recreation of Load-Displacement Curves 81
Compromise between Detail and Representation 85
Improved Strain Determination 86
Misplaced Elemental Weight 88
Future Work 89
Non-orthogonal Elements 91
Statistical Variation 94

6. EMPERICAL CONSTITUTIVE RESPONSE 96

7. ASSUMED NONLINEAR RESPONSE 100

Simple Bilinear Response 100
Optimization Parameters 103
Secant Modulus 103
Modified Linear FEA Model 105
Displacement Step Size 106
Objective Function 109
Load-Displacement 109
Dissipated Energy 111
Full-Field Strains 112
Initial Conditions and State Variables 114
Optimized Results 115
Future Work 119
Platform, Geometry, and Ply Independence 120
Alternative Material Models 121
Modifications to the IPL 128

8. Conclusions 131

Application to Composite Structures 132

REFERENCES CITED 136

APPENDICES 140

APPENDIX A: IM7 8552 Test Data and Analysis 141
APPENDIX B: DED Function MATLAB Files 149

TABLE OF CONTENTS—CONTINUED

APPENDIX C: ANSYS Optimization BATCH Files.....154

LIST OF TABLES

Table Page

1. Optimized Coupon Stiffnesses 53
2. Comparison of Carbon Fiber Results 54
3. Comparison of Approximation Functions 56
4. Optimized Critical and Ultimate Strains 119
5. Stiffness Tensor Degradation Models 122

LIST OF FIGURES

Figure Page

1. Carbon Fiber Components of F/A-18 Hornet [4] 4
2. Typical Crack Growth Behavior [7] 6
3. Residual Strenth Capacity [7] 7
4. Design Hierarchy for Composite Structures [8] 8
5. Fourth Generation IPL 24
6. Actuator Vector Loop Kinematics 26
7. IPL LVDT Array 27
8. Typical IPL Test Coupons 31
9. Extended Interior Penalty Function [23] 41
10. Mesh for Gage Area of Notched IPL Coupon 45
11. Notched Coupon with Tabs 46
12. Coupon in Shear with and without Tabs 49
13. Convergence of Optimization Solvers 51
14. Relative Convergence of Elastic Properties 52
15. DED Function Data Points per Element 61
16. Actual DED Function Strain Distribution 63
17. IPL Load Directions for DED Function 64
18. DED Function Solution Process 68
19. Unconstrained DED Solution 69
20. DED Solution with Energy Constraints 70

LIST OF FIGURES—CONTINUED

Figure Page

21. Reproduction of DE from DED Solutions 71
22. Initial Damage Surface Based on Longitudinal Tension 72
23. DED Solution with Void Approximation 76
24. DED Function with Shear Symmetry 78
25. Converting Dissipated Energy Results to Load-Displacement 83
26. Comparison to Bearing Strength Tests 84
27. Possible Non-orthogonal Element Construction 93
28. Representative Bilinear Constitutive Response 101
29. Secant Modulus (Overshoot Exaggerated) 104
30. Convergence Due to Displacement Step Size 107
31. Erratic Rotation Data 110
32. Mismatched Elastic Constants 111
33. Strain Difference between Tests 113
34. Nonlinear Results for Shear Test 116
35. Nonlinear Results for Tension Test 116
36. Nonlinear Results for Shear and Tension Test 118
37. Multi-Stage Failure Modes [28] 123
38. Damage Variable Evolution [29] 125
39. Equivalent Bilinear Response [29] 127
40. IPL Backtracking 128

LIST OF FIGURES—CONTINUED

Figure Page

41. Residual-Strength-Considerate Component Life 134

ABSTRACT

Fiber reinforced plastics are increasingly being used in the construction of primary structures in the aerospace and energy industries. While their elastic behavior and fatigue response have been the subject of considerable research, less is known about the performance of continuous fiber composites following initial damage. Several competing models for the post-damage response of orthotropic composite materials are explored in this thesis. Each of these models includes only the in-plane loads experienced by the material and characterizes damage based on the local state of strain.

Starting with previous work performed at the Naval Research Laboratory and at MSU, the energy dissipated in multiaxially loaded coupons was used to optimize an empirical function that relates the three in-plane strains to the local dissipated energy density. This function was used to approximate a three dimensional damage initiation envelope as well as to quantify the severity of damage following first ply failure in a fiberglass laminate.

Carbon fiber reinforced epoxy was characterized using an assumed bilinear constitutive response. The elastic properties of the material were first optimized to minimize deviation from experimental data and then the necessary coefficients for a per-axis strain softening response were found using a similar optimization. This model provides detailed insight into the residual strength of significantly damaged material, as well as dissipated energy as a direct consequence.

To facilitate the need of these models for diverse local in-plane loading configurations, the MSU In-Plane Loader (IPL) was utilized. The tests performed in the IPL for this thesis were instrumental in validating a new image-correlation-based displacement monitoring system.

INTRODUCTION

The history of modern fiber reinforced composites likely began in 1932 with the work of a researcher at Owens-Illinois Glass Company by the name of Dale Kleist. In an attempt to develop a method for welding architectural glass, a hot jet of compressed air separated streams of molten glass from the welding surface that solidified into glass filaments. Although the weld failed, Kleist and his team eventually refined the technique into the steam-blown process. Before this innovation, all glass fibers produced were as staple, or small clusters held together by interwoven cross fibers. The steam-blown process allowed for the manufacture of continuous fibers. In 1938, Owens-Illinois, in a joint effort with Corning Glass, formed the Owens-Corning Fiberglass Corporation to market the advancements pioneered by Kleist. [1]

One of the first rolls of continuous fiber was purchased by Douglas Aircraft. Excessive lead time in the production of metal molds for hydropress sheet metal forming was slowing development, and cast plastic molds were inadequate for the for pressing process. It was thought that the plastic could be reinforced with the new fibers and, even if the molds could not be used for production runs, the molds would be able to produce enough parts to verify the rapidly changing designs. At first, phenolic resins were used to create the reinforced dies. Later, however, polyester resins developed by DuPont and curing processes stolen from the German war machine dramatically improved plastics

and, therefore, fiber reinforced plastics. The development of epoxy (patented in 1938) led to the direct predecessor of contemporary resins. [1]

At the onset of the Second World War, Owens-Corning began experimenting with weaving the fibers into fabrics and discovered the heat treatment that provides those fabrics with the flexibility required for use as reinforcement. Heretofore, fiberglass had been used primarily in dies and tooling; but, in 1942, the first fiberglass composite aircraft components were fashioned. The hectic pace at which aircraft were being designed and produced necessitated a prioritization of the aircrafts' internal systems. Generally, ducts existed as the last priority as they could be shaped around the other systems. This process inevitably resulted in some bizarrely shaped ducts such that metals could not be easy formed into those shapes. Fiberglass fabrics cured over plaster mandrels provided a quick solution that had the added benefit of weight savings. Some of the first structural aircraft components to be constructed from fiberglass were light engine nacelles and radar-transparent radomes.

As concerns grew about the immanent shortage of metal, engineers at Wright Patterson Air Force Base were charged with finding new and innovative uses for the fiberglass technology. Those engineers were also tasked with the monumental undertaking of optimizing both the manufacturing processes involved in constructing fiberglass composites as well as the design rules used in their application. Among the results of those developments were some of the most significant structural composite components of the time: fiberglass wings for the AT-6 and BT-15 training airframes. Several sets of wings were flown with

successful results, but structural composite aircraft components were not further pursued for several decades.

The dissolution of the military-industrial complex at the end of the war was especially unsettling to the fiberglass market. Large capital investments and governmental research funds were suddenly far more scarce, and composite manufacturers were often found investing in the tooling for composite consuming projects to improve the apparent viability and desirability of their products. These events, unfortunately, were transpiring at a time following great advancements in the materials themselves. Filament winding, vacuum bag molding, and pre-pregs would all play secondary roles to the economic downturn of the industry in general.

Contemporary Composites in Aircraft Structures

Arguably, composites are the most significant advancement in aircraft technology since the integration of aluminum [2]. However, the multiphase compositions complicate testing and design so production costs and lead times are often higher than metallic counterparts. Composites are then often slow to be adopted and implemented by the aircraft industry, if they are adopted at all. This resistance is evident in the gradual change in the amount of composite materials used in aircraft structures since their inception.

The first large scale production use of fiberglass was in the Boeing 707 in the 1950s, although only 2% of the structure made use of the new material [2]. With the advent of more advanced fibers such as carbon and boron, the U.S. Air

Force became interested in composites for control surfaces such as the horizontal stabilizer on the Navy's F-14 Tomcat interceptor. The penetration of composites into commercial and military designs continued and, in 1975 as part of the NASA Aircraft Energy Efficiency program, Boeing also developed a graphite/epoxy stabilizer for the 737-200 [3]. The British Aerospace-McDonnell Douglas AV-8B Harrier first flew in 1981 with an over 25% composite structure [2] with similar numbers for the F/A-18 Hornet [4].

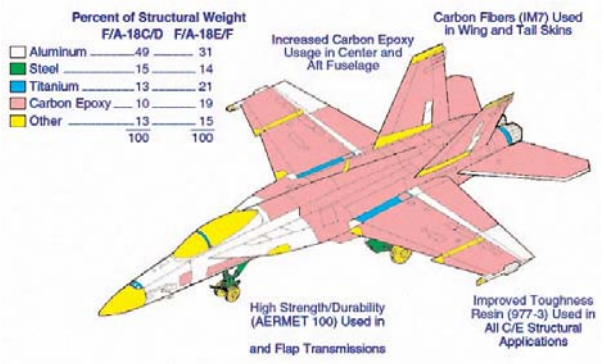

Figure 1. Carbon Fiber Components of F/A-18 Hornet [4]

Composites are used to lighten and strengthen existing aircraft designs, but they can also be used to implement features that are nearly impossible with traditional materials. One such an example of composites as an enabling technology is the forward-swept wing. Forward-swept wings have very desirable aerodynamic properties, especially at transonic speeds, and were successfully demonstrated by the Grumman X-29 in 1984 [2]. In addition, carbon fiber fan containment casings are at the forefront of safer powerplant designs for passenger aircraft.

Both military and commercial aircraft are progressively incorporating more composite components, although the assimilation in the former has been faster due largely to the difference in maintenance [2]. For instance, the Boeing 777 is about 10% composites by weight where the F-22 is more than a third. However, the Airbus A320 is over 28% composites which provide it with a nearly 20% weight savings and increased damage tolerance [4], while the Boeing 787 is expected to consist of almost 50% composites [5].

Since the beginning of the jet age, fatigue damage has been the vanguard of aircraft design. This trend developed as the result of the failure of early incarnations of the de Havilland Comet [6]. Composite materials are generally more resistant to fatigue than metals. In addition, the weight savings offered by composites can reduce structural loads and consequently further diminish fatigue damage. By extension, any advancement that can lead to reduced weight can mitigate the primary cause of failure in these structures. Additional understanding into the damage response of composite materials could reduce the amount of overdesign necessary for the predictable operation of an aircraft. That is, a structure that is designed to withstand infrequent overloads could instead be designed to withstand minor damage if the behavior of the material following damage is satisfactory for normal operation. Reducing the amount of material used by tolerating overloads would reduce the weight of the component and, therefore, cyclic loading related to the additional weight. Diminution of cyclic loading would abate the more dominant problem of fatigue damage. Studies into

several methods that share the purpose of providing understanding of such post-damage responses are developed in this thesis.

Damage Tolerant Design

A related methodology used by the United States Air Force [7] and its contractors to monitor aging fleet aircraft is the concept of damage tolerant design. This design philosophy is primarily used in the prediction and prevention of crack growth, but it provides a valuable guideline for the methods evaluated herein. Damage tolerant design relies on several practices. First, it is assumed that stable crack growth can be predicted with adequate knowledge of the loading of the component.

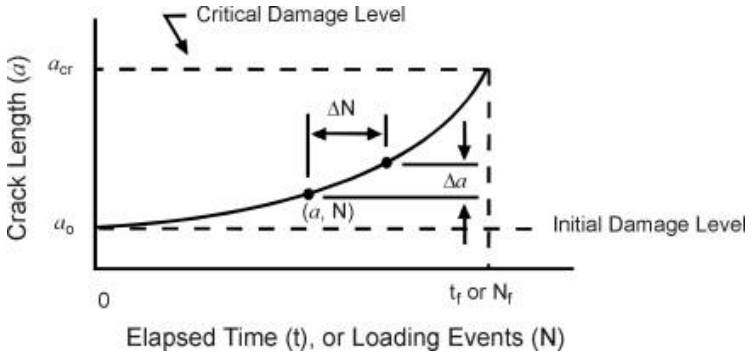

Figure 2. Typical Crack Growth Behavior [7]

The growth of a crack is contingent on the existence of a crack so an initial crack length must also be assumed based on the size of some preexisting flaw. Inspection intervals are formed based on the growth of the crack under normal conditions and the length of the crack when it becomes critical. Thus, some manner of inspection of the crack size must also exist. If a crack is detectable,

then the remaining usable life of the component is established based on its estimated residual strength.

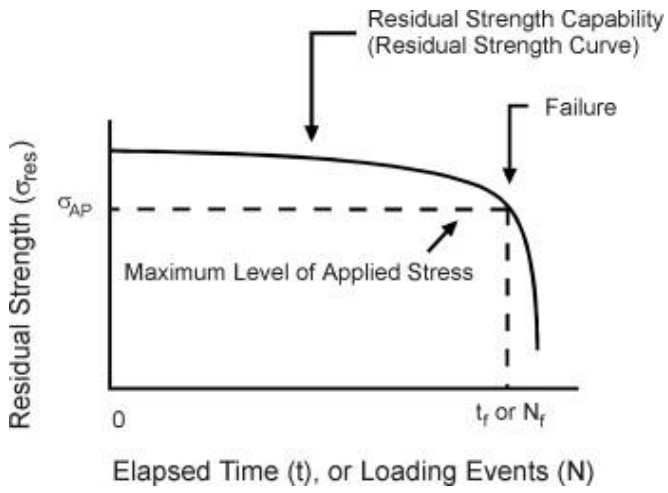

Figure 3. Residual Strenth Capacity [7]

Methods discussed in this thesis are used in the pursuit of an analogy to Figure 3 for non-cyclic and pseudo-static in-plane loading, except the design space covered needs to be multidimensional with respect to the many loading configurations available to non-isotropic materials. Thus, the damage state and residual strength of any element of material could be predicted.

Design Hierarchy

New composite materials are often slow to implementation due to the increased complexity associated with modeling the behavior of anisotropic materials. Unlike isotropic materials, there are many intermediate steps between coupon level testing and component level design [8]. Furthermore, coupon

testing itself can be far more complex since the materials behave in such a variety of ways.

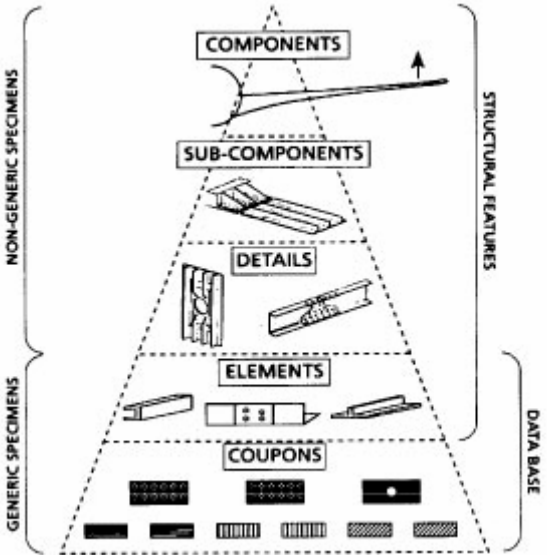

Figure 4. Design Hierarchy for Composite Structures [8]

All of the additional testing required to validate composite components can be prohibitively expensive, even when weighed against the sometimes immense structural benefits. This process tends to stifle the insertion of new composite materials into primary aircraft structures.

Methods that describe detailed post-damage response such as those presented in this thesis have the potential to significantly abbreviate this process. Most of these methods involve multiaxial coupon testing which can drastically reduce the number of tests when compared to traditional uniaxial testing. Of course, multiaxial testing requires special testing equipment but also eliminates the elaborate fixturing that is often needed to fully characterize orthotropic materials. Such tests and the ensuing analysis can provide insight into regions of

localized stress which may then translate into understanding of such regions in higher level specimens, thus reducing the need for intermediate and high level component testing.

10

STRENGTH AND STIFFNESS OF LAMINATES

The layered nature of composite laminates allows their analysis to be separated into two major components. One component assumes that the bonding between layers is perfect and indestructible and the other component views the interlaminar regions as irremovable flaws. The former, known as classical lamination theory, is an extension of plate theory with accommodations for the often non-isotropic properties of fiber reinforced composites [9]. The latter encompasses both fracture mechanics and fatigue.

Stiffness

Kinematic, constitutive, equilibrium, and force resultant equations all harmonize in the construction of classical lamination theory. The kinematics of laminate theory describe how displacements and strains are related and are subject to restrictions that are specific to thin media under small displacements. These restrictions are collectively referred to as the Kirchhoff assumptions and state that normals—lines that are perpendicular to the plane of the material—always remain undeformed and perpendicular. This conjecture leads to the conclusion that shear strain in the normal direction is negligible [9]. The details of classical lamination theory can be found in most composite reference texts [9, 10] and ultimately result in what is commonly referred to as the ABD matrix. This matrix relates the applied strains and curvatures, ε and κ, to the resulting

forces and moments, *N* and *M*. This relationship is used in finite element analysis of layered composites.

$$\begin{Bmatrix} \begin{Bmatrix} N_x \\ N_y \\ N_{xy} \end{Bmatrix} \\ \begin{Bmatrix} M_x \\ M_y \\ M_{xy} \end{Bmatrix} \end{Bmatrix} = \begin{bmatrix} \begin{bmatrix} A_{11} & A_{12} & A_{16} \\ & A_{22} & A_{26} \\ sym. & & A_{66} \end{bmatrix} & \begin{bmatrix} B_{11} & B_{12} & B_{16} \\ & B_{22} & B_{26} \\ sym. & & B_{66} \end{bmatrix} \\ \begin{bmatrix} B_{11} & B_{12} & B_{16} \\ & B_{22} & B_{26} \\ sym. & & B_{66} \end{bmatrix} & \begin{bmatrix} D_{11} & D_{12} & D_{16} \\ & D_{22} & D_{26} \\ sym. & & D_{66} \end{bmatrix} \end{bmatrix} \begin{Bmatrix} \begin{Bmatrix} \varepsilon_x^0 \\ \varepsilon_y^0 \\ \gamma_{xy}^0 \end{Bmatrix} \\ \begin{Bmatrix} \kappa_x \\ \kappa_y \\ \kappa_{xy} \end{Bmatrix} \end{Bmatrix} \tag{1}$$

The submatrix *A* relates the in-plane strains to the resultant forces and is often simply referred to as the stiffness matrix. The components of the submatrix *B*, when nonzero, result in a laminate that produces internal moments when a strain is applied to the neutral plane, or vise versa. Thus, it is labeled the bending-extension coupling matrix. Finally, the bending stiffness matrix *D* provides a direct relationship between the three components of curvature and the moment resultants. In addition, due to the unique nature of the shear strain γ_{xy} and the twist κ_{xy}, the components A_{16} and A_{26} as well as D_{16} and D_{26} are known as the shear-extension coupling factors and the bend-twist coupling factors, respectively. In this thesis, only in-plane loads are considered so the *B* and *D* matrices are either negligible or simply not important.

Often, it is desirable to eliminate some or all of the above coupling dynamics. For instance, any interaction between bending and extension can be eliminated by fabricating a laminate that is symmetric with respect to the neutral plane. As regards the diminution of the other couplings, it is often a matter of

tailoring the specific laminate for its intended loading. A laminate that has a distribution of plies that is symmetric with respect to the principal loading will have no shear-extension or bend-twist coupling in that direction. In any other direction where that symmetry condition is not met, however, the couplings may still exist. One special case, called a transversely isotropic material, is unburdened by coupling in any in-plane direction. This is achieved through radial symmetry of the distribution of the plies.

It is not always the case that a load-uncoupled laminate is the laminate best suited for an application. In fact, for certain purposes, bend-twist and other load coupling can be exploited to increase performance. For example, in an airfoil structure where the aerodynamic forces produce a distributed lift load, the center of loading is often not aligned with the axis of torsion. In this case, both bending and torsional loads are applied to the structure. Excessive twisting in these wing structures can lead to disastrous stall flutter, so the bend-twist coupling of a composite laminate can be used to negate the twisting due to off center loading. This concept is known as aeroelastic tailoring [10] and is used in the X-29 mentioned earlier. Furthermore, techniques that utilize the adaptable construction of laminates are not limited to purely mechanical loads. Variable thermal expansion properties can be used to guarantee uniform thermal expansion in conditions where the heating itself is not uniform.

Strength

A fiber derives its strength from its near crystal-sized diameter. The small diameter purges the material of nearly all lateral dislocations so the statistical likelihood of failure in the fiber direction is reduced asymptotically to nearly the atomic bond strength. Some fibers, like carbon fibers, also utilize the already anisotropic behavior of the bulk material to their benefit. In carbon fibers, well-bonded layers of graphite are aligned in the fiber direction leaving the weak interlaminar bonds in the transverse direction.

In general, the in-plane failure of a laminate is assumed to be the aggregation of the failure of the compositing layers. Since the layers themselves are heterogeneous, analysis for even a single layer is nontrivial. As with traditional engineering materials, the first step in describing the failure of a ply is determining when damage initiates—or when the material has left the realm of elasticity and energy is lost to material degradation. Several theories have been proposed for the damage threshold of orthotropic materials, although the most appropriate theory is often a matter of which provides the best fit for the material at hand. The problem with a material with as many inherent flaws and interfaces as a continuous fiber composite is that many different failure modes exist:

- Fiber rupture – Some fibers, like glass, are isotropic and some, like carbon, have more complicated constitutions. In either case, the stress at which a typical fiber will break is often considerably less than a theoretical or flaw-free fiber.

- Matrix cracking – The matrix material is usually isotropic and brittle, but loading complicated by residual stresses and stress concentrations makes microscopic prediction of its failure difficult.
- Debonding – While a fiber is theoretically much stronger than bulk material, it is entirely dependent on its interface with the matrix to provide any appreciable structure.
- Delamination – While not an in-plane phenomenon, separation of the individual layers of a laminate is a critical method of failure even under in-plane loading and can often obfuscate the determination of lamina properties.

Modeling of a composite at this microscopic level is generally very impractical; especially in the case of laminates, it becomes difficult to distinguish between the methods of failure. Damage criteria that are applied to generally anisotropic materials are often applied to composites for this reason.

Maximum Stress

At the most basic level, the strength of a material can be analyzed by assuming that each of the principal stresses is bounded by a maximum tensile stress X_T and minimum compressive stress X_C. If one of these bounds is exceeded, the material is said to have failed in that direction.

$$X_C < \sigma_1 < X_T \text{ and } Y_C < \sigma_2 < Y_T \text{ and } |\tau_{12}| < S \tag{2}$$

This criterion suffers from a complete lack of interaction between the principal directions and modes of failure. At the same time, the lack of interaction necessitates a distinction between the directions which can be useful since the different modes of failure are often more pervasive in—or even unique to—a particular direction.

Maximum Strain

Similar to the maximum stress theory, the maximum strain criteria consider each of the principal in-plane directions independently. The most substantial difference between the two methods, however, is that with the maximum strain theory, the effects of the material's Poisson's ratios are taken into consideration. Others factors may influence the strains besides direct loading such thermal expansion and moisture, but that is beyond the scope of this work.

Tsai-Hill Failure Criterion

Maximum stress and maximum strain analysis can sometimes produce adequate results, especially under uniaxial loading, but as soon as the loading becomes more complicated, neither method provides an effective match to experimental data. Hence, a failure criterion was proposed by Hill for orthotropic materials that is shown in equation (3) where each of the letters is a curve fitting parameter.

$$\begin{aligned}&(G+H)\sigma_1^2+(F+H)\sigma_2^2+(F+G)\sigma_3^2\\&-2H\sigma_1\sigma_2-2G\sigma_1\sigma_3-2F\sigma_2\sigma_3\\&+2L\tau_{23}^2+2M\tau_{13}^2+2N\tau_{12}^2<1\end{aligned}\qquad(3)$$

The equation is a modified version of the von Mises criterion for isotropic materials. The von Mises criterion, like most isotropic yield analysis techniques, is based solely on distortion energy and ignores dilatational energy; that is, changes in volume do not affect the predicted failure. In orthotropic materials, however, dilatation is an irremovable component of distortion [10].

Tsai's contribution to the method was to relate the parameters *F*, *G*, *H*, *L*, *M*, and *N* to the more familiar parameters *X*, *Y*, and *S*. First, it must be recognized that, within a single ply, the out-of-plane strength *Z* is equal to the strength in the transverse direction. Then, if uniaxial loading is considered along each of the three in-plane directions, the maximum stress and maximum strain equations agree and the Hill equation becomes the Tsai-Hill equation.

$$\frac{\sigma_1^2}{X^2} - \frac{\sigma_1\sigma_2}{X^2} + \frac{\sigma_2^2}{Y^2} + \frac{\tau_{12}^2}{S^2} < 1 \tag{4}$$

It should be noted immediately that the equation has lost the distinction between tensile and compressive failures in the fiber and transverse direction. In practice, this is only a minor inconvenience as the parameters *X* and *Y* can be assigned their tensile or compressive components based on the signs of the stresses. As always, failure in shear is independent of direction.

Tsai-Wu Tensor

In order to overcome the shortcomings of the previously mentioned methods, Tsai and Wu proposed a damage initiation surface with the following form.

$$F_i\sigma_i + F_{ij}\sigma_i\sigma_j = 1 \text{ for } i, j = 1,\ldots,6 \tag{5}$$

F_i and F_{ij} are tensors of the second and fourth rank, so the primary result of this method is the introduction of significantly more degrees of freedom (i.e., curve fitting parameters). This procedure could, of course, be continued ad nauseam to produce successively better fits, but the Tsai-Wu surface has the added advantage of being a tensor and thus can be rotated as such and so is independent of coordinate rotations. When reduced for the orthotropic materials of interest to this thesis and when considered for plane stress conditions, the equation simplifies considerably.

$$F_1\sigma_1 + F_2\sigma_2 + F_{11}\sigma_1^2 + F_{22}\sigma_2^2 + F_{66}\tau_{12}^2 + 2F_{12}\sigma_1\sigma_2 = 1 \tag{6}$$

The inclusion of terms that are second order in stress allows for simultaneous consideration of tensile and compressive failure. For example, suppose an orthotropic material is loaded solely in the 1-direction. In that case, the above equation is condensed to two terms, but it is possible for the failure to occur either in tension or compression.

$$F_1X_T + F_{11}X_T^2 = 1 \text{ or } F_1X_C + F_{11}X_C^2 = 1 \tag{7}$$

Solving the above equations results in values for F_1 and F_{11} based on the independent tensile and compressive strengths. Similar values exist for the 2-direction.

$$F_1 = \frac{1}{X_T} + \frac{1}{X_C} \text{ and } F_{11} = -\frac{1}{X_T X_C} \tag{8}$$

Although the Tsai-Wu tensor provides great improvements over the other methods mentioned, it still suffers from a few deficiencies. Most notably, determination of the remaining tensor quantities can be difficult and, therefore, expensive. The F_{12} term in particular is the coefficient on the product of σ_1 and σ_2 and can only be determined with biaxial testing. According to Jones, however, variations in F_{12} have little effect on modeled outcomes. Like the Tsai-Hill criterion, the Tsai-Wu criterion does not distinguish between modes of failure.

Hashin Failure Modes

Among the first to suggest a failure criteria that discriminates between any of the many modes of failure accessible to composites while including coupling effects was Zvi Hashin [11]. Primarily, the approach takes notice of the high degree of anisotropy in unidirectional fiber composites and separates the transverse direction—which supports smaller loads but in which damage is no less significant—from the longitudinal direction. Longitudinal and transverse failures are then denoted as fiber and matrix failures, respectively. The method also clearly differentiates between compressive and tensile failure modes.

The principal conclusion to Hashin's work was that matrix failure F_m is the result of a direct coupling between transverse stress and shear stress. Results regarding fiber F_f failure were far less conclusive. Several conditions have been

proposed, the most agreed upon of which range between maximum stress failure and a coupling similar to the matrix criterion.

$$F_m^t = \left(\frac{\sigma_{22}}{Y_T}\right)^2 + \left(\frac{\tau_{12}}{S}\right)^2$$
$$F_f^t = \left(\frac{\sigma_{22}}{X_T}\right)^2 + \alpha\left(\frac{\tau_{12}}{S}\right)^2 \quad (9)$$

Typically, the parameter α in equation (9) is set to either zero, for maximum stress failure, or one, for shear-coupled failure, but in theory could be assigned a value anywhere in between to illustrate the degree of interaction between directions. As with the other damage initiation criteria, failure in the fibers or matrix is said to have occurred when the corresponding output variable meets or exceeds a value of one. Output variables for compressive modes have also been proposed [11] but have not been included here for brevity.

Progressive Damage and Residual Strength

Each of the preceding damage criteria is applicable only up until the proportional limit of the material. None of these methods provide any information about the material following initial damage. As mentioned in the introduction, engineering is tending towards designing components to be leaner (especially as concerns the aerospace industry) such that they may encounter overloads intermittently within their lifetimes. If this is to be the case, then knowledge of the component's behavior following such events will be paramount.

With the science of damage prediction within unidirectional composites only now reaching maturity, the science of the evolution of that damage is only now poised for cultivation.

The damage is not in itself particularly useful towards structural ends but, correctly applied, can yield the residual strength of the material. Residual strength is used here to encompass both the ultimate loads that the material is still able to support and the many stiffness constants—now variables—that approximate how the material deforms under loading after damage. Again, the binary nature of composites requires that this analysis be simplified by decomposing it into laminar and interlaminar effects. While certainly not a trivial problem, interlaminar effects like delamination find attention in other fields involving crack growth and fatigue. The progressive damage and residual strength within individual layers will then be explored in this thesis, although the two regimes of failure may not be as distinct as implied.

Compensation for the inseparability of 2-dimensional laminar and 3-dimensional interlaminar effects can be made using several techniques. For instance, in most laminates, a transverse crack would serve as an initiator for delamination which—since continuity between layers would be broken by the transverse crack—could dramatically affect the strain field. Although not a long-term solution, materials were chosen for this work that are known to be less susceptible to such delamination. A more complete solution would be to fully model the crack-seeded delamination as has been done in previous work [12], but the complexities may not be warranted compared to the in-plane concept

developed in this thesis. Within this limitation (that is, a continuum response rather than a 3-dimensional fracture architecture), compensation is attempted by saturating the model with experimental data that encompasses several modes of failure that are not distinguished, thereby smearing each mode into one. By uniting an in-plane material model with such a data-rich environment, the model can be inclusive of out-of-plane phenomena without being overwhelmed by them. This will have particular applications to finite element modeling, wherein the in-plane data from this thesis will be applicable to a practical structural model which does not require three-dimensional modeling throughout the domain.

TESTING VIA MULTI-AXIAL LOADING

Composite materials differ from traditional materials in several important ways. Even a single lamina, especially one with continuous, aligned fibers, can have vastly different properties in different directions. Additionally, these materials generally cannot be classified as either ductile or brittle; the different behaviors apparent in the fibers and the matrix material, as well as the interaction at the interface between the two, complicate the response greatly. Testing for and application of isotropic material properties is a relatively well developed science, especially when compared to the generally orthotropic constants that must be found to characterize a continuous fiber composite.

For an isotropic material, only two constants need to be found to model the material reaction under loading in any direction. These two constants are the elastic modulus and the lateral contraction coefficient. The elastic modulus, or Young's modulus, is the ratio of applied stress to resultant strain and can be found by a simple uniaxial test. The lateral contraction or Poisson's ratio for an isotropic material is the negative of the ratio of lateral strain to the strain in the loaded direction. Due to the requirement that the shear modulus must be positive, Poisson's ratio cannot be greater than 0.5 or less than -1. Most materials, however, have a Poisson's ratio greater than zero, meaning they contract in the lateral direction when stretched.

Since they behave identically in all directions, isotropic materials are said to have an infinite number of axes of symmetry. An orthotropic material has only

two or three axes of symmetry so its mechanical properties will be different along each of those axes. In the worst case, nine components of the compliance tensor need to be identified to describe an orthotropic material; but, since continuous fiber composites are largely of interest due to their in-plane characteristics, it is often sufficient to test for those four coefficients alone.

$$\begin{Bmatrix} \varepsilon_1 \\ \varepsilon_2 \\ \varepsilon_3 \\ \gamma_{23} \\ \gamma_{31} \\ \gamma_{12} \end{Bmatrix} = \begin{bmatrix} S_{11} & S_{12} & S_{13} & 0 & 0 & 0 \\ & S_{22} & S_{23} & 0 & 0 & 0 \\ & & S_{33} & 0 & 0 & 0 \\ & & & S_{44} & 0 & 0 \\ & \textit{sym.} & & & S_{55} & 0 \\ & & & & & S_{66} \end{bmatrix} \begin{Bmatrix} \sigma_1 \\ \sigma_2 \\ \sigma_3 \\ \tau_{23} \\ \tau_{31} \\ \tau_{12} \end{Bmatrix} \tag{10}$$

Still, determining those four coefficients is not a trivial task. A first effort often involves traditional uniaxial testing of a unidirectional layup along its various axes. The problem with this approach is that, without the support of oblique fibers, a unidirectional layup is especially vulnerable to matrix cracking between fibers. This matter is additionally complicated by the end loading due to the gripping techniques of traditional testing. Consequently, creative and often expensive fixturing is required in order to test composites in this manner.

Uniaxial testing can also be misleading when it comes to describing the strength of composites. Much of that strength is derived from a composite's ability to distribute damage. In a unidirectional layup, for example, cracks in the matrix can easily propagate through the thickness whereas a crack would be readily terminated by subsequent layers in a layup with fibers in multiple

directions. Therefore, although the interaction between layers depends heavily on the specific layup, it would provide a much more accurate portrayal of the actual material if those distributive advantages were to be included in the testing.

In-Plane Loader

To accomplish this robust testing, researchers at MSU have been inspired by previous work at the Naval Research Laboratory [13] to develop a testing machine that is capable of loading coupons in all of the three in-plane directions: tension/compression, shear, and rotation. The in-plane loader as it exists today can be seen in Figure 5.

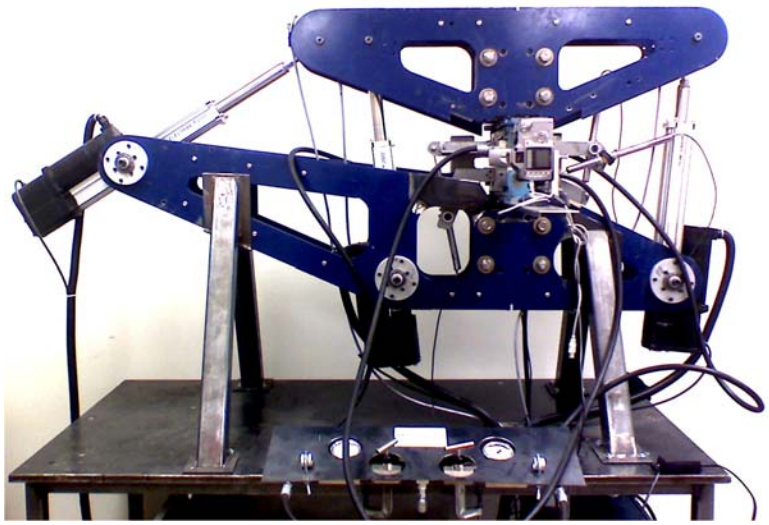

Figure 5. Fourth Generation IPL

While currently in its fourth generation of modification, the majority of the components of the system above were present in the original incarnation of the IPL. In an ideal situation, the only components necessary for a functionally operating IPL would be the actuators, load cells, grips, and two frame pieces.

Indeed, its earliest configuration consisted of scarcely more than that but experience has shown that additional control and measurement elements are required if meaningful data are to be produced [14].

The first generation IPL relied solely on the motion of the actuators for displacement control. In this instance, the entire apparatus was arranged horizontally with the large frame piece fixed and the small piece allowed to roll on a number of ball casters. The machine was placed horizontally in the hope that the weight of the heavy frame pieces would be sufficient to keep all loads in the plane of the coupon. These two sections of the frame are attached together by means of the three displacement actuators each with tapered roller bearings at its ends. Stepper motors drive the ball screw actuators and at the end of each actuator is a pancake load cell. Loads measured by the load cell are, therefore, always aligned with the direction of motion of their respective actuators. To manipulate the three in-plane degrees of freedom of the smaller frame piece, the three actuators are positioned such that at least two are nonparallel. Two of the three are roughly aligned with the coupon length in anticipation of higher loads in this direction since each actuator is rated to only about 8900N. This arrangement is also the most intuitive for producing rotations.

Displacements at the grips are determined tentatively using kinematic vector loop equations. Equation (11) is a representative example of the idea that the summation of the displacements in any closed loop is identically zero [14]. With three independent loops, the three degrees of freedom of the smaller frame piece can be determined and, with them, the position and rotation of the grips.

The grips themselves were originally just thick metal plates with knurled surfaces—two of which were rigidly attached to the frame pieces—pressed together using eight heavy bolts.

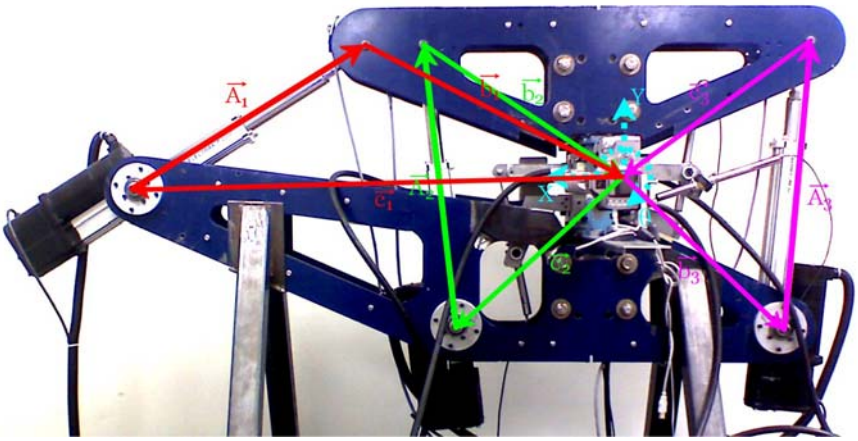

Figure 6. Actuator Vector Loop Kinematics

$$\vec{A}_i + \vec{b}_i + \vec{c}_i = \vec{0} \tag{11}$$

Second generation modifications were made largely to correct for unforeseen however obtuse errors in the acquisition of displacement data. Although the plates of the frame are constructed from 6.35mm thick steel, necessarily high loads and stress concentrators from holes cut through the plates allow for considerable elastic deflection in both frame pieces. Also, since each grip had one plate rigidly attached to the frame, alignment of coupons with the actuator axes could not be guaranteed when the coupons were of varying thickness. The solution to the latter problem was the implementation of a pair of self-centering grips each formed from a modified Palmgren vice and a pair of hydraulic jacks. Each side of the grip now needs to be fixed to its base after the

hydraulic pressure has been applied so, in order to facilitate access to both sides of the IPL, the device was moved to a vertical position. Weight from the mobile grip then no longer contributes to the constraint of its motion within the plane so two plates sandwiching a plate of ball bearings were added to serve this purpose. More accurate measurement of the motion of the new grips was accomplished through the use of three linear variable displacement transformers. These are attached directly to the grips and relative motion between them is determined using kinematic vector loops similar to those used with the actuators. Incongruity between displacements predicted by the actuators and those measured by the LVDT array are resolved with a computational feedback loop.

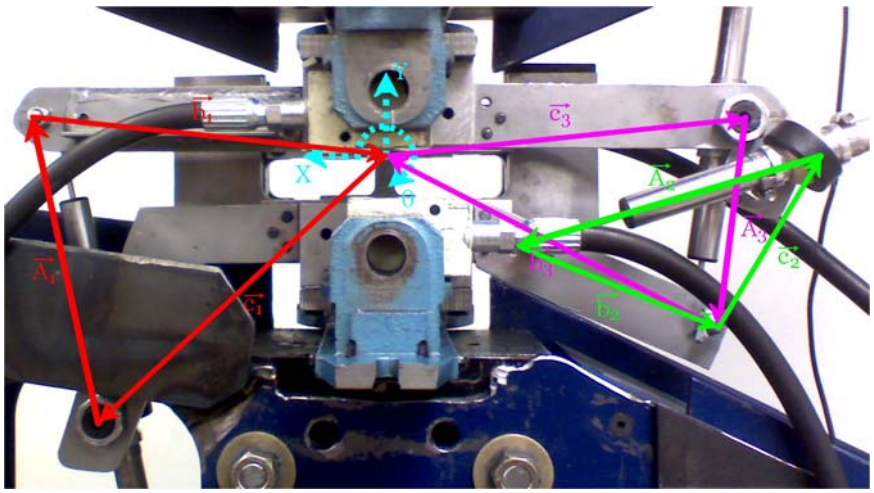

Figure 7. IPL LVDT Array

Improvements to the measurement of the movement of the grip edges are futile if the coupon slips in the grips. Both the first and second generation designs of the IPL made use of knurled grip surfaces, but coupons exiting those grips exhibited the signs of considerable slippage of the coupon within the grips [15].

For the third stage in the evolution of the IPL, a surface treatment designed specifically for gripping fiber reinforced polymers. This coating is known as Carbinite™ and is actually a carbide alloy that is bonded to the metal through electrofusion. To compliment the new grip surfaces, a new hydraulic pump was also installed that provides over three times the available gripping pressure.

Image Correlation

In its most recent iteration, control of critical variables within the IPL has lost priority to their accurate observation. The fourth generation IPL did not involve the replacement or alteration of any internal components, only the addition of a digital camera to monitor the distortion of the coupon. Rather than measure the grip edges that may be in imperfect contact with the coupon, edge displacements can now be found directly from the coupon. This is performed using digital image correlation. The camera is mounted rigidly near the grips of the immobile frame section and is focused on the coupon such that it captures the same area with each photograph.

A reference image is first taken of an undisplaced coupon after which subsequent images are acquired as the IPL translates through the desired steps. Subsections of the reference image surrounding specified control points are virtually displaced over the actual displaced images until the correlation between the two is at a maximum. This correlation is based on the intensity of the pixels of the images, so black and white images are used. Since the displacements of these coupons are expected to be very small, a very fine speckle pattern is sprayed over

the gage section of each coupon before it is loaded into the IPL. Correlation at a given pixel displacement *(u,v)* between the subsection *f* of pixel dimensions *(i,j)* and the displaced image *t* is given in equation (12). The correlation must be normalized by the mean and variance of the intensity of each sub-image to compensate for variable intensity across the images and because, otherwise, the correlation would depend on the chosen subsection size.

$$\gamma(u,v) = \frac{\sum_{i,j}\left(f(i,j) - \bar{f}\right)\left(t(i-u, j-v) - \bar{t}\right)}{\sqrt{\sum_{i,j}\left(f(i,j) - \bar{f}\right)^2 \sum_{i,j}\left(t(i-u, j-v) - \bar{t}\right)^2}} \quad [16] \tag{12}$$

Over a specified range, the actual displaced position of the control point corresponds to the displacement at which the correlation coefficient finds its maximum. As posed, however, this method is only capable of resolving displacements to the accuracy of a single pixel. This situation can be improved well beyond that limit by means of curve fitting and gradient-based techniques which are employed in the analysis of IPL coupon images but are not within the scope of this thesis. Several control points along the edge of the coupon give the best available estimate of the actual boundary movement of the coupon as explained in the next chapter. In addition, displacements of interior control points can be found and their numerical derivatives taken to find strains.

Asymmetrically Notched Coupon

In order to fully exploit the biaxial capabilities of the IPL and to circumvent grip induced failures that plague composite material testing, a notched coupon has been used with success by both Ritter [8] and Smith [15]. In essence, the notch is used to concentrate loads so that damage initiation and progression are localized in a region where they can be monitored and can be safely assumed to be the result of in-plane loads exclusively. It is deliberately designed to be asymmetric with the goal of increasing the diversity of local loading conditions observed over the coupon.

Material Selection

Two materials were used to construct these coupons during the course of this research. The first material was a multilayer fiberglass fabric that has been the subject of much study at MSU. This fabric, Owens Corning Triaxial CDB200 [17], was prepared using a modified hand layup with Hexion EPON 826 resin and EPI-CURE 3234 for a curing agent [18,19]. The fabric consists of a primary ply with two plies offset by 45° in both directions. To reduce the possibility of buckling under unanticipated compressive loads, the primary plies of two layers of fabric were placed on the outside of the coupon to increase bending stiffness. Unfortunately, such a layup using a multilayer fabric cannot be performed while maintaining symmetry about the neutral plane, so the resulting layup was [0/±45/±45/0]. For the remainder of this analysis, it is assumed that any twist

couplings are negligible when compared to the in-plane loads on this material. One of the fiberglass IPL coupons is shown on the left side of Figure 8.

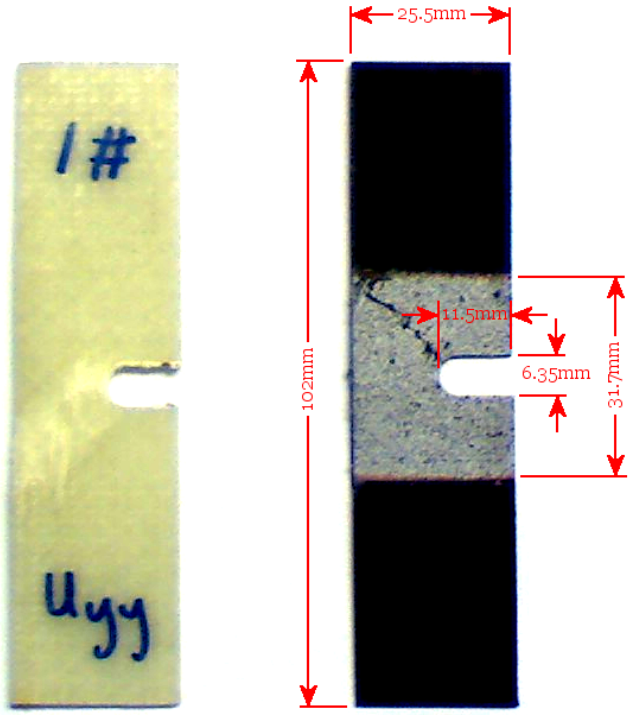

Figure 8. Typical IPL Test Coupons

HexPly 8552, half of the second material used, is an amine cured, toughened epoxy that, in this case, came supplied with Hexcel IM7 unidirectional carbon fibers in the form of a fabric pre-impregnated with the resin system [20]. The highest quality layups made from this material were cured under vacuum bags at 180°C for two hours after having been warmed and adhered by a heat gun. Originally, an eight layer quasi-isotropic laminate was to be used but its thickness proved to be too strong for the IPL and the overlapping longitudinal and transverse layers were not conducive to much of the desired analysis. Ultimately, a $[\pm 30]_s$ laminate was chosen because it required only half the

thickness and a plate of such a laminate could be also rotated and cut into coupons with a $[\pm 60]_s$ layup. The latter were later found to be unusable for this analysis because the amount of overlap of the plies near the notch was not sufficient for a prolonged damage event and resulted in complete and nearly instantaneous delamination. The high-contrast speckle pattern used in the image-based displacement tracking can be seen on the gage area of a carbon fiber IPL coupon in Figure 8.

OPTIMIZATION OF ELASTIC PROPERTIES

One method for estimating the linear elastic response of aligned fiber composites is through micromechanics. Micromechanics attempts to characterize a heterogeneous material by summation of its individual phases. In the direction of the axis of the fibers, for example, the stiffness of the composite is analogous to the combined stiffness of the fiber and matrix materials if they are viewed as springs in parallel. Similarly, the stiffness in the direction transverse to the axis of the fibers is equivalent to the same springs in series.

Micromechanical analysis can become convoluted, however, when the constitutive materials are themselves not isotropic. The method is also entirely neglectful of any fiber-matrix interface interaction; but, because of its simple implementation, micromechanics are often employed to provide heuristic estimates of orthotropic composite properties. The estimates provided are rarely used without considerable empirical verification, and that verification is the subject of this thesis.

Materials

In choosing a material on which to perform testing and eventual analysis, several factors were considered. First, it is desired that the materials be among those that are commonly used in composite structures. The reason for this is twofold: a fabric already employed in the field will have already had considerable study into its properties and the industry can only benefit from any additional

insight into materials that are already in service. A material for which many properties are already known is advantageous towards this research in at least two ways. In the case of the linear-elastic optimization, the published values provide a requisite benchmark to compare the results obtained through the proposed method and those obtained through traditional testing methods. Furthermore, a material with well-known elastic properties will later allow for greater emphasis to be placed on determination of the nonlinear properties. In practice, a similar situation would likely be encountered. The linear properties would, of course, be determined for initial analysis either by traditional means or by this new method. Then, should it be determined that a particular component could benefit from post-damage analysis—generally because that component is poorly suited for frequent or convenient maintenance—the nonlinear properties can be found with the aid of the previously revealed elastic properties.

Anisotropy was also considered during the material selection process. Stiffness and strength are vastly higher in the fiber direction in this type of composite. By necessity, testing for this research involves multidirectional laminates so the overall properties of the coupon are dominated by the fiber properties in every direction. This dominance greatly hinders the discovery of the off-axis lamina properties through optimization. The hindrance is proportional to the anisotropy ratio of the material because changes in those properties produce proportionally smaller changes in the resultant coupon stiffnesses that are used in the minimization variable. Hence, the model and therefore the optimization

are considerably less sensitive to those properties. As explained by Huang, the key to surmounting this problem is thoughtful bounding [21].

Originally, the CDB200 Triaxial fiberglass tests were used for this process because fiberglass composites typically have much lower anisotropy ratios [22]. In addition, glass laminates also store considerably more strain energy than those based on carbon due to their high strain to failure. It was thought that the energy methods described in later chapters would be easier to prove with such a material. After the process had matured, however, and the reliability of the dated Triaxal tests came under question, the IM7 carbon fiber pre-preg test data were used despite the material's higher anisotropy ratio. Additional complications can be avoided by preparing the laminate such that none of the transverse axes are aligned with any of the fiber axes. Such an alignment causes effects from the two directions to become indistinguishable.

General Optimization

Numerical optimization can be categorized as linear or nonlinear. For linear optimization, the variables sought must be fully described by a set of linear equations. An equation, in turn, is said to be linear if each term is either a constant or simply proportional to one of the variables. Generally speaking, a set of variables found using linear optimization will have an over-determined data set. That is to say that there are more linear equations describing the variables than there are variables and that there is an independent linear equation for each variable. Such a set is usually solved through least squares regression.

Least squares regression is so named because it seeks to minimize the squares of the residuals: the differences between the actual values and the predicted values. The squares of the residuals are used because that method corresponds to the solution of maximum likelihood if experimental error is assumed to have a normal distribution. Also, for a quadratic equation, only one critical point exists so a solution is guaranteed.

To further discuss the solution to the least squares problem, some mention must be made of optimization in general. For any optimization, there are at least two types of variables. The two types most fundamental are the design variables β_j and the objective function f. Design variables are the parameters that are optimized in order to minimize the objective function. In the case of linear least squares regression, the objective function is the sum of the squares of the residuals r_i.

$$f\left(\vec{\beta}\right) = \sum_{i=1}^{m} r_i^2 \tag{13}$$

$$r_i = y_i - \sum_{j=1}^{n} X_{ij}\beta_j \tag{14}$$

Finding the minimum of the objective function with respect to the design variable vector is as simple as setting the gradient of the objective function to zero.

$$\vec{\nabla} f\left(\vec{\beta}\right) = \vec{0} \text{ is equivalent to } \frac{\partial f}{\partial \beta_j} = 0 \text{ for } j = 1, \ldots, n$$

$$\frac{\partial f}{\partial \beta_j} = \frac{\partial}{\partial \beta_j}\left(\sum_{i=1}^{m}\left(y_i - \sum_{k=1}^{n} X_{ik}\beta_k\right)^2\right) = -2\sum_{i=1}^{m}\left(y_i - \sum_{k=1}^{n} X_{ik}\beta_k\right)X_{ij} = 0 \qquad (15)$$

$$\sum_{i=1}^{m}\sum_{k=1}^{n} X_{ij}X_{ik}\beta_k = \sum_{i=1}^{m} X_{ij}y_i \text{ becomes } X^T X\vec{\beta} = X^T\vec{y} \text{ in tensor form}$$

Linear regression is used extensively and will be discussed further in the chapter on the dissipated energy density function. For the most part, however, nonlinear optimization processes are used in this thesis even where a linear algorithm might be sufficient. This is done largely in an effort to simplify the debugging procedure for the more complicated analysis that does require nonlinear optimization. In addition, nonlinear analysis can sometimes be considerably more transparent.

As an example, it may be possible to approximate most linear properties through linear least squares alone. Due to the linear nature of finite element analysis, an increase in the modulus of the modeled material results in a proportional increase in the loads and, therefore, stiffnesses of the model under constant displacement. By considering the individual contributors as layers of unknown thickness β_j in a 2-D model, the loads from models with differing elastic constants can be combined linearly. The Poisson's ratio cannot follow this progression for reasons seen later, in equation (46), and discussed in more detail in Chapter 5.

$$\sum \beta_j \begin{Bmatrix} E_1 \\ E_2 \\ G_{12} \end{Bmatrix}_j \rightarrow \sum \beta_j \begin{Bmatrix} F_x \\ F_y \\ T_{xy} \end{Bmatrix}_j \tag{16}$$

Consequently, a quasi-arbitrary arrangement of three finite element models with differing elastic constants can be used to approximate the actual elastic constants knowing only the loads and displacements from several multiaxial tests. The arrangement can only be quasi-arbitrary because the trivial solution must be avoided by having linearly independent vectors and the distortion of the modeled coupons must be consistent enough as to maintain the distributive principle of the stiffness tensors. Each model must be run in three independent directions so that the displacements can be scaled to match each test. Again, the justification for this is given later, in equation (34), and its preceding text.

$$r_i = \begin{Bmatrix} F_x \\ F_y \\ T_{xy} \end{Bmatrix}_i - \sum_j \beta_j \sum_k \frac{u_{k,i}}{u_{k,j}} \begin{Bmatrix} F_x \\ F_y \\ T_{xy} \end{Bmatrix}_{k,j} \tag{17}$$

Once solved for by equation (15), the unknowns can be reinserted into equation (16) to reconstitute the optimized elastic constants. However, the derivation of this method is convoluted and the assumption of consistent distortion across models with different properties is debatable. For these reasons and for the exclusion of the Poisson's ratio, this process can be discarded for a more limpid parametric nonlinear optimization.

The final type of variable available to an optimization solver is a state variable. State variables constrain the system but are generally dependent on design variables. A state variable that might be included in the optimization of elastic properties is one that describes whether the resulting stiffness tensor is positive-definite. This condition is unlikely to be violated with small variations but is critical to FEA stability. State variables play a much more important role in the optimization of nonlinear properties.

Nonlinear Optimization

All nonlinear optimization was performed using the ANSYS finite element modeling program. This program contains a very robust set of optimization tools, but the two primary methods are the Subproblem Approximation Method and the First Order Method [23]. The toolset also contains a large collection of other routines intended to provide better understanding of the design space.

As described by the ANSYS Theory Reference, the Subproblem Approximation Method (SAM) is “an advanced zero-order method which uses approximations (curve fitting) to all dependent variables” [23]. As a zero-order method, it requires no information about the derivatives of the objective or state variable functions. Consequently, a zero order method is considered to be less computationally intensive as derivatives must be calculated numerically. In this method, each dependent variable (the objective function and all of the state variables) is fit with a quadratic function with respect to the design variables.

$$\hat{f}(\vec{\beta}) = f(\vec{\beta}) + error = a_0 + \sum_i a_i \beta_i + \sum_i \sum_j b_{ij} \beta_i \beta_j \quad (18)$$

The curve fitting on a and b employs the linear least squares regression discussed earlier. As an objective function for that regression, ANSYS uses a weighted residual. The weighting factors can be controlled by the user, but those most commonly used are uniform weights or where the design sets nearest the best design—those with the lowest objective function—receive the highest weights.

Again, the solution set must be overdetermined, so a sufficient number of design sets must be available. Design sets can either be provided by the user or, in the case that the number of provided sets is less two more than absolutely required, design sets are generated randomly within the design space. Once the data set is sufficient, the curve fit is obtained and minimization on the approximation function is performed. However, the approximation function is subject to constraints on the design variables as well as constraints created by the optional state variables. To solve such a system, the constrained problem must be converted to an unconstrained one. The unconstrained problem is achieved through the implementation of penalty functions [23]. A penalty function is a weighting function that tremendously increases the objective function as a variable approaches and surpasses its bounds, making that design set less and less likely. Penalty functions in ANSYS are all of the extended-interior type. For example, near the upper bound of the variable w, its penalty function would have the following form.

$$W(w_i) = \begin{cases} c_1 + \dfrac{c_2}{\overline{w} - w_i} & if \quad w_i < \overline{w} - \varepsilon(\overline{w} - \underline{w}) \\ c_3 + \dfrac{c_4}{w_i - \underline{w}} & if \quad w_i \geq \overline{w} - \varepsilon(\overline{w} - \underline{w}) \end{cases} \tag{19}$$

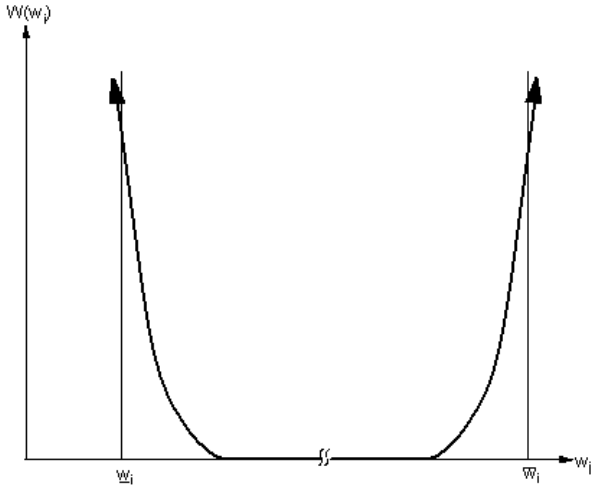

Figure 9. Extended Interior Penalty Function [23]

In the above function, ε is not intended to represent strain but instead to signify its mathematical connotation as an arbitrarily small positive number. Also, the c coefficients are internally determined by ANSYS.

Having established penalty functions, the new unconstrained problem is summarized by equation (20). Constraints on the design variables are enforced by the penalty function B, whereas G, H, and W are constraints of various forms on state variables.

$$F(\vec{\beta}, p_k) = \hat{f}(\vec{\beta}) + f_0 p_k \left(\sum_i B(\beta_i) + \sum_j G(\hat{g}_j) + \sum_m H(\hat{h}_m) + \sum_n W(\hat{w}_n) \right) \tag{20}$$

The reference objective function value f_o is intended to reflect the units and magnitude of the true objective function, although the units go largely unnoticed in numerical analysis. Known as the response surface parameter, the iterative variable p_k is a result of the sequential unconstrained minimization technique used to solve each design iteration. With each successive iteration, p_k is increased to amplify the weight of the penalty functions and improve convergence and accuracy. Convergence is assumed to have occurred when the magnitude of the difference between the current value for the objective function and the previous or best value is within a predefined limit.

The First Order Method (FOM) uses a modified objective function similar to that derived via penalty functions for the Subproblem Approximation Method. The difference between the two methods is that the FOM uses functional derivative information to establish search directions rather than using global approximation functions. For the initial iteration, the search direction is in the steepest descent direction from the initial guess. Following the initial step, conjugant directions are established based on the Polak-Ribiere recursion formula [23], the details of which are beyond the scope of this thesis. The search directions are applied to the solution vector as in equation (21).

$$\vec{\beta}^{\,j+1} = \vec{\beta}^{\,j} + s_j \vec{d}^{\,j} \tag{21}$$

Motion of the solution vector depends on the line solution parameter s_j whose value is determined through a golden-section algorithm combined with local quadratic curve fitting. Its distance is also limited by a global maximum limiting

the speed of convergence but also reducing the possibility of overshoot. “The algorithm is also occasionally restarted…forcing a steepest descent iteration. Restarting is employed whenever ill-conditioning is detected, convergence is nearly achieved, or constraint satisfaction of critical state variables is too conservative” [23].

As mentioned, the gradient vector is calculated using a finite difference numerical approximation. A first order forward difference is used by ANSYS for this purpose. The forward difference is used for two main reasons: the functional value at the point the gradient is to be calculate is already known as it is needed for other calculations and the added accuracy of a higher order or central difference is offset by calculation time. Additional convergence steps are, in this case, less costly than more accurate derivatives.

$$\frac{\partial Q(\vec{\beta})}{\partial \beta_i} = \frac{Q\left(\vec{\beta} + \hat{e}_i \Delta\beta_i\right) - Q\left(\vec{\beta}\right)}{\Delta\beta_i} + O\left(\Delta\beta_i\right) \tag{22}$$

The size of the finite difference step is defined in ANSYS as a percent of the range of values available to the design variable. This value can be critically important with objective functions that contain considerable amounts of noise.

Convergence of the FOM is assumed under the same conditions as the SAM. It is additionally required that the last iteration is performed using the steepest descent method. Because so many additional functional evaluations are required for the gradient calculations in the FOM, it is considerably less efficient. However, it is generally accepted that the addition of first-order information

contributes to a more accurate result. On the other hand, all steepest descent methods are susceptible to local rather than global convergence. Of course, this would only be an issue with functions having pronounced variations of higher than second-order, which are not anticipated in this analysis.

Modeled Coupon

Sufficient refinement of the mesh around the notch is critical to modeling the notched coupon. The notch is intentionally included as a stress concentrator to divert damage away from the gripped areas and to create a non-uniform strain profile whose diversity is amplified by a variety of loading conditions. To accurately characterize the local strain field in this area through finite element modeling, the resolution of the mesh must be increased. This is not true of the remainder of the coupon as the deformation becomes more regular at distances farther from the notch. Thus, the model developed uses a fine mesh distribution on the notch that expands radial outward into the rest of the coupon as seen below. The section of the coupon shown in Figure 10 corresponds to the gage sections of the test coupons in Figure 8.

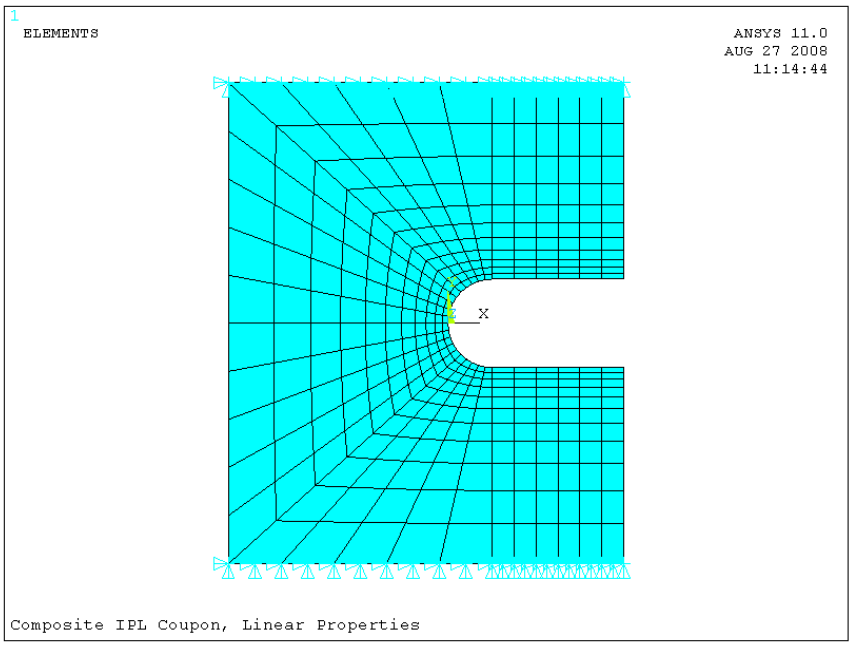

Figure 10. Mesh for Gage Area of Notched IPL Coupon

For most test directions, however, this arrangement has a fatal flaw. Any displacement that requires that more than one of the degrees of freedom of the nodes on the boundaries be fixed will cause a shear discontinuity along that edge. Disagreement between shear strains as determined by fixed displacement of the nodes and those determined by mathematical distortion of the model causes an irremovable but artificially induced stress concentration. With a coupon designed to direct stress concentrations into a specific location, this is unacceptable. Tabs were added to the model to separate the shear discontinuity from the gage area. These tabs rely on Saint Venant's principle to distribute the singular loads across the coupon but the length of the tab must be balanced with the tendency of a long beam to carry shear loads in bending. The actual boundaries of the gage section of the tabbed coupon are highlighted in red in the figure below.

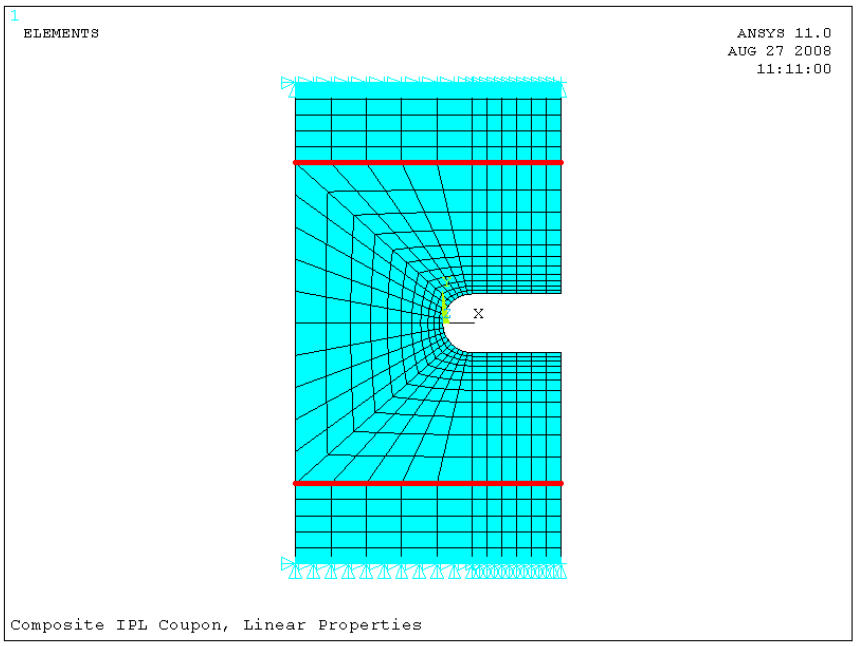

Figure 11. Notched Coupon with Tabs

A tabbed FEM creates its own set of problems. To avoid local singularities within the gage area, a routine must be introduced to accurately recreate the gage displacements by displacing only the tabs. This is not a trivial task for an asymmetric coupon under multiaxial loading. The first logical approximation is to assume the displacements for a tabbed but unnotched coupon with no edge effects. Because the deformation of such a coupon would be uniform, the displacements for the gage area would be a fraction of the displacements of the tabs—that fraction being equal to the gage length divided by the full length of the tabbed coupon. This serves as the initial guess for an iterative process for the nearest possible recreation of the gage displacements. An improved guess is formulated by subtracting the difference between the actual displacement and the target displacement from the previous guess. While this step alone is convergent,

the speed of convergence can be improved by scaling that difference by the gage length fraction. Convergence can only be assumed when the change is less than a predefined limit, for which a small fraction of the total displacement was used.

$$\vec{u}_{tab}^{\,j+1} = \vec{u}_{tab}^{\,j} - \frac{l_{gage} + 2l_{tab}}{l_{gage}}\left(\vec{u}_{gage}^{\,j} - \vec{u}_{gage}^{\,target}\right) \tag{23}$$

Problematic to the above equation are the actual gage displacements since they are now internal to the FEM and therefore susceptible to deformation. They too must then be approximated. The horizontal u and vertical displacement v can be approximated by taking the average of the displacements of all of the nodes along the boundaries of the gage area. However, since a uniform distribution of nodes is unlikely due to a mesh adapted to the notch, the average must be weighted according to that distribution x.

$$\bar{u} = \frac{\frac{1}{2}(x_2 - x_1)u_1 + \frac{1}{2}\sum_{i=2}^{n-1}(x_{i+1} - x_{i-1})u_i + \frac{1}{2}(x_n - x_{n-1})u_n}{x_n - x_1} \tag{24}$$

An identical mean exists for the vertical displacement v. Calculating the actual rotation of the gage area is slightly more complicated in that a line must be fit through the displaced nodes using linear least squares. The weighting factors from equation (24) can be used to establish a weighted objective function. It has been shown that this function is still a best linear unbiased estimator if each weight is proportional to the reciprocal of the variance of the measurement. Since variance diminishes proportionally to the sample size and the sample size here is

equivalent to the length of the boundary represented by the node, the above weights satisfy that criteria. [24]

$$f(\vec{\beta}) = \sum_{i=1}^{m} W_i r_i^2 \text{ where } r_i = v_i - m(x_i + u_i) - b \tag{25}$$

The intercept *b* of this line is not used since the vertical displacement has already been found, but the slope *m* can be used to calculate the angle of deflection at both edges. However, a rotation in the IPL is a pivot of the top grip around the center of the coupon. Motion of the virtual bottom grip must then be accounted for in the true gage displacements. Theoretical displacements for the top grip are found based on rotation alone, then those are subtracted from the actual displacements at the top grip. A final rotation is then applied to orient the displacements with the bottom grip as a reference.

$$\theta = \theta_t - \theta_b = \arctan(m_t) - \arctan(m_b)$$

$$\begin{Bmatrix} u \\ v \end{Bmatrix} = \begin{bmatrix} \cos\theta_b & -\sin\theta_b \\ \sin\theta_b & \cos\theta_b \end{bmatrix} \begin{Bmatrix} \bar{u}_t - \left(\bar{u}_b + \frac{l}{2}(\sin\theta_b + \sin\theta_t) \right) \\ \bar{v}_t + l - \left(\bar{v}_b + \frac{l}{2}(\cos\theta_b + \cos\theta_t) \right) \end{Bmatrix} \tag{26}$$

Not surprisingly, resultant tensile and shear loads must also be rotated to the coordinate system of the bottom grip and the moment on the coupon must be translated such that it is concentric with the presumed rotation. While it may seem unwieldy, the boundary displacement convergence algorithm is needed to facilitate the tabbed model that liberates the predicted data from significant

numerical artifacts. Figure 12 shows the difference in the strain fields between a tabbed coupon under shear and an equivalently displaced coupon without tabs. Not only has the maximum strain shifted from the notch to one of the corners, but there are also visible discontinuities between elements that have propagated out from the singularities. Peripherally, the algorithm also adapts readily to hastening the convergence of nonlinear material models that will be seen in Chapter 7.

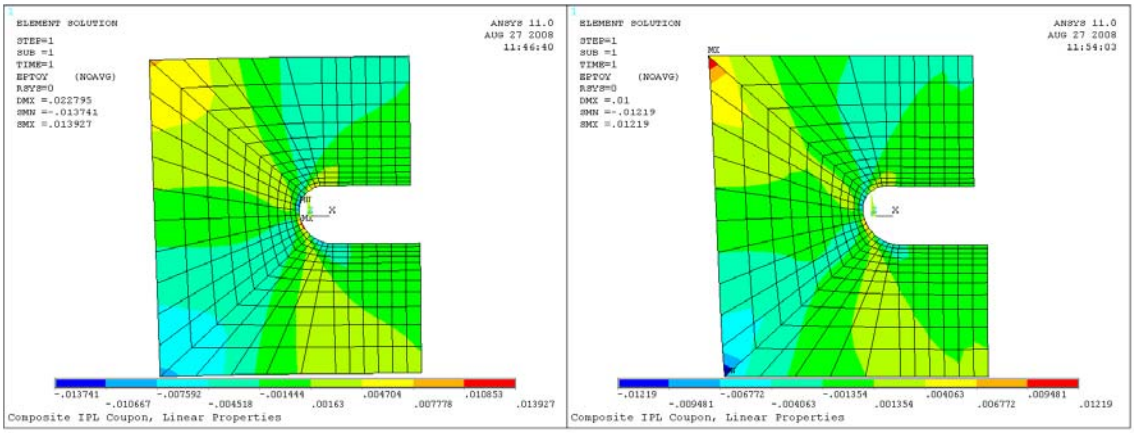

Figure 12. Coupon in Shear with and without Tabs

Optimized Results

Coupon stiffnesses in the displaced directions were used as the basis for the residuals for this phase of the optimization. With no displacement, stiffness values are not available in the other directions despite the presence of loads. Loads were not used directly for two reasons: load data from the IPL can be erratic in directions with no displacement and the magnitudes of loads in different directions and from different tests can vary greatly which will

inadvertently bias the residuals. Stiffness values for the tests were found through inspection and curve fitting of the linear portions of the IPL data after image correlation. The objective function is then the sum of the squares of the differences between observed and predicted coupon stiffnesses.

Once the model had been prepared parametrically with an objective function established, one of the optimization solvers needed to be chosen. As mentioned, the SAM is designed for speed whereas the FOM is designed for accuracy. To test these limitations, a simple model with only one design variable was optimized using each solver. The convergence of each is shown in Figure 13. Both methods converge on the same solution to within a very small tolerance. As expected, $n+2$ random design sets are evident at the outset of the SAM trial. With this number of steps, the FOM had already converged. Were the figure plotted versus time, it would be distinctly different. Where the ten steps of the SAM were performed in 1.7 hours, the three steps of the FOM concluded after 6.4 hours. Effectively identical detail from the First Order Method required a nearly fourfold increase in computation time. This factor is likely to increase as more design variables are included since calculation of the gradient requires a numerical derivative in each design direction. With no appreciable degradation in accuracy and vast time savings offered by the Subproblem Approximation Method, it is the solver utilized for the remainder of this thesis.

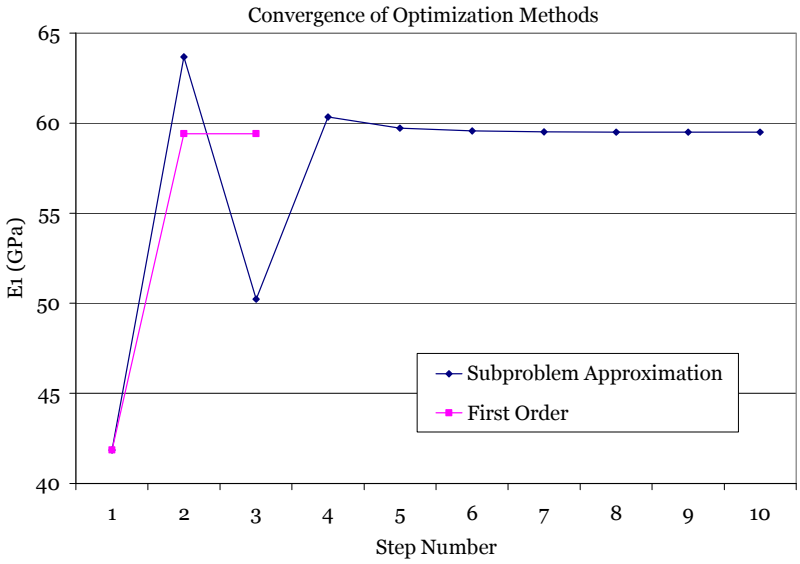

Figure 13. Convergence of Optimization Solvers

CDB200 Triaxial Fiberglass

Reasonably bounded optimizations provided no solution set that satisfactorily predicted the behavior of the fiberglass. Most results displayed properties that were pinned against the boundaries of the optimization. All results seemed to show inescapably that the predicted shear stiffness was double that observed. At first, this lead to doubt concerning the viability of simultaneous determination of elastic properties with high anisotropy; in eventuality, it garnered suspicion about the composition of the fabric.

This suspicion came to fruition when it was uncovered that the off-axis plies consist of a different material. Optimizing the properties of a fabric composed of two materials would require twice the number of design variables, each of which would increase computation time and uncertainty. In order to maintain simplicity in this proof-of-concept, the fiberglass laminates were

abandoned in favor of the carbon fiber pre-preg. Also influential in this decision was the concurrence of the maturation of the image correlation process which required that a new batch of coupons be tested for verification of that technique.

IM7 8552 Carbon Fiber Pre-Preg

Almost immediately, processing of the carbon fiber laminate produced more promising results because of the consistency of the material and its properties. In all, seven load paths were used in the optimization and typical convergence times ranged from twelve to twenty hours. Convergence of each of the in-plane elastic constants can be seen in the figure below. Relative change is shown rather than the actual value because of the relative magnitude of the fiber direction modulus.

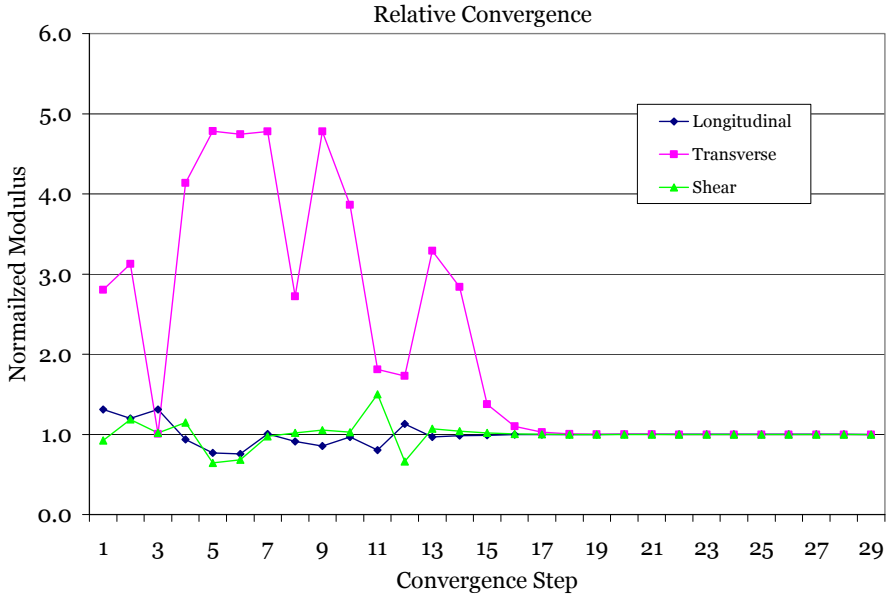

Figure 14. Relative Convergence of Elastic Properties

Pronounced changes in the transverse modulus are primarily a result of the less accurate initial guess but are also a consequence of the decreased sensitivity from high anisotropy. A comparison of the predicted and observed coupon stiffnesses can be seen in the following table.

Table 1. Optimized Coupon Stiffnesses

	Observed (kN/mm)		Predicted (kN/mm)		Difference	
Test	k_x	k_y	k_x	k_y	k_x	k_y
1	—	12.04	—	11.53	—	4.2%
2	3.59	—	3.21	—	10.6%	—
3	2.80	14.23	3.29	11.56	17.5%	18.7%
4	—	16.16	—	14.91	—	7.7%
5	1.91	—	3.18	—	66.6%	—
6	4.63	—	3.22	—	30.5%	—
7	1.51	11.73	3.18	14.98	111%	27.7%

As a whole, prediction of the behavior of coupons under tension is reliable. In shear, the errors vary by a much larger degree seemingly due to the inability of the model to capture changes in that direction under combined loading. While shear displacement and rotation appear to create additional modeled tensile loads, loads in the shear direction are only marginally affected by tensile displacement and rotation. This seems counterintuitive to the idea that the coupling should persist in both directions.

For validation, the optimized properties can be compared to those published by the manufacturer. The shear modulus and the Poisson's ratio are not presented in the datasheet for this material so they must be substantiated

using other sources such as the MSU Composite Material Fatigue Database [22]. In addition to reference materials, uniaxial tension tests were performed on several quasi-isotropic carbon fiber samples. The samples have in-plane isotropy due to a radially symmetric arrangement of plies: $[0/+45/90/-45]_s$. Using equation (1), the ply-averaged modulus of such a test can be predicted with both the published and optimized constants.

Table 2. Comparison of Carbon Fiber Results

	E_1	E_2	G_{12}	ν_{12}	Quasi-Isotropic
Optimized	146 GPa	12.8 GPa	4.17 GPa	0.322	63.2 GPa
Published	163 GPa	12 GPa	—	—	70.1 GPa
Observed	—	—	—	—	55.3 GPa
Difference	10.4%	6.67%	—	—	9.86%, 14.3%

According to the MSU Database, Poisson's ratios for carbon fiber laminates typically range from 0.30 to 0.35 and the shear modulus of most fabrics is roughly half of the transverse modulus. The optimized properties seem to coincide well with these trends, although changes in these values had very minor effects on the modeled results.

DISSIPATED ENERGY DENSITY

The experimental dissipated energy density function hinges on the assumption that the damage accrued by an element of material under pseudo-static loading is uniquely defined by the strain state in that element. Of course, it is easy to imagine that this would not be the case under any manner of cyclic loading or along a load path that involves substantial unloading. Still, a load path that begins at an unloaded state and follows an approximately linear path to its final state should produce a unique damage state. The uniqueness of the dissipated energy density as a function of the strain state is then not so much a matter of the strains themselves so much as the repeatability of the path to the strain state.

Piecewise and Global Approximations

As mentioned above, the purpose of the dissipated energy density method is to find a functional relationship between dissipated energy density and strain. For the purposes of this thesis, the function will be three-dimensional where the three dimensions are the three in-plane strains of the orthotropic composite lamina.

$$\phi = \phi(\varepsilon_1, \varepsilon_2, \varepsilon_{12}) \tag{27}$$

Unfortunately, a continuous function cannot be found experimentally, and there is no precedent for a post-damage function on which to perform curve fitting.

Therefore, an arbitrary function must be assumed and its parameters adjusted so that it provides the closest approximation to the actual, unknowable function. Several options exist for such a function. One of those options is a global nonlinear approximation; another is a piecewise linear approximation.

The piecewise and global approximations are analogous to linear and nonlinear finite elements, respectively, in that they both employ nodal values and interpolating shape functions. When the dissipated energy density method was first proposed by the U.S. Naval Research Laboratory [13], the global approximation was used, but both methods have advantages and disadvantages as summarized in the following table.

Table 3. Comparison of Approximation Functions

Global Nonlinear	Piecewise Linear
Constraining nodal values does not guarantee functional constraints since nonlinear shape functions often include regions that are negative or greater than one	Constraining functional values is as simple as constraining nodal values
Ostensibly more computationally complex	Simpler shape functions offset by additional nodes and searching
Produces higher order functional variations with error $O(h^n)$	First order interpolation has error $O(h)$ which is intrinsically less accurate
Fewer nodes are needed to represent the same space	Solution improves slowly with reduced nodal spacing h

Because it is physically impossible to produce a negative dissipated energy, it is critically important that the approximating function also be globally nonnegative. Primarily for this reason, a piecewise linear function was chosen for this work. It was originally assumed that no constraints would be needed since the experimental data provided only nonnegative dissipated energy values. Early analysis proved that assumption to be false and reinforced the decision to use the piecewise function. The reduction in computational complexity with linear elements would also ultimately prove very convenient.

Deconvolution

In evaluating the approximating function, the dissipated energy density φ at any arbitrary point ε is defined as the sum of the shape functions N evaluated at that point weighted by the corresponding nodal values β. The shape functions are only valid for the region enclosed by the associated nodes. For an arbitrary number of nodes, this equation takes the following form.

$$\phi(\vec{\varepsilon}) = \sum_i \beta_i N_i(\vec{\varepsilon}) \tag{28}$$

A rectangular hexahedral element will have eight nodes and so will have eight shape functions. Frequently, a transformation of coordinates is used to orient the space inside any particular element. In this case, the functions u, v, and w map the space in the ε_1, ε_2, and ε_{12} directions linearly to reside between -1 and 1. In this manner, the shape functions take on a very simple form.

$$N(\varepsilon_1, \varepsilon_2, \varepsilon_{12}) = \frac{(1 \pm u(\varepsilon_1))(1 \pm v(\varepsilon_2))(1 \pm w(\varepsilon_{12}))}{8} \tag{29}$$

The parities of the operators inside the expression vary in such a way that the value of the shape function is 1 at the associated node and 0 at any of the other nodes. This guarantees that the functional value at the node is precisely the nodal value.

What is problematic about this method is that it is the nodal values that are unknown. The only experimental data that is available for this method is the total dissipated energy from coupons with known boundary displacements. The total dissipated energy, however, is no more than the accumulation of dissipated energy in the microscopic parts of the coupon. While it would be nearly impossible to integrate the dissipated energy over the continuum of a coupon, it can be broken down into smaller elements: finite elements, as it were. The finite element model described in the previous chapter is used to bridge the gap between the macroscopic dissipated energy data and the unknown dissipated energy density.

For a composite laminate, though, the strain state in an element is not the same as the strain state in a single ply, at least not when put in terms of that ply's principal directions. In order to represent the true orthotropic material, the element strains must be rotated to the material orientation using the strain transformation equations. In this way, the solution represents the material rather than the layup.

$$\begin{Bmatrix} \varepsilon_1 \\ \varepsilon_2 \\ \varepsilon_{12} \end{Bmatrix} = \begin{bmatrix} \frac{1+\cos 2\theta}{2} & \frac{1-\cos 2\theta}{2} & \sin 2\theta \\ \frac{1-\cos 2\theta}{2} & \frac{1+\cos 2\theta}{2} & -\sin 2\theta \\ -\sin 2\theta & \sin 2\theta & \cos 2\theta \end{bmatrix} \begin{Bmatrix} \varepsilon_x \\ \varepsilon_y \\ \varepsilon_{xy} \end{Bmatrix} \tag{30}$$

Once the strains have been rectified for the various plies, the total dissipated energy can be written as the sum of the dissipated energies from the plies of the elements of the coupon.

$$\Phi = \sum_e A_e \sum_p t_p \phi\left(\vec{\varepsilon}_{e,p}\right) \tag{31}$$

Since the dissipated energy density is, in fact, a density, it must be weighted by the volume it represents shown as the element area and ply thickness above. Remembering that the dissipated energy density is itself a summation, the total dissipated energy can be further expanded.

$$\Phi = \sum_e A_e \sum_p t_p \sum_i \beta_i N_i\left(\vec{\varepsilon}_{e,p}\right) \tag{32}$$

Now that the total dissipated energy is in its fully expanded form, it can be rearranged so that the unknown nodal values β_i take center stage.

$$\Phi = \sum_i \beta_i X_i \text{ where } X_i = \sum_e \sum_p A_e t_p N_i\left(\vec{\varepsilon}_{e,p}\right) \tag{33}$$

In this simplified form, it becomes clear how the macroscopic dissipated energy can be used to approximate the nodal values. With i or more total

dissipated energy values with differing associated elemental strains, a system of equations arises that can be solved using linear least squares. For a single linear element, that solution would be both very uninteresting and very poorly suited for an accurate portrayal of dissipated energy density throughout the strain space; on the other hand, if several elements are combined in an array with the proper arrangement and constraints, an interesting picture emerges.

Data Distribution

Two techniques are used to provide the necessary data for an adequate least squares fit. Primarily, multiple experimental tests are performed along varying load paths to provide diversity in the acquired strain data. Since the strain space defined by the elements is rectangular in all directions, it would be ideal if the points representing the in-plane strains of the finite element model completely and uniformly filled the strain space. This is not a realistic goal. The purpose of a notched coupon is to concentrate damage at the tip of the notch. The notch is an irremovable part of the coupon design because without it damage would be focused around the grips where the loading conditions are much more complicated with considerable out-of-plane components. Because of the concentration, however, the strains at the notch are many times higher than the strains in the rest of the coupon that largely maintain an elastic response. Consequently, the vast majority of the strain points are relatively near to an unstrained state: the origin in strain space. In Figure 15, a histogram of the data points for a 4×4×6 arrangement of elements is shown. The vast disparity between

populated, sparsely populated, and unpopulated nodes is clear. Of the 96 elements, 41 contain no data leaving 45 of the 175 nodes unrepresented.

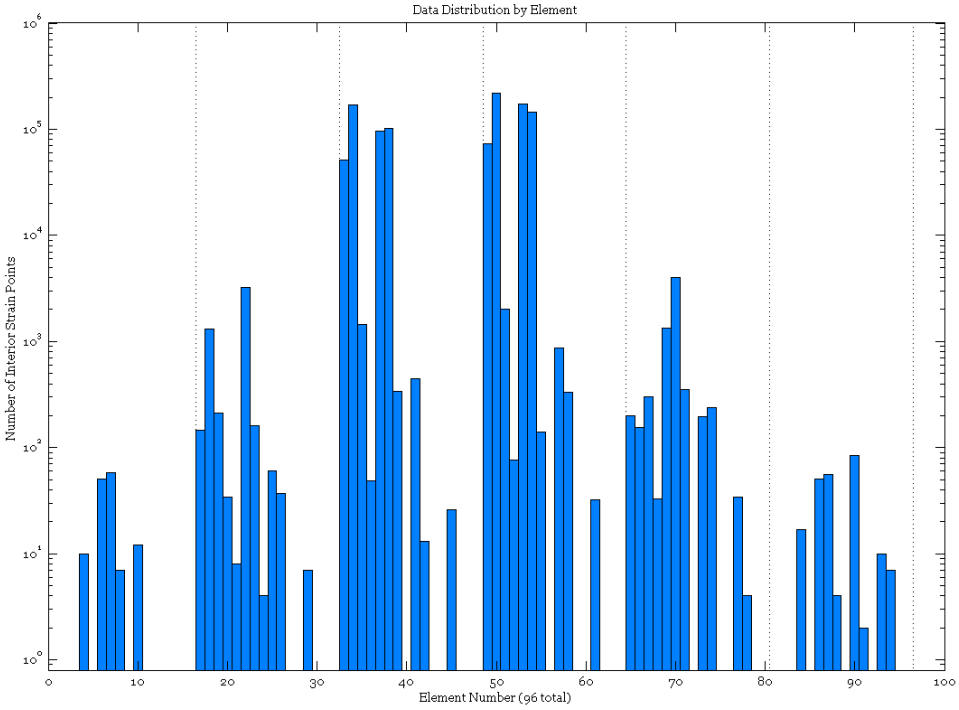

Figure 15. DED Function Data Points per Element

Initially, three linear finite element models were used to reconcile the calculation of strains for all of the tests. Since the IPL is capable of loading in the three in-plane directions, each of the three FEA models corresponds to one of those directions. Assuming that a linear strain response is satisfactory yields several computational advantages. A linear finite element model is linear with respect to any of the applied loads. That is, a load that is n times greater will result in an increase by a factor of n in the displacements and, therefore, the strains. Linear finite element models are then, not surprisingly, linearly independent. Furthermore, this fact is indicative of the applicability of the

principle of superposition. By running three independent FEA models, the strain for any element at any displacement can be found by scaling and superposing the strains from the three linear models.

$$\begin{Bmatrix} \varepsilon_x \\ \varepsilon_y \\ \varepsilon_{xy} \end{Bmatrix} = \frac{u}{u_{ref}} \begin{Bmatrix} \varepsilon_x \\ \varepsilon_y \\ \varepsilon_{xy} \end{Bmatrix}_{u_{ref}} + \frac{v}{v_{ref}} \begin{Bmatrix} \varepsilon_x \\ \varepsilon_y \\ \varepsilon_{xy} \end{Bmatrix}_{v_{ref}} + \frac{\theta}{\theta_{ref}} \begin{Bmatrix} \varepsilon_x \\ \varepsilon_y \\ \varepsilon_{xy} \end{Bmatrix}_{\theta_{ref}} \tag{34}$$

While it is certain that the internal strains in a damaged sample do not coincide with the internal strains of an equally displaced undamaged sample, it is unclear whether those deviations are significant enough to affect the results of the dissipated energy density function. The argument for the use of the linear FEM is that, since accrued damage will be focused around the notch, most of the coupon is preserved in its linearity and continuity will force the degraded regions to deviate only slightly. Later, this argument will come under question and alternative approaches will be explored.

At first glance, the use of superposition appears to lend itself to infinite scalability whereupon coupon displacements could be tailored to fill any arbitrary strain space. Unfortunately, this is not the case as any one strain point intrinsically influences every other element in the FEM. Certain regions in the strain space can not be filled without expanding the boundaries of that space in undesirable directions, as can be seen in the Figure 16. Each point represents a data point in strain space, and the telescoping rays of points from the origin are the scaled strains that inadvertently expand that space.

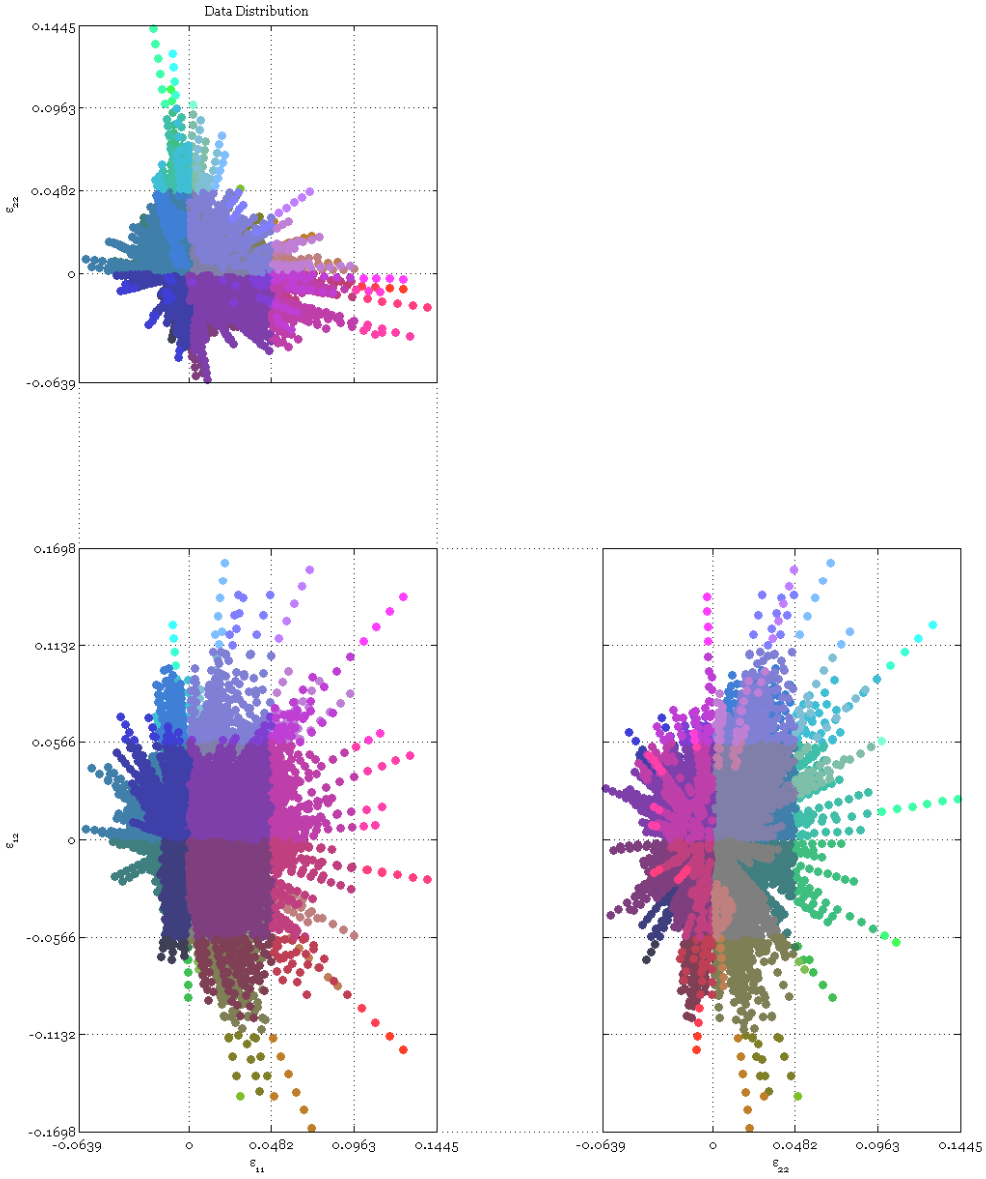

Figure 16. Actual DED Function Strain Distribution

That being the case, attempting to tailor the resultant strains provides little advantage over simply using an organized system of boundary displacements. Because the coupons are very thin compared to the gauge length, they are very susceptible to buckling so outright compression is excluded from all of the tests. Pure tension, pure shear, and pure rotation are the principal

components of the test set but are augmented by combinations of two and three directions. Those combinations are organized such that their “directions” are uniformly distributed in load space, although this is somewhat arbitrary except for bookkeeping purposes.

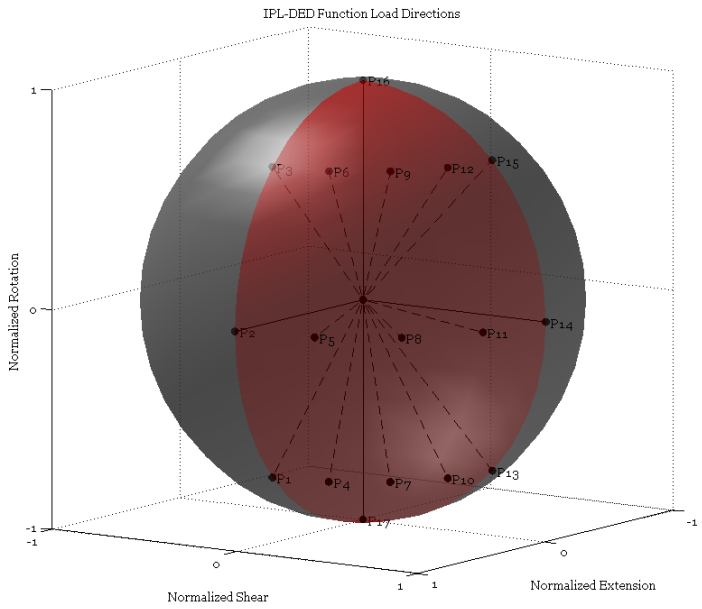

Figure 17. IPL Load Directions for DED Function

The second technique used to ensure an adequate number of strain points for an overdetermined solution is interpolation of the path data. By design, the IPL acquires data in discrete steps that are chosen by the operator. Except in cases where catastrophic failure has occurred, interpolating between the measured data points is sufficiently close to creating data that was present but not recorded. For the most part, extreme damage events cause unpredictable behavior in the IPL and, generally, those data are truncated. Interpolating data points is accurate and reliable and, unlike including additional load paths, does

not encroach upon existing solution space boundaries. Unfortunately, it does not add any particularly compelling new information to the system and so should be used as a contingency.

Constraints

In theory, no constraints should be required to obtain a physically realistic solution. The most likely solution should correspond with the true solution if the method is viable. Due to imperfect data and the finite precision of discrete elements, however, unconstrained solutions display physically unrealistic properties. It does, of course, provide the literal best fit to the data, but when the solution is taken out of the context of the optimization set, results deviate from gathered data by absurd amounts. Any constraints placed on the solution set will move the solution away from the least squares solution, reducing the correlation between the predicted data and the experimental data, but doing so is an essential step towards a database that is applicable to any circumstance other than the layup, geometry, and loading already tested.

The anticipated shape of the DED function starts with a small undamaged region encompassing the origin. With no damage, there is no dissipated energy. Intuitively, the shape of the undamaged part of the function should take a shape similar to those described by the failure envelopes described in Chapter 2. Surrounding this region of zero dissipated energy should be a region of progressive damage, itself surrounded by the maximum possible damage that can be sustained by the material.

The first and most obvious constraint that must be applied to the dissipated energy density values is that they be nonnegative. Negative dissipated energy values are a violation of the second law of thermodynamics but frequently appear in unconstrained solutions. If zero is the lower bound for dissipated energy, then the upper bound is the strain energy for an equivalently displaced elastic element. This bound is excessive in the sense that the dissipated energy density should actually be nowhere near that level. Only if an element were to be loaded completely elastically then utterly pulverized would this energy state be possible, and any further displacement would result in zero additional damage energy. The maximum theoretical strain energy density is a function of the stresses and strains within an element; however, since the stresses in an elastic material are a function of the strain state alone, the strain energy can be calculated knowing only that.

$$0 \le \phi(\vec{\varepsilon}) \le w(\vec{\varepsilon}) \text{ where } w(\vec{\varepsilon}) = \frac{1}{2}\vec{\varepsilon}^{T}\vec{\sigma} = \frac{1}{2}\vec{\varepsilon}^{T}C\vec{\varepsilon} \tag{35}$$

Distribution of Nodes

Initially, the nodes of the DED function are dispersed regularly between the upper and lower bounds of the three directions in the strain space as defined by the provided strain data. The number of nodes is largely a matter of choice, but in general can be increased to improve the level of detail in the solution. That increase in precision does not come without costs: the most immediate of which being calculation time. There are other and possibly more dire consequences to

capriciously increasing the node count, but those will be discussed later in this chapter.

Arrangement of the nodes can be performed in a slightly more strategic manner than simply evenly between the bounds. The most significant adjustment that can be made is to force one node to be at the origin. In a state of zero strain, no displacement has taken place so no energy has been added to the element and, therefore, no energy has been dissipated. This is described by the constraints in equation (35) but, better yet, this node can be completely removed from the solution since it is known to be zero. Because the nodes are arranged orthonormally, requiring that a node be at the origin also requires that there be nodes along each axis and in the base planes. Comparisons to known uniaxial and biaxial properties are then made less cumbersome. In order to maintain low aspect ratios, the nodes on either side of all three base planes are also redistributed uniformly.

An alternative approach was used in a similar work performed by Will Ritter [8]. Rather than bounding the solution space by the maximum strains that occur in the FEA, a set of bounds was predetermined by the user. Values for the DED of strain points that lie outside of those bounds were assumed to take on the same value as the nearest node. The motivation behind this method lends from the anticipated shape of the DED function. If there exists a boundary after which no additional energy can be dissipated, then limits placed outside that boundary should have no adverse effect on the solution. Restricting the solution space in this manner could increase the density of nodes and the precision of the solution

where the experimental data are most populous. However, because discovering the surfaces that correspond with damage initiation and catastrophic failure is of interest to this study, this method was not used. The catastrophic failure envelope is entirely unknown, so imposing any bounds would be a matter of pure speculation. Avoiding this method also removes any concerns that arise from the implementation of extrapolation.

Comparison of Solution Sets

The entire solution process as outlined in the previous sections is diagramed in Figure 18. All of the DED function solutions were obtained using MATLAB. Appendix B contains a substantial portion of the code used for these solutions, and the remainder can be seen in Jay Smith's thesis [15]. In addition, all of the solutions are for the CDB200 Triaxial material.

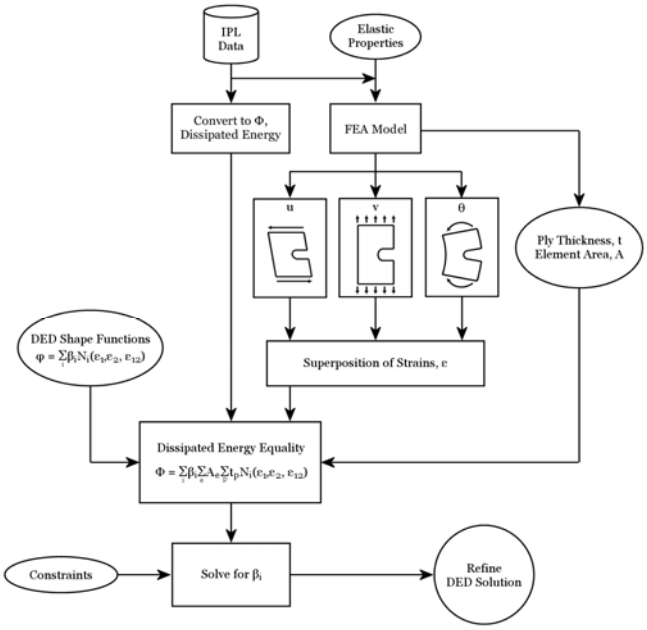

Figure 18. DED Function Solution Process

Unconstrained and constrained solutions can be seen for comparison in Figure 19 and Figure 20, respectively. Slices were made through the base planes in each figure.

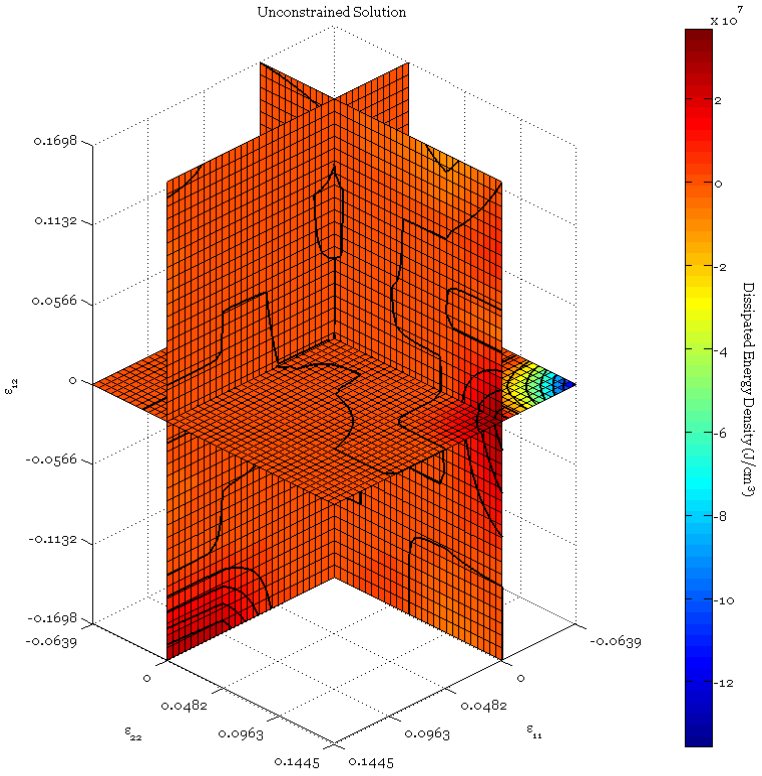

Figure 19. Unconstrained DED Solution

The unconstrained solution displays none of the properties of the anticipated functional shape. It severely violates the principle that dissipated energy cannot be negative. The solution space is dominated by zero and near-zero values with what appear to be randomly distributed hot and cold spots. Of course, the unconstrained solution does produce the most accurate reproduction of the input data, as can be seen in Figure 21. In this case, however, what is—by the definition of the least squares method—the most probable solution does not correspond

with the most realistic solution. Constraints are clearly necessary for a more satisfying result.

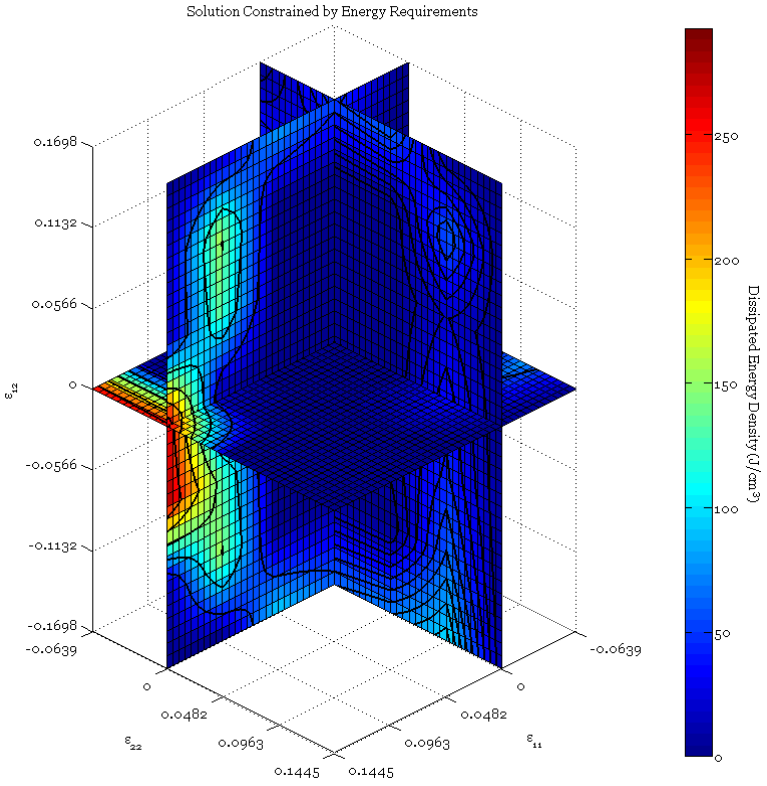

Figure 20. DED Solution with Energy Constraints

In Figure 20, constraints help to form the expanding shells that represent increasing dissipated energy density. While not as close as the unconstrained solution, the constrained solution has relatively high correlation with the experimental data, which can again be seen in Figure 21. Nevertheless, the solution is not perfect. Many of its flaws are covered later in this thesis and possible remedies are suggested.

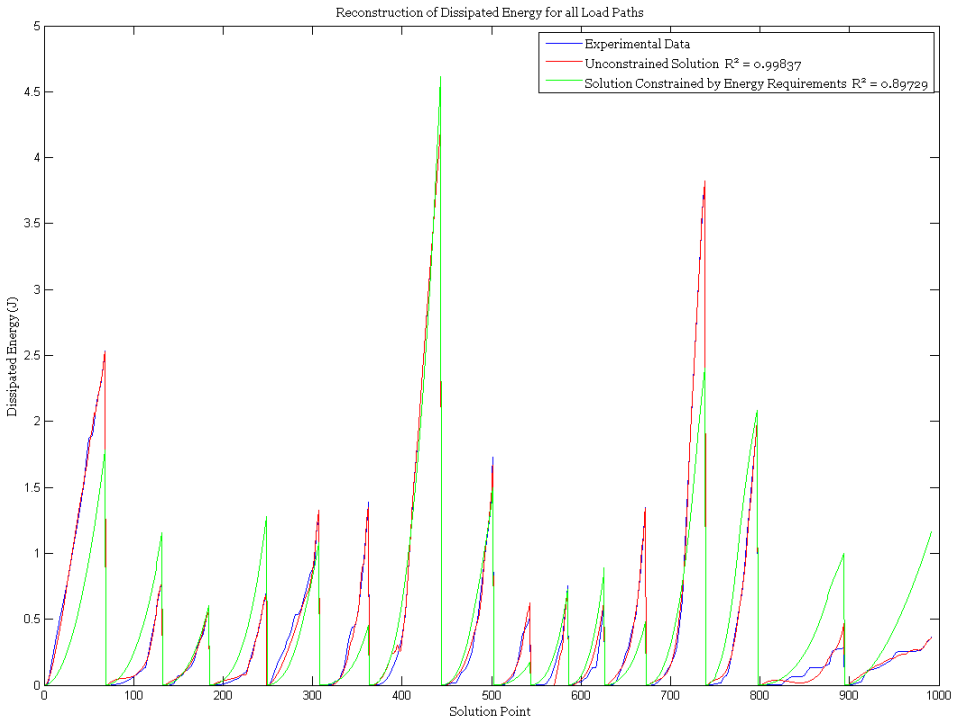

Figure 21. Reproduction of DE from DED Solutions

Damage Initiation Isosurface

Aside from the DED information itself, another result of primary interest is the surface within the DED function that represents the point at which the material response has change from elastic to some unknown nonlinear form. This surface shall henceforth be referred to as an isosurface since, using only dissipated energy data, there is no better metric for a damage initiation surface than a constant value of DED. Ideally, the isosurface would correspond with some degree of accuracy to one or more of the damage models described in Chapter 2. In reality, however, the shape encountered is irregular when compared to the shapes formed by other damage envelopes. When designing a structure, finite element modeling could reveal the strain states of elements

within the structure which, if found to exceed the boundary of the purely empirical damage initiation isosurface, could then be assessed as regions of potential damage.

Because of the linear piecewise nature of the DED function, there is no clear distinction between damaged and undamaged strain space. Therefore, it is necessary to assume some level of dissipated energy density at which damage initiation has occurred. For instance, a small fraction of the maximum observed DED can be used to form the isosurface. Alternatively, the dissipated energy density found at a location that is otherwise known to be damaged can be used for this value; the strain to failure in the fiber direction is such a location.

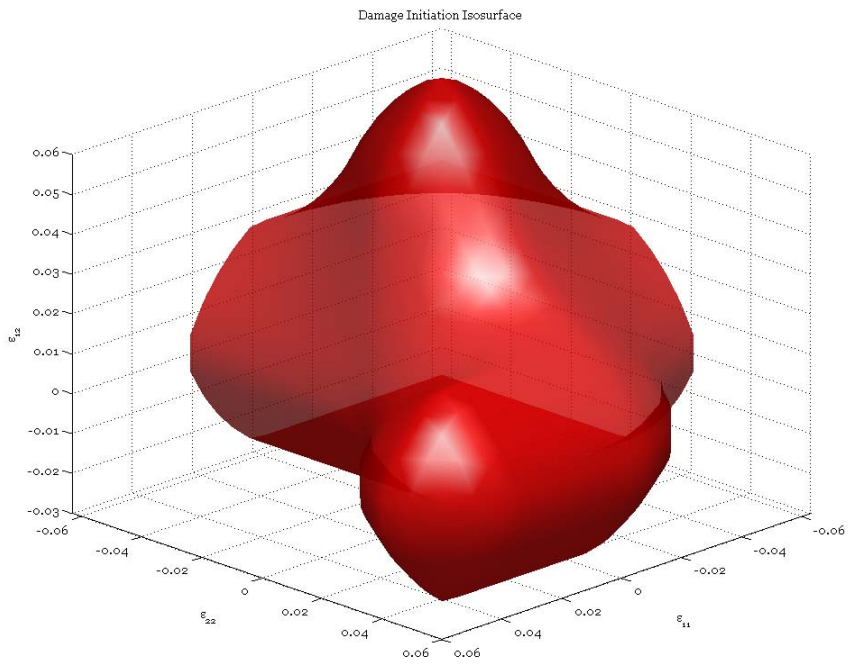

Figure 22. Initial Damage Surface Based on Longitudinal Tension

CDB200 Triaxial fabric is known to fail in tension in the fiber direction with strains between 2.49% and 2.98% [22]. Based on the values of the DED in this

range, the isosurface in Figure 22 was formed. The isosurface exceeds the bounds of the solution domain in both compressive directions. Intuitively, the strain to damage should be highest along the axes of the strain space, which appears to be the case with the shear axis. The peaks in the longitudinal and lateral directions are slightly offset from this ideal, however, and the reason is unknown.

Inconsistencies and Modifications

The most obvious flaws with most of the data sets are the large regions of low DED near the edge of the strain space. This is not a result of the data so much as it is of the lack of data. As mentioned, most of the experimental data are clustered around the origin. Such a distribution leaves many of the outer elements sparsely populated or completely unpopulated. A single unpopulated element is not necessarily the cause of a low-valued region as each node is associated with up to eight elements. Nodes with no data associated with them, however, will form a null space in the least squares solution and will be overlooked when solved with a constrained solver or singular value decomposition. When such a situation arises, the nodal value is set to zero by default. This is merely a computational artifact, but it leads to a physically unrealistic solution where regions of low dissipated energy density follow or are nestled within regions of higher DED.

Recreating the original experimental dissipated energy paths provides no diagnosis for this problem since every strain point needed for the recreation was one used to build the DED function. It is then somewhat of a misleading metric

for the quality of the function. When the DED function is used to predict the damage response for any path that was not part of the original data set, the zeroed nodes can be disastrously detrimental to that end. Several corrective measures were employed in an attempt to remedy this flaw.

Finite Difference Weighted Average

The first attempt to fill the voids left by insufficient data assumes that the DED function has a high degree of local consistency. Physically, this assumption seems safe because of the function's anticipated shape. Also, since each element is approximated using linear shape functions, it is no less valid to assume linear variation across multiple elements.

Each of the nodes—except the nodes on the boundaries—has six nearest neighbors. In an analogy to a finite difference steady-state heat transfer problem, each node can be imagined as being surrounded by a rectangular prism that is abutted by the prisms of the six neighboring nodes. Some of the nodes have known nodal values determined by a least squares solution while the rest have zero values which are effectively unknown as the zero value is assigned arbitrarily to nodes which have no associated data.

Proceeding from a least squares solution, the set of nodes n is broken down into the subset of known nodes k and the subset of unknown nodes u. For each unknown node, it is assumed that the node is influenced by its set of neighboring nodes i proportionally to the area of the face of the prism between the nodes but inversely proportional to the distance between the two nodes.

Again, this is analogous to Fourier's law of heat conduction where the net flow of influence into and out of the surface surrounding the node is zero, but it results in what is merely a weighted average.

$$\sum_i A_i \frac{\beta_u - \beta_i}{\varepsilon_u - \varepsilon_i} = 0 \tag{36}$$

For each unknown node, an equation arises that is linear with respect to the other nodal values. However, some of those nodal values are known while others are not. It is therefore convenient to break up each of u equations into its unknown and known components k.

$$\sum_{j \subseteq u} c_j \beta_j = \sum_{j \subseteq k} c_j \beta_j \text{ where } c_i = \pm \frac{A_i}{\Delta \varepsilon_i} \tag{37}$$

What arises is then a fully determined set of u linearly independent equations for the set of u unknown nodal values. Solving this set of equations provides values for the unknown nodes and smoothes the solution set as much as possible with the given data.

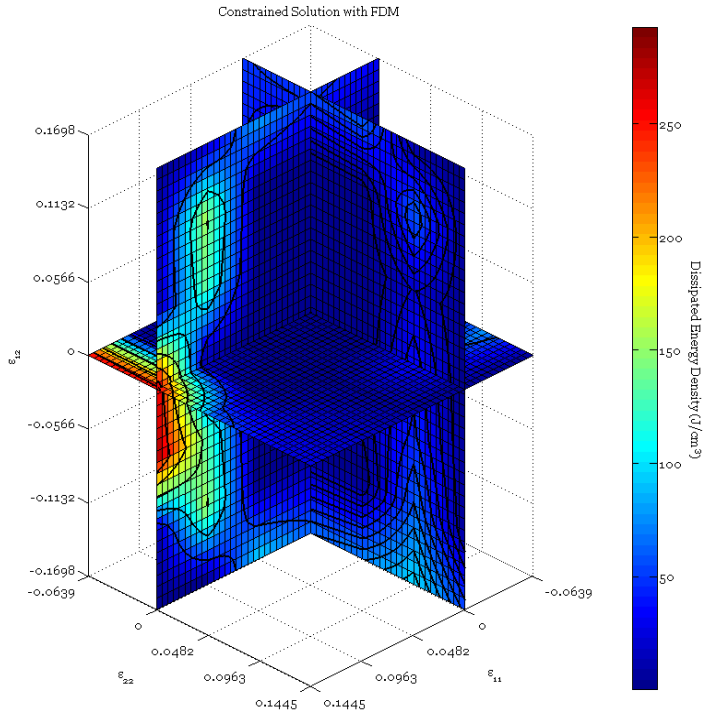

Figure 23. DED Solution with Void Approximation

The difference between Figure 20 and Figure 23 is subtle but significant. Where the uncorrected solution has nearly unchanged DED values on paths out to the boundary of the solution space, the void-corrected set better encloses low DED regions inside of higher ones. While this has no impact whatsoever on the reproduction of load paths included in the solution process (i.e., Figure 21 is not affected), it could make a tremendous difference in predicting the behavior of other load paths and geometries.

Symmetry in Shear Strain

In previous works, positive and negative shear have always been considered independently [8,15]. Altering this arrangement could not only double the amount of available data, but could also create a more physically realistic

DED function. If the axis that represents the shear strain instead accounts for the absolute value of the shear strain, then all values below the zero plane are reflected above it. This action effectively doubles the density of strain points. In addition, it removes almost half of the nodes, reducing solution time or allowing those nodes to be redistributed in the positive half of the solution.

The justification for using a solution that is symmetric in shear is as simple as considering the strain state of an element in ply principal axes. Any strain state in any arbitrary orientation can be transformed to this coordinate system using equation (30). In ply principal axes, regardless of the condition of either normal strain, positive and negative shear strains form mirror images of one another. Therefore, a strain state with negative shear is equivalent to viewing the same strain state with positive shear from the other side of the laminate. Due to that symmetry, the actual state of strain is irrespective of the sign of the shear. The effects of the sign of shear outside of ply principal axes are then redirected to the difference in tensile and compressive strength of the fiber and transverse directions in ply principal coordinates.

Alternatively, consider an infinitesimal change in the strain energy density of an element of an orthotropic material where both the strain vector and the components of the stiffness tensor depend on some arbitrary path variable p.

$$dw = \vec{\sigma} \cdot d\vec{\varepsilon} = \left(\varepsilon_1 C_{11} + \varepsilon_2 C_{12}\right) d\varepsilon_1 + \left(\varepsilon_1 C_{12} + \varepsilon_2 C_{22}\right) d\varepsilon_2 + \varepsilon_{12} C_{66} d\varepsilon_{12}$$

$$dw = \left(\varepsilon_1 C_{11} + \varepsilon_2 C_{12}\right) \frac{\partial \varepsilon_1}{\partial p} dp + \left(\varepsilon_1 C_{12} + \varepsilon_2 C_{22}\right) \frac{\partial \varepsilon_2}{\partial p} dp + \varepsilon_{12} C_{66} \frac{\partial \varepsilon_{12}}{\partial p} dp \tag{38}$$

Were the sign of the shear strain reversed, all of its contributions to the strain energy density would remain unchanged.

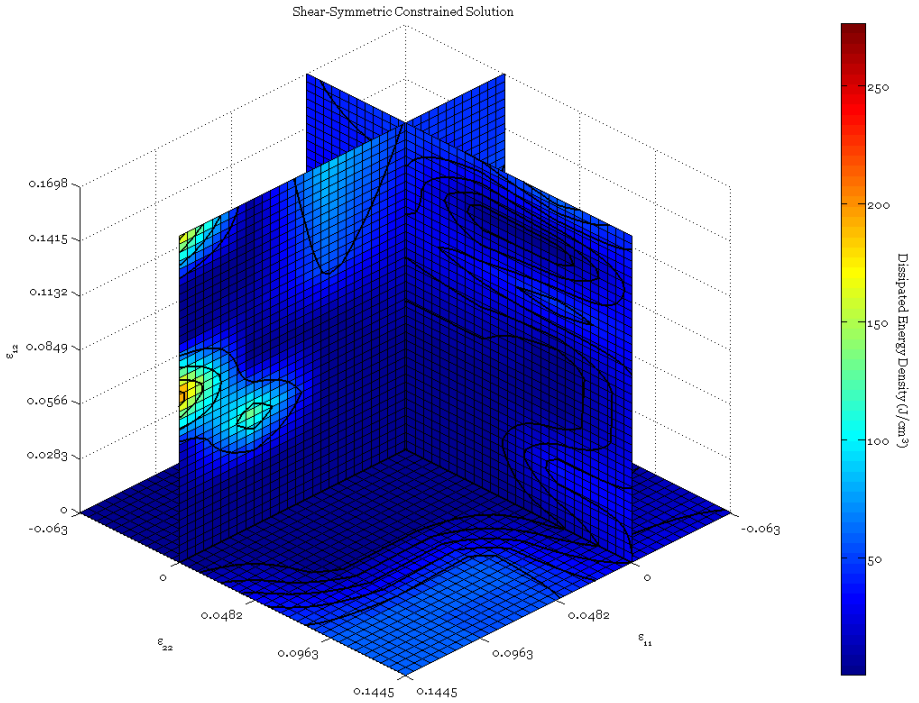

Figure 24. DED Function with Shear Symmetry

Constrained Gradient

In an attempt to combat the lack of association between the strain points defined by the coupon elements and the nodal unknowns of the outer DED function elements, an additional constraint was considered. As mentioned before, it is physically impossible for a decrease in dissipated energy to occur along a load path. This is equivalent to saying that the slope of a dissipated energy path must be nonnegative at all points. The same is true of dissipated energy density, although the definition of “path” and “slope” are much more difficult to interpret in a three-dimensional strain space.

Ideally, the change in dissipated energy density between a point and any subsequent point on a load path should always be nonnegative. Of course, this cannot be possible with a deterministic, single-valued function since returning along a path will always produce the opposite change as proceeding along it. Fortunately, of interest here are only those paths which do not undergo significant unloading. The difference between loading and unloading, however, is ambiguous at best. One of the most true-to-form distinctions would be that any direction in which elastic strain energy would be increased can be considered a loading direction. The direction of the maximum increase in elastic strain energy at any point in strain space can be found by taking the gradient of equation (35). Since the stiffness tensor is symmetric, the gradient of the quadratic form is remarkably simple.

$$\vec{\nabla} w = \vec{\nabla}\left(\frac{1}{2}\vec{\varepsilon}^{T} C \vec{\varepsilon}\right) = C\vec{\varepsilon} \tag{39}$$

On a local scale, any motion from the strain point in a direction that is more than 90° from the direction of the strain energy gradient at that point will result in unloading. What is desired is a constraint on the dissipated energy density function that will produce only positive changes in loading directions. In a likewise manner, those changes are described by the gradient of the DED. The DED function, however, is both discrete and unknown, so its gradient must be defined using finite difference analysis of the unknown nodal values. First order central differences were used to approximate the partial derivatives at the

nodes—except at the boundaries of the solution domain where only forward/backward differences are available. Here, a three component notation is used to orient the nodal values in strain space, but that must eventually be converted to the global notation for eventual solution.

$$\vec{\nabla}\phi = \left\{ \begin{array}{c} \dfrac{\partial \phi}{\partial \varepsilon_1} \\ \dfrac{\partial \phi}{\partial \varepsilon_2} \\ \dfrac{\partial \phi}{\partial \varepsilon_{12}} \end{array} \right\} = \left\{ \begin{array}{c} \dfrac{\beta_{i+1,j,k} - \beta_{i-1,j,k}}{2\Delta\varepsilon_1} \\ \dfrac{\beta_{i,j+1,k} - \beta_{i,j-1,k}}{2\Delta\varepsilon_2} \\ \dfrac{\beta_{i,j,k+1} - \beta_{i,j,k-1}}{2\Delta\varepsilon_{12}} \end{array} \right\} \tag{40}$$

While it is certainly not the case that the gradients of the elastic strain energy and the dissipated energy densities are collinear, a comparison of their directions can promote changes in dissipated energy in only loading directions. This is accomplished by means of the dot product. By definition, the dot product is related to the angle between two vectors in the following manner.

$$\vec{a} \cdot \vec{b} = \left|\vec{a}\right|\left|\vec{b}\right| \cos\theta \tag{41}$$

The least restrictive implementation of this constraint would be to require that the angle between the gradient of the strain energy density and the gradient of the DED be no greater than 90°—when the cosine is zero. While this does not ensure that all increases in DED be in loading directions (this can only be accomplished by setting the gradients as collinear), it does requires exactly that of the strongest changes. Unfortunately, the constraint cannot be made more

stringent by reducing the maximum allowed value for θ without creating a highly nonlinear inequality with respect to the solution vector.

$$\vec{\nabla} w \cdot \vec{\nabla} \phi > 0$$

$$\left(C\vec{\varepsilon}\right)_1 \frac{\beta_{i+1,j,k} - \beta_{i-1,j,k}}{\Delta\varepsilon_1} + \left(C\vec{\varepsilon}\right)_2 \frac{\beta_{i,j+1,k} - \beta_{i,j-1,k}}{\Delta\varepsilon_2} + \left(C\vec{\varepsilon}\right)_3 \frac{\beta_{i,j,k+1} - \beta_{i,j,k-1}}{\Delta\varepsilon_{12}} > 0 \tag{42}$$

Unfortunately, the combination of the gradient constraint with all of the other constraints proved to be too restrictive as a whole. Inequality constraints are very sensitive to initial conditions, and no initial condition could be found that created a convergent solution with the gradient constraint in place. This is not an indication that a solution of this form is unobtainable, only that an initial condition closer to the final solution must be found.

Unresolved Issues

Several issues continue to plague the DED function and hinder it from general utility. Some of these issues are inherent to the method and so are themselves irreconcilable. Others can possibly be resolved if they are supplemented with additional analysis and new technology. Much of this research is currently underway at MSU.

Recreation of Load-Displacement Curves

In converting load-displacement data to dissipated energy data, a considerable amount of information is lost. First, since there is no dissipated

energy associated with any elastic response, all information about the elastic stiffness of the material is lost. Secondly, all multi-axial tests—which originally have up to three independent load-displacement curves—are reduced to a single dissipated energy curve. The dissipated energy from the three curves is inseparable. Consequently, a dissipated energy curve that has been produced in order to predict the response of a material under multi-axial loading will never be able to demonstrate the response in any single direction. For this type of loading, the method is ultimately only appropriate for damage initiation and degree-of-damage type descriptions. The situation for uniaxial loading is only slightly more promising.

Since all elastic information is lost in the conversion from load-displacement to dissipated energy, the former must be supplied in order to recreate the latter. Compared to the difficulty in obtaining the DED function, however, this is only a minor inconvenience. To solve for a load-displacement curve based on the dissipated energy, the definition of dissipated energy for brittle materials must be reconsidered. The discrete form of this equation will be evaluated as it is more applicable to this situation.

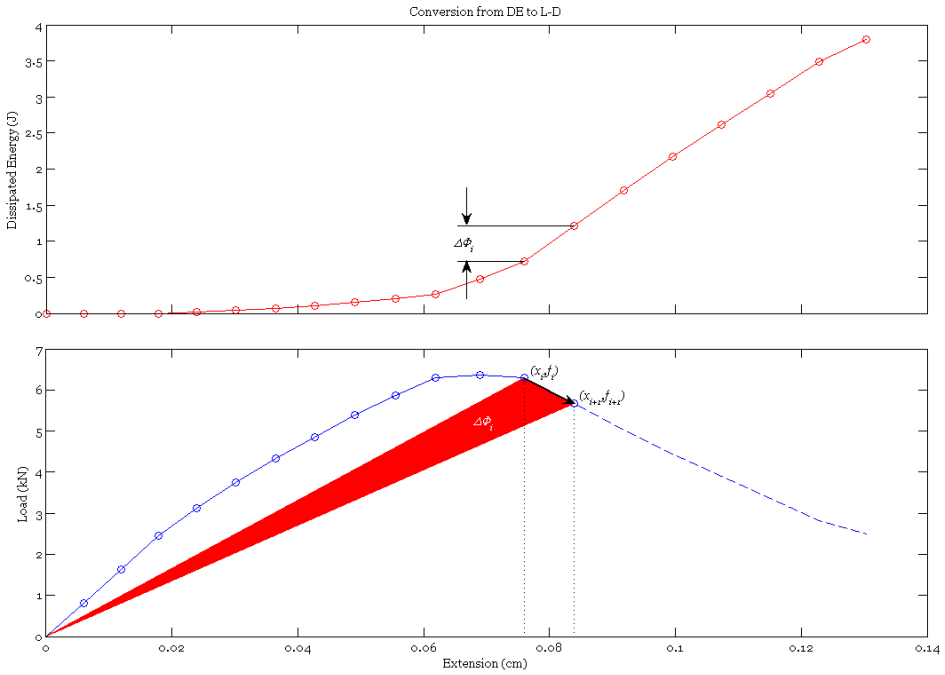

Figure 25. Converting Dissipated Energy Results to Load-Displacement

By this definition, the change in dissipated energy over one step is equivalent to the area of the triangle formed by the origin and the current and next load-displacement points.

$$\Delta\Phi_i = \frac{f_i x_i}{2} + \frac{(f_{i+1} + f_i)(x_{i+1} - x_i)}{2} - \frac{f_{i+1} x_{i+1}}{2} = \frac{f_i x_{i+1} - f_{i+1} x_i}{2}$$

$$f_{i+1} = \frac{f_i x_{i+1} - 2\Delta\Phi_i}{x_i} \tag{43}$$

The requirement that the elastic stiffness of the material be known is evident in the singularity of equation (43) when x_i is zero. An initial nonzero displacement point must be established and it must have an associated load, thus establishing an initial stiffness.

Even though it is possible to recreate L-D curves in this manner, curves generated from the DED function often exhibit erratic behavior due to high sensitivity to changes in dissipated energy, especially at low loads. Changes in dissipated energy at low loads are often exaggerated by the linear elements and accommodations must be made to reduce this effect. The most effective means of doing so is to assign a displacement under which no dissipation of energy is allowed, but this is very subjective and artificially imposes damage initiation criteria.

To test the ability of the DED function to recreate both dissipated energy and load-displacement data, testing and analysis were performed bearing strength tests following the ASTM standard for such tests in plastics [25]. These coupons were then modeled using ANSYS and the strains from that model were input into the DED function in an attempt to predict their total dissipated energy. Loading on the bearing surface was assumed to be frictionless with a cosine distribution achieving its maximum at the center of the pin.

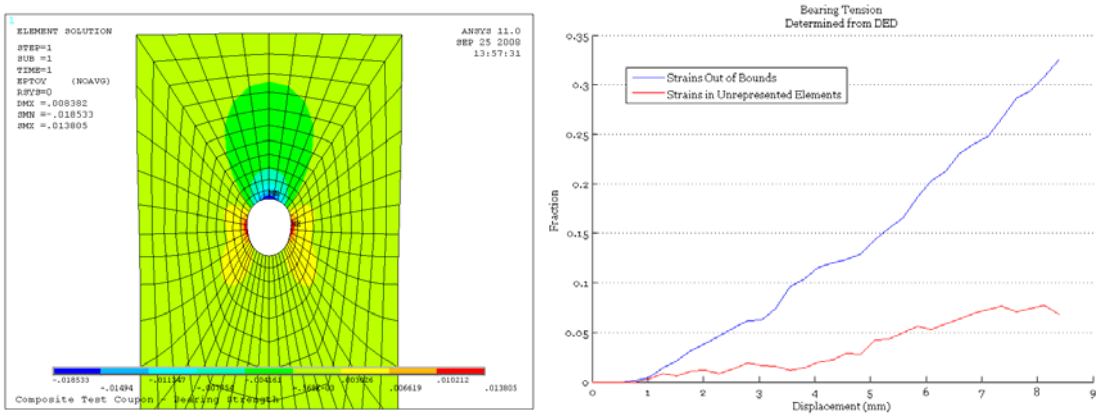

Figure 26. Comparison to Bearing Strength Tests

No DE or L-D data are shown because of the overwhelming number of strains in the FEM that were not represented by the DED function as shown on the right side of Figure 26. Primarily, this will need to be remedied by finding a way to include compression data in the database that forms the DED function.

Compromise between Detail and Representation

The misrepresentation of damage using orthogonal, linear elements can only be remedied by increasing the density of fitting function elements. Error in the approximating function is proportional to the size of the element, so a decrease by a factor of two in one of the dimensions of the element would theoretically double the accuracy of the solution. Such a change in all three dimensions would, therefore, increase accuracy by a factor of eight. Near the origin (i.e. inside and just outside of the elastic region), there should be only minor uncertainty in the values of the DED. Increasing the nodal density there would be greatly beneficial for the purposes of reconstructing load-displacement data and verifying the initial damage surface.

The density change, however, cannot be isolated to the elastic region while maintaining the rectangular arrangement of the nodes. A change in density must occur globally, but that change is not necessarily globally advantageous. Of course, an improvement in accuracy cannot be viewed as detrimental, but such an improvement is not nearly as significant in areas where uncertainty plays a larger role. There are also other consequences. Placing more elements in the already sparsely populated sections of the solution space only increases the

number of unrepresented nodes. While several methods for compensating for such nodes have been discussed, their effectiveness diminishes rapidly as the number of unknown nodes increases. A direct compromise between the detail and completeness of the solution then arises. This dilemma is an intrinsic part of the DED function as proposed. Only a fundamental change in the way the problem is posed could rectify this issue. Such a revision will be discussed later.

Improved Strain Determination

Crucial to the DED function are the values of the strains in the elements that compose the test coupons. As successively more refined solutions continue to fail to produce results that are coherent with experimental and theoretical models, the strains used to create the solutions come under question. With regard for the weight carried by this component of the data, many options have been considered that should improve upon the existing linear FEA data. There are two main concerns with the strain data. The first concern is that the displacements acquired from the IPL deviate from the actual boundary displacements of the coupon. The second concern lies with the adequacy of using elastic models to predict what is by definition an inelastic process.

Concerns about the accuracy of the displacement data from the IPL have largely been eliminated as a result of the image correlation tracking developed by John Parker. A direct analogy takes shape between the boundary displacements as found by the image correlation and those modeled with the tabbed FEM. In both cases, the points along the edge of the gauge section cannot be expected to

form a straight line. Instead, deformation that is not collinear with the gauge length occurs due to non-uniform compliance from the notched coupon and imperfect gripping. Compensating for this irremovable fact involves fitting a straight line to both the top and bottom grip edges and using that information to calculate the edge displacements of the coupon. Accommodation between the testing machine and the computational model is assured by providing both with the same method for calculating displacements.

Prior to the implementation of image correlation, the most promising option for improving the strain data was the use of nonlinear material models. A nonlinear material model is intended, in this capacity, to account for increased compliance in damaged elements where the actual strains would be higher than those predicted by elastic models. In doing so, however, the nonlinear model would have already accomplished what the DED function set out to do. Given this, the nonlinear material model distinguished itself as another possibility for a damage analysis tool. The project quickly took on a life of its own and is the topic of Chapter 7 of this thesis.

Image correlation, however, still holds much potential for the DED function. The same technique that tracks the motion of control points along the edges of the coupon can also track the motion of an indefinite number of interior points in the coupon. The locations of those points can be reconciled relative to the tip of the notch and, more importantly, numerical derivatives can be calculated to provide full-field experimental strain data. This method is currently being developed at MSU by John Parker.

Parker has shown that the error in determining the position of a displaced point is absolute in nature and is generally on the order of a fraction of a pixel. Error in IC strains is then proportional to the ratio between the absolute error of tracking a point and the required spacing between control points, both measured in pixels. For example, Parker currently uses a fourth-order central difference to calculate full-field strains. The error profile for this formula appears as follows.

$$\varepsilon_x(x) = \frac{u(x-2h) \pm e - 8(u(x-h) \pm e) + 8(u(x+h) \pm e) - u(x+2h) \pm e}{12h} + \mathrm{O}(h^4) \quad (44)$$

While the truncation error for a high order finite difference such as this is low, the uncertainty in the displacements of the control points leads to an additional error bounded by $3e/2h$, where e is the bound on error for an individual control point and h is the spacing between them. Since e is constant, the error bound on strains increases as the spacing between control points decreases. It is not known what level of refinement in nodal distribution will adequately dissect damaged from undamaged elements but, at some level, the miniscule size of the damaged elements will be overwhelmed by the mostly undamaged coupon. Due to the steadily increasing resolutions of commercially available digital cameras, however, this concern is ever-diminishing.

Misplaced Elemental Weight

The final major issue still plaguing the DED function is another that is possibly irresolvable. This issue comes about from the reminder of the necessity of small FEA elements in damage regions. Since composites are brittle materials,

cracking must be approximated by a series of failures in very small elements. The size of those elements is reflected in the weighting factors in equation (33). Cracking indicates that the cumulative damage in a coupon must all occur in a relatively small region. Using a least squares solution, elements with larger weighting factors will have proportionally larger residuals, thus removing the focus of the solver from the theoretically damaged regions. This problem stacks with the sparseness of high strain data to further obfuscate the solution.

Future Work

Because the focus of this project shifted so quickly to the creation of a nonlinear material model, there is still much work left to be done even in the context of what has already been discussed. Through that nonlinear material model, it was revealed that the CDB200 Triaxial material, used heretofore in all of the dissipated energy density calculations, is not composed of uniform plies—a fact not made widely available by the manufacturer and one that has gone unnoticed in several theses prior to this one. The Triaxial material is actually constructed out of two different materials; D092 constitutes the on-axis ply and the two off-axis plies are DB120. These materials not only have nontrivial differences in linear properties but also are laid out in different thicknesses—each off-axis ply being slightly greater than half the thickness of the primary ply. This says nothing of their assuredly dissimilar post-damage response. The material that was selected for its versatility and practicality was ultimately very poorly suited for the prototype of this process.

While not perfect, the material database is not entirely unusable for a trial run. Of the three problems stated above, the most egregious and, conveniently, the most easily corrected is the thickness of the plies. Where the element volumes were once calculated using a constant ply thickness, those thicknesses vary in the assembly of the DED function in equation (33). Also, those thicknesses and the linear properties were corrected in the three linear finite element models used to determine the elemental strains. For future works, however, a separate DED function should be created for the off-axis plies if the same test data are to be used. There would then be two completely autonomous functions that would need to be solved simultaneously. Solving such a set would be impractical and would add another uncertainty in a method that is already riddled with them. Fortunately, it is also unlikely considering the advancements in strain determination that have taken place since the time that database was produced.

Any future work on this subject should include at least three specified changes. The first is, for reasons just discussed, a layup that is a composition of uniform plies. Secondly, since strain tracking via image correlation is now an integral part of the IPL testing process, future DED functions should make use of in-situ strain data rather than depending on FEA (linear or nonlinear). Finally and most mindful of the nature of the DED function is the need for a fitting function element distribution that is more considerate of the distribution of the data and the anticipated shape of the function itself. Certain regions of the solution space are fundamentally more critical which should be reflected in the predicting function.

Non-orthogonal Elements

Insufficient available detail in the near-elastic region cannot be addressed without also taking into consideration the intrinsically coupled problem that is the paltry distribution of data in the remainder of the solution domain. Ideally, the solution to this dilemma is to have smaller, more detailed elements near the origin and to have the size of the elements progressively increase as they move further from that point. This cannot be accomplished using orthogonal elements. However, it does not preclude the use of brick-type elements. Removing the requirement that the elements be orthogonal has several effects.

First—and of the most immediate concern—is determining the inhabitation of the data points within the distorted elements. What could once be done using a global inequality would need to be done element-by-element using parametric location shape functions. Potentially, this could be avoided if the elements were arranged in a regular pattern, but an arrangement that is adaptive to the distribution of the data would be more beneficial. A three dimensional linear element with its eight vertices in arbitrary locations would require the solution of a set of cubic equations to map any arbitrary point to its local coordinate system. Two of the three solutions to that cubic set are an artifact of the overlapping basis vectors but, as long as one of the three solutions is within the bounds of equation (29), the point is within the element. The local coordinates found would then be associated with that data point for the remainder of the DED function solution. For a set of n data points in a solution domain consisting of m elements, mapping the global coordinates to the correct

local coordinate system involves solving, on average, $n \times m/2$ cubic systems. If the elements nearer to the origin were included at the front of the search pattern, then this number could be reduced; however, the number of elements is, by necessity, much smaller than the number of data points, which for many of the solutions seen has been over one million. Hopefully, the fixed increase in computation time would be outweighed significantly by the improved quality of the solution.

The primary benefit of irregularly shaped elements is the possibility of degenerate nodes. Degeneracy occurs when there is collocation between two or more nodes of the same element. Those nodes share common degrees of freedom or, in this case, only the nodal value. Without degeneracy, the density of the nodes and elements could not collapse towards the origin.

Among the most likely candidates for alternative 8-node element shapes are irregular hexahedrons, concentric spherical shells, and proportional ellipsoidal shells. Irregular hexahedrons present the greatest challenge for coordinate mapping but afford the greatest flexibility in bounding and distributing the available data. Spherical and elliptical shells could potentially avoid the mapping issues but would suffer from poor bounding. Where a rectangular space is bounded by the six most extreme strains, a spherical space is bounded only by the point furthest from the origin. While an ellipsoidal space would be delimited by up to three points, its requisite symmetry would leave a lot of empty space with a data distribution like that shown in Figure 16. That distribution is principally a result of the lack of compressive testing, but

symmetric data in the longitudinal and lateral directions can never be guaranteed. Due to their flexibility, hexahedral elements then seem like the most promising option. Such an arrangement is overlaid on the existing data distribution in Figure 27. Shown are the faces of the elements that coincide with the base plane of each direction.

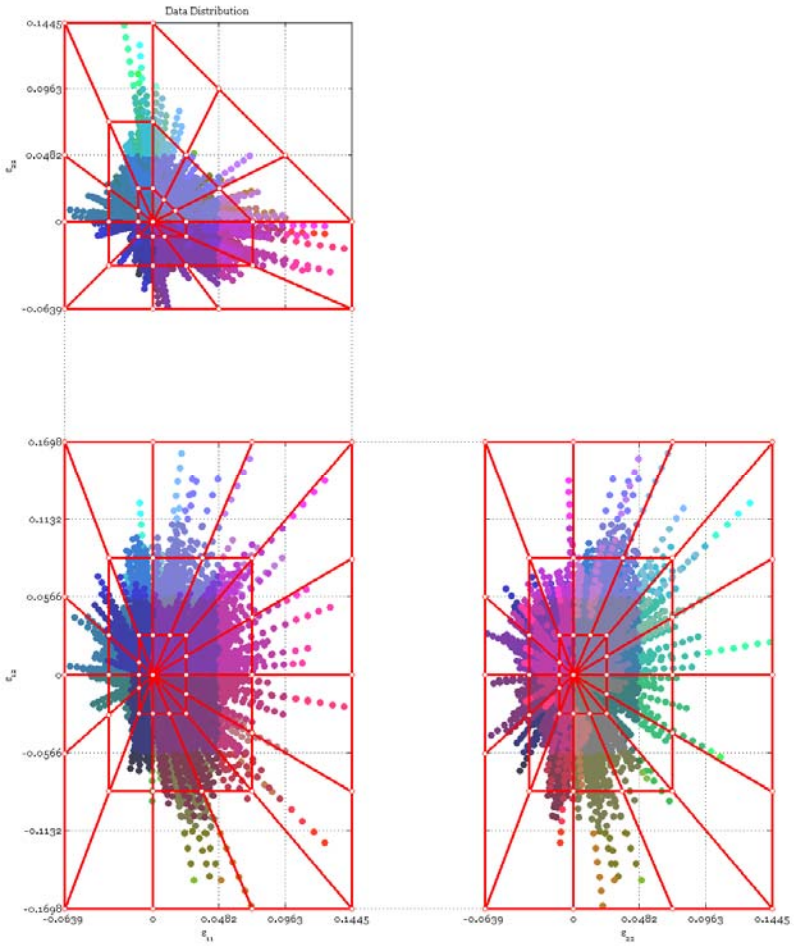

Figure 27. Possible Non-orthogonal Element Construction

The major drawback to an elemental arrangement that is not regularly distributed compounds one of the major drawbacks to an interpolating function of this nature in general. Even for a uniform distribution, the location and value

from every node must be transported and interpreted. As proposed, the association of the nodes with their respective elements would become obscure, so that information would also need to be conveyed. In a worst-case scenario, with m elements and p nodes, the eight nodes associated with each element would need to be enumerated along with the locations and values of each node for total of $4p+8m$ values that need to be transported. Regardless of the amount of additional information carried by these values, this number is ridiculous when compared to the parameters for any other damage criteria such as in equations (2-9). A standardized nodal distribution would likely need to be arranged before the DED function could be practical, reducing that number to approximately p.

Statistical Variation

Quantifying the statistical nature of the DED function itself is difficult because of the inverse nature of the problem. Specifically, dissipated energy density is extracted from total dissipated energy from an experiment. Comparisons can be made between experimental, optimized, and predicted total dissipated energy values, but not between DED since it is not measured as a direct quantity. The repeatability and expected variability of instances of the DED function are not immediately available. Theoretically, the deviation of a solution to the DED function from the true mean solution, if such a thing exists, would decrease as the number of included data points increased. However, this relationship is established primarily for response variables with directly

observable counterparts [24] and may be unclear for this type of deconvolution process.

To be consistent with the current paradigm in composite materials test data reporting, the DED function's statistical attributes would nonetheless need to be quantified. One way to accomplish this would be to divide the data into several solutions and use those to construct a single solution statistically. Where the individual solutions overlap, a mean solution could be calculated as could the variance at any point within the solution space. This would complicate the problem of weak data distribution and would likely narrow the boundaries of the final solution space. It may be the case that these effects could be minimized by allowing the separated data sets to be non-exclusive, but these interrelationships are beyond the scope of this thesis. It suffices to say that a candidate for measuring statistical properties of a DED-based function exists.

EMPERICAL CONSTITUTIVE RESPONSE

An alteration to the dissipated energy density inverse problem intended to focus on residual strength information was proposed by Eric Booth [26]. In this method, the DED interpolation function is replaced by several interpolation functions with identical domains whose functional values represent the desired constitutive properties of the material. For the purposes of modeling the in-plane response of a continuous fiber composite, those properties are the longitudinal, transverse, and shear moduli and possibly the Poisson's ratio. Each remains a function of the three in-plane strains.

$$\begin{aligned} E_1 &= E_1(\varepsilon_{11}, \varepsilon_{22}, \varepsilon_{12}) \\ E_2 &= E_2(\varepsilon_{11}, \varepsilon_{22}, \varepsilon_{12}) \\ G_{12} &= G_{12}(\varepsilon_{11}, \varepsilon_{22}, \varepsilon_{12}) \\ \nu_{12} &= \nu_{12}(\varepsilon_{11}, \varepsilon_{22}, \varepsilon_{12}) \end{aligned} \tag{45}$$

Again, the nodal values must be determined through deconvolution of experimental data. Since the linear response is a nontrivial component of the solution, total dissipated energy can no longer be used as the resultant of equations (28,31-33). In fact, the only scalar quantity that can be derived from the nonlinear properties and strains alone is the recoverable energy density defined by the elastic strain energy of a damaged element as in equation (35). This equation assumes that the material remains orthotropic with damage as can be seen by the stiffness tensor.

$$\psi(\vec{\varepsilon}) = \frac{1}{2}\begin{bmatrix}\varepsilon_1 & \varepsilon_2 & \varepsilon_{12}\end{bmatrix}\begin{bmatrix} \frac{E_1(\vec{\varepsilon})}{1-\nu_{12}(\vec{\varepsilon})\nu_{21}(\vec{\varepsilon})} & \frac{\nu_{12}(\vec{\varepsilon})E_2(\vec{\varepsilon})}{1-\nu_{12}(\vec{\varepsilon})\nu_{21}(\vec{\varepsilon})} & 0 \\ & \frac{E_2(\vec{\varepsilon})}{1-\nu_{12}(\vec{\varepsilon})\nu_{21}(\vec{\varepsilon})} & 0 \\ \textit{symm.} & & 4G_{12}(\vec{\varepsilon}) \end{bmatrix}\begin{Bmatrix}\varepsilon_1 \\ \varepsilon_2 \\ \varepsilon_{12}\end{Bmatrix} \quad (46)$$

Evident immediately are the nonlinear features of the components of the stiffness tensor due to the assumed variability of the Poisson's ratio. An equation of this kind cannot be solved using the procedure outlined in the previous chapter, so the first compromise that must be made is to assume that this value is constant. Because the off-axis Poisson's ratio ν_{21} is defined by the Poisson's ratio and the ratio of the stiffnesses, a provisional anisotropy ratio must also be assumed. The validity of both of these assumptions is not known. Having removed these variables, the recoverable energy density expands as follows.

$$\psi(\vec{\varepsilon}) = \frac{1}{2}\left(\frac{E_1(\vec{\varepsilon})}{1-\nu_{12}\nu_{21}}\varepsilon_1^2 + \frac{2\nu_{12}E_2(\vec{\varepsilon})}{1-\nu_{12}\nu_{21}}\varepsilon_1\varepsilon_2 + \frac{E_2(\vec{\varepsilon})}{1-\nu_{12}\nu_{21}}\varepsilon_2^2 + 4G_{12}(\vec{\varepsilon})\varepsilon_{12}^2\right) \quad (47)$$

Using the shape functions from equations (28) and (29) for each of the three unknowns, the total recoverable energy for a coupon is equated to the sum of the contributions to the recoverable energy from each element.

$$\Psi = \frac{1}{2}\sum_e A_e \sum_p t_p \sum_i \left[\frac{\varepsilon_1^2}{1-\nu_{12}\nu_{21}} \quad \frac{\varepsilon_2^2 + 2\nu_{12}\varepsilon_1\varepsilon_2}{1-\nu_{12}\nu_{21}} \quad 4\varepsilon_{12}^2\right]_{e,p}\begin{Bmatrix}\beta_{E_1} \\ \beta_{E_2} \\ \beta_{G_{12}}\end{Bmatrix}_i N_i(\vec{\varepsilon}_{e,p}) \quad (48)$$

The directional distinction between the unknown nodal values β_i is purely notational. In reality, the three directions merely construct a set of unknowns that is three times the size of any one space. Those unknowns are intrinsically linked and must be solved as a single set. Bounding this solution is relatively simple. The constitutive properties can never be negative nor can they ever exceed their original values assigned at the origin of each strain space. While simple, these bounds are not as robust or dynamic as those used in the DED function and, as seen there, adequate bounding is critical to a convergent and physically meaningful solution.

While a linear finite element model is as logically valid for calculating elemental strains for an interpolating empirical constitutive function as it is for an interpolating DED function, the idea that nonlinear modeling information that is being revealed is not then being reincorporated into the solution is slightly more offensive. A circular solution process of this kind would be vastly more complicated and resource exhaustive. Fortunately, it can be avoided entirely through the image correlation techniques already implemented.

The major drawbacks to an empirical constitutive response are akin to the pitfalls of its antecedent: the DED function. The insufficiency and poor distribution of data are entirely unaffected by the change as the strain spaces that make up the DED function and the components of this function are identical. In addition, while the strain spaces are constructed and populated identically, there are three times as many unknowns that must be represented by the same meager data set. That data set again has a finite boundary formed by the most extreme

strains found in the coupons. It is unlikely that those bounds could ever be inclusive of all strain vectors that might be encountered in a design situation even through computational test design such as that discussed by Furukawa[†] [27]. Those most extreme strain values continue to occur in the smallest elements of the coupon except, in this situation, high-valued strains ought to be associated with low residual strength. The lowest-weighted data points are then linked with the nodes with the highest relative residuals, further degrading the issue of misplaced elemental weight. Already poor transportability is also worsened by the inclusion of three times the number of nodal values. Ultimately, an empirical constitutive function would benefit from the same modifications as the DED function—primarily nonorthogonal elements with a standardized distribution.

In summary, this method would provide several engineering advantages over the DED function, but few practical ones. The ability to reproduce residual strength under any conditions would greatly increase the viability of an inverse solution, but many of the obstacles still inhibiting the success of an inverse solution are not mitigated by or are exacerbated by the increased complexity of the system.

[†] Furukawa suggests a distribution of tested load paths based on numerically defined quantities that characterize each path as informative, distinguishable, and unique. Interestingly, it is also implied that the coefficients of the stiffness matrix might be better suited for the design variables in this chapter.

ASSUMED NONLINEAR RESPONSE

Originally intended to augment the dissipated energy density function, finding a constitutive nonlinear material response began to dominate the direction of this work as it became apparent that such a response might accomplish the goals of the DED function without being subject to many of its shortcomings. Rather than attempting to create a heuristic function that is bound by—but not derived from—prior knowledge of the material behavior, a nonlinear response supplements the existing constitutive laws of the laminate. In doing so, it resolves at least two of the major drawbacks of the DED function. The numerous and scattered DED coefficients that are the root of the poor transportability are replaced by only a few additional material constants that represent the nonlinear response. Also, enhancing the elastic behavior rather than concealing it leaves a clearer picture of residual strength.

Simple Bilinear Response

On the most basic level, there are only two major events in the loading life of a sufficiently small element of material. The first is that the element will fail; that is, it will accrue initial damage and will no longer be considered as within the realm of elastic behavior. The second is that there will eventually be a load that obliterates the material so completely that it will no longer be able to carry any load at all. While the rate at which the events occur, the condition of the material between the events, and the ability to delineate the events with any certainty are

unclear, their existence is undeniable. The most basic way to approximate those two events is with a bilinear curve where the first half of the curve is the elastic response and the second half approximates the progressive damage of the material.

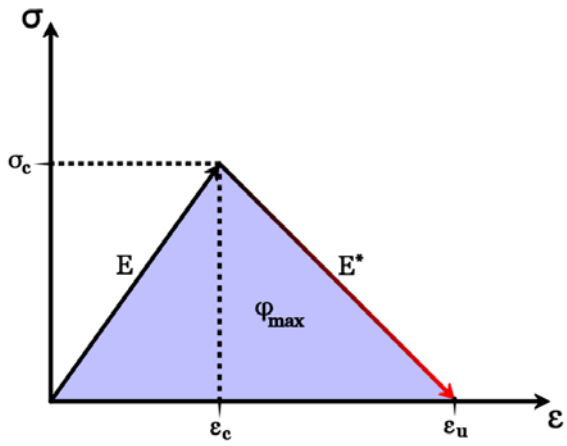

Figure 28. Representative Bilinear Constitutive Response

For a brittle orthotropic composite—when considering only in-plane loading—there must be such a curve for each of the three in-plane directions. By analogy, the two fundamental events have now become six: two for each of the three directions. Dissecting the response in such a way intrinsically uncouples the three directions leading to a failure envelope defined by maximum strain criteria when composites have been shown to be heavily affected by coupling such as in equations (4,6,9). While not trivial, the lack of direct coupling is not altogether damning. First, as mentioned above, a set of bilinear curves is the most basic expression of a post-damage response. It is therefore intended for it to set a lower bound for the quality of a model of this type. Increasing the number of parameters and the interaction between those and existing parameters can only

improve that quality. The problem with including directional coupling is that most existing multiaxial failure criteria do not distinguish between the modes of failure; this leads to ambiguity in which direction—or directions—the properties should be degraded.

Secondly, it is intuitive to expect that the strain used to predict damage initiation for a bilinear case will correspond with the classic strain to failure. While such a correlation would be convenient, it is not compulsory. The actual path between the point of initial failure and the point of ultimate failure is unknown and may contain confounding variables, so it is almost certainly nonlinear. Therefore, the line that serves as its best fit does not necessarily intersect the point of initial damage. A lack of direct coupling is then partially compensated for by indirect coupling through inclusion of multiaxial load paths in the determination of the best fit of the damage progression line.

In the same sense, interlaminar effects may also be absorbed by the optimization. Much of the damage tolerance of fiber reinforced plastics is a result of the distribution of the loads in weakened areas over other fibers and other plies. There could be both advantages and disadvantages to modeling this coupling with in-plane analysis alone. In its defense, reproduction of the coupling contributes to a more accurate representation of the material using a material model that is considerably less intricate than one that directly includes out-of-plane phenomena. However, packaging multiple modes of failure into one inherently removes any distinction between them so features which are unique to either will be blurred.

Optimization Parameters

Three points define the bilinear curve for each in-plane direction: the origin, the critical strain, and the ultimate strain. The ultimate strain must be positioned somewhere along the strain axis and the critical strain must be somewhere along the elastic line. This leads to a maximum of three parameters that must be found via optimization for each direction. Because the optimization of a set of n parameters has a computational complexity of, at best, $O(n^3)$, it is desirable to reduce the number of parameters by as much as possible. The model must be built for efficiency. Allowing the elastic constants to vary alongside the damage parameters would theoretically produce a better fit to the empirical data, but the practical benefits are marginal. Composites behave predictably within the elastic region and there is very little variation in the elastic constants due to multiaxial interaction; Hooke's law for orthotropic materials is already attentive to those interactions. Using predetermined elastic constants provides additional computational and practical advantages, as well. One of those advantages is the availability of that data prior to nonlinear analysis either from the manufacturer or via the methods discussed in Chapter 4. Other advantages are discussed throughout this chapter.

Secant Modulus

Optimization of the nonlinear properties is very similar to and uses the same ANSYS solvers as optimization of the linear properties which were discussed in Chapter 4. The difference between the two processes is primarily in

the model used to represent the material. There are several ways to execute a nonlinear material model but, in this case, a series of linear models was used. A model such as this requires understanding of the unloading behavior of the material. It has been presented several times in this thesis that, due to its brittle nature, a composite will unload linearly back to its undeformed configuration. Similarly, it is assumed that subsequent reloading will follow the same path until further damage ensues. This is what is known as a secant modulus. It is so named because it intersects the origin and the point of most severe loading. Since this secant line intersects the origin, a linear model is perfectly appropriate up until the updated critical point. Linear models are consecutively run until slightly beyond the point where damage occurs in any one of the elements, at which point the elastic modulus of that element is degraded and the critical point advanced according to the bilinear curve. This process is shown in Figure 29.

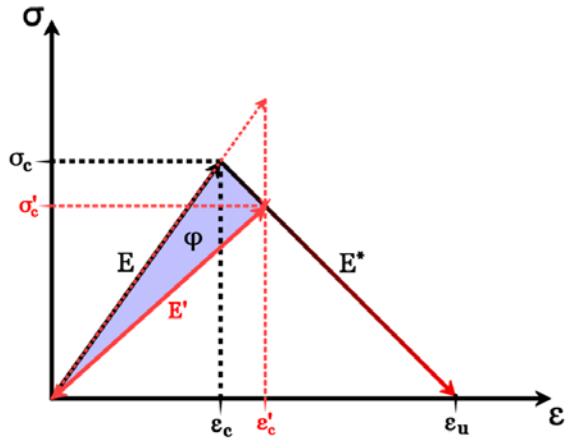

Figure 29. Secant Modulus (Overshoot Exaggerated)

Because the models are linear, each strain of each element is proportional to the boundary displacements. By this method, a set of three linear models can

be superposed using equation (34) to determine, precisely, the displacements for the next damage event. With any continuous constitutive response, however, initial damage is the only literal damage event. Even so, approximately half of every test is within the elastic range so that one linear combination eliminates nearly half of the displacement range where each element of the FEM would otherwise need to be assessed individually for damage.

A peripheral benefit to approaching the problem of nonlinearity with the secant modulus is that the information stored during damage expresses exactly the residual strength of the element. The reduced modulus and the postponed strain to failure acquired following a damage event are part and parcel of the concept of residual strength. In a design situation, those two values may be all that is required to permit or disallow the continuing operation of a component.

Modified Linear FEA Model

The ANSYS model used in Chapter 4 is well-suited to demonstrate the nonlinear constitutive response in every aspect but two. For one, each ply of each element is now susceptible to degradation of its properties, so each must be assigned its own material as defined by ANSYS. The three mutable critical strains must also be stored for each. Secondly, the model must be enclosed by an additional loop that controls the advancing displacement of the coupon. This loop differs only slightly and borrows largely from the loop that converges on individual displacement steps. Equation (23) is equally convergent for a shifting target displacement, although it will be seen that it is not unconditionally stable.

Displacement Step Size

Superposition is ideal for determining the point of initial damage but, because a bilinear response is inherently continuous, several options exist for the discretization of the subsequent points. For the purpose of comparison with the observed data, it is convenient if the sequence of displacements used in the finite element model is equivalent to that from the testing. It is also helpful in reducing the amount of interpolation that must be performed between displacement points as the linear paths suggested to the IPL cannot be strictly maintained. Coincident displacement points, however, are not required and reducing or increasing the number of points can decrease calculation time or improve accuracy, respectively.

Following the initial step, steps of a fixed size can be used. It is difficult to assign a definition to a fixed size in three dimensional boundary displacement space, especially when rotation is included. Rotation has fundamentally different units than displacement so it must be normalized as an arc length to be compared to the other components. A fixed step size can be interpreted as either a fixed path length interpolated between observed data points or as a fixed number of points generated between existing ones that are of roughly equal spacing. Reducing the step size refines the solution and, theoretically, successively improved solutions should asymptotically approach the continuous one. With IPL data, however, refined spacing does not necessarily generate a closer match because a coarse spacing creates more dramatic damage events where many elements are damaged simultaneously without the redistributive effects of refinement. This is not to say that such a prediction is a more accurate

representation of the model, only that damage events are also exaggerated by the compliance of the IPL. Changes in a predicted load-displacement curve due to alterations of the step size can be seen in the figure below.

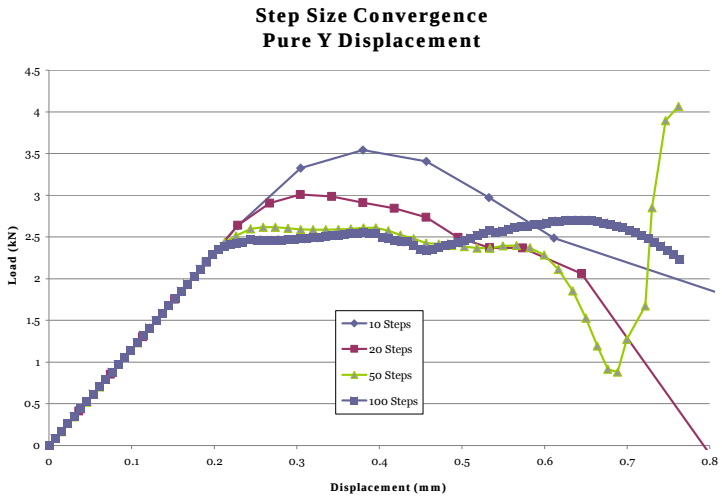

Figure 30. Convergence Due to Displacement Step Size

Several important characteristics can be seen in Figure 30. First, for the purpose of this convergence study, a fixed displacement size was used to demonstrate the value of determining the point of initial damage through superposition. Without it, the boundary of the damage envelope can vary by as much as a step size. Second, the rate at which the material initially degrades increases asymptotically as the size of the displacement step is reduced. This is not surprising since more frequent steps will more frequently degrade the material properties. In a third and related phenomenon, the loads and displacements of the 10, 20, and 50 step trials become unstable after about 0.6mm of displacement. Clearly, the reactions predicted are not feasible for the material model used but are instead an artifact of the boundary displacement

convergence algorithm used in the model. In the later steps, the fixed step size can be seen to be anything but. The boundary displacement algorithm uses proportional information from the previous step as a starting point for the current displacement, from which it uses the secant root finding method to converge on the target displacement. Changes to the overall compliance of the coupon ultimately disrupt the tractability of the displacement control and, as can happen with secant root finding, a poor initial condition leads to divergence. Smaller steps mitigate this problem by calling for approximations on a more local and therefore more accurate scale.

If refining the step size globally can improve detail during significant softening events and increasing the step size can improve performance, then combining those two methods should provide an optimal model. A model that implements an adaptive step size such as this decreases the step size only when sufficient damage is predicted or detected. The definition of “sufficient” is highly subjective for a continuous constitutive model but can be used as a parameter to vary refinement in a manner similar to a fixed step size: the difference being that resource once expended on uneventful steps are diverted to ones where a high degree of change is present. The metric used for this change is again a matter of choice but, for reasons mentioned throughout this thesis, dissipated energy seems like the most direct analog to damage. In order to determine whether this threshold has been met, a large tentative step is made at which point the change in dissipated energy is calculated. If the change in dissipated energy exceeds the tolerance parameter, then the step size is refined and the model reverts to its

state prior to the anticipatory step. For efficiency purposes, the full step is refined only as far as a specified minimum substep, even though convergence is guaranteed at any resolution for a continuous model. The next full step proceeds in a similar manner. Due to the nontrivial amount of backtracking, an adaptive solution can increase the computation time compared to a fixed step solution with a comparable number of final points by as much as 50%. In practice, the marginal improvements in detail were overshadowed by inconsistency in the test data; in addition, a decisive variable based on dissipated energy that was consistent between load paths proved elusive, so the adaptive step size was abandoned for efficiency.

Objective Function

Unlike the optimization of the linear properties and deconvolution of the DED function, there is no clear metric for quantification of the quality of a nonlinear constitutive response. Part of the confusion lies in the multitude of data sources that arose in the search for a satisfying DED function. There is also a balance within each option between an acceptable end result and suitability as a residual for optimization.

Load-Displacement

The most viscerally gratifying match for the modeled data would be the load-displacement data that comes directly from the IPL. Prediction of residual strength is the most telling result but also the most difficult to obtain. Ideally, the

residual used for the objective function of the optimization would be the difference between the predicted loads and the unprocessed actual loads, but there are reasons why that might not be the most realistic metric.

In calculating the loads applied to the coupon, the IPL must translate the information gathered from the load cells based on displacement data from one of a few sources: the actuators, the LVDT array, or the image correlation. None of these sources have the capability to include deformation in the IPL frame pieces, so the exact alignment of the load cells is not known. This problem increases proportionally with the load and often leads to unexpected results in the load-displacement curves, especially in the rotation direction which appears to be most sensitive and most erratic.

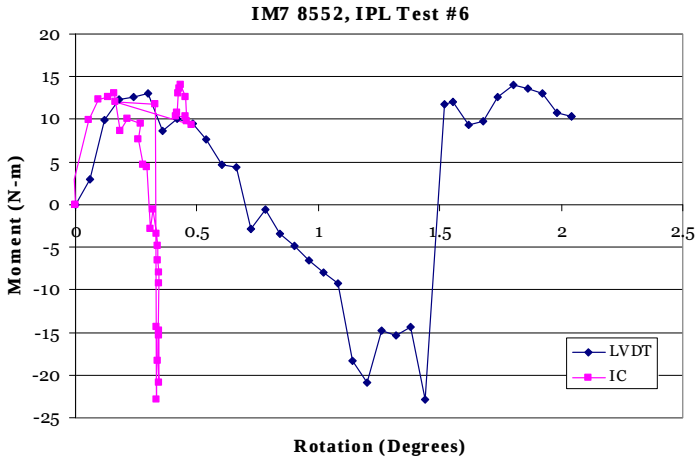

Figure 31. Erratic Rotation Data

Furthermore, the elastic data are never entirely congruent with the gathered or optimized elastic constants. The elastic constants are, of course, the best fit to the available data, but that does not guarantee that every stiffness is aligned. An offset of this kind causes two problems. First, the differing initial

stiffness between the two curves creates an irremovable component of the residual that can decrease the sensitivity of the optimization. Second, if the elastic components do not coincide, then neither can the points of initial failure. This mismatch will cascade through the remainder of the degraded portion of the test. In the best case, what will develop is failure controlled by load rather than displacement which runs contrariwise to the proposed strain-induced damage model. There is also a possibly vast difference in the damage energy with this objective function. In Figure 32, the shaded area represents both the indelible component of the objective function and the approximate difference in dissipated energy between the observed data and the load-displacement optimized model.

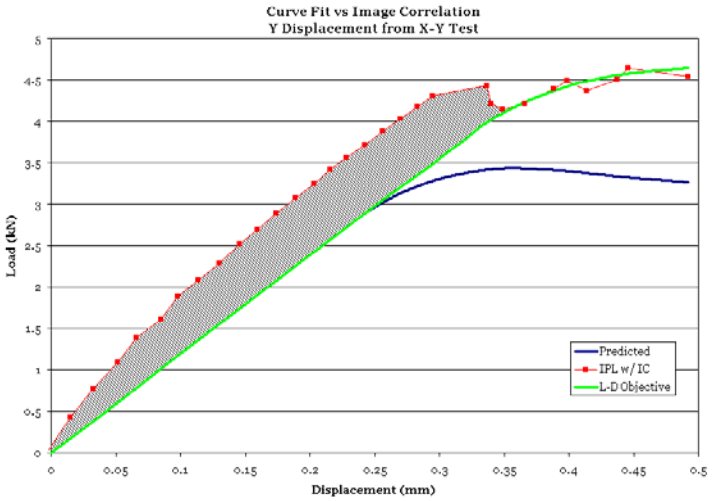

Figure 32. Mismatched Elastic Constants

Dissipated Energy

Inconsistency in the IPL load-displacement data and imperfect elastic properties can both be compensated for by using a residual based on total dissipated energy. Since there is no dissipated energy associated with an elastic

response, that portion of the curve provides no contribution to the residual. Dissipated energy can also be determined by the IPL without first converting the load cell data to coupon boundary data. As dissipated energy is a direct measure of the degree of damage of the material, it seems more appropriate to minimize the difference between the DE of the model and the tests when a discrepancy between the actual data is unavoidable.

The primary disadvantage to using dissipated energy as the objective function is the loss of information. Only one DE curve exists for a set of up to three load curves, so unrecoverable information is inevitable. The suppression of the elastic region—which was beneficial to other ends—removes the possibility of including the elastic parameters in the bilinear fit. While there are practical reasons why they might not be included anyway, the option is no longer feasible. Elastic properties must be known if this metric is to be used.

Full-Field Strains

Image correlation has provided detailed information about the microscopic behavior of each coupon. For the DED function, that microscopic behavior can theoretically be used in aggregate to derive the macroscopic behavior. There are then reasons to suspect that full-field strains could provide similar enhancements to the optimization of a nonlinear constitutive response. After all, the bilinear function uses the accumulation of microscopic damage via finite element analysis to predict the macroscopic behavior of the material. It

would seem, then, that direct comparison of the microscopic elements could provide an even more precise solution.

The problem with this approach is that it removes any statistical advantage. For the sum of the dissipated energies of the coupon elements to match the total dissipated energy of the coupon, the dissipated energy density must only be accurate on average. To compare the element strains from the finite element analysis to those from the image correlation, the strains must be accurate exactly. From a practical point of view, it is a problem of repeatability. Where a finite element model will always identically reproduce the same result, actual coupons will have variations due to irremovable flaws that lead to dramatic changes on the microscopic level but only minor changes on the macroscopic level. These microscopic changes are evident in the difference between two otherwise identical tension tests seen in the figure below.

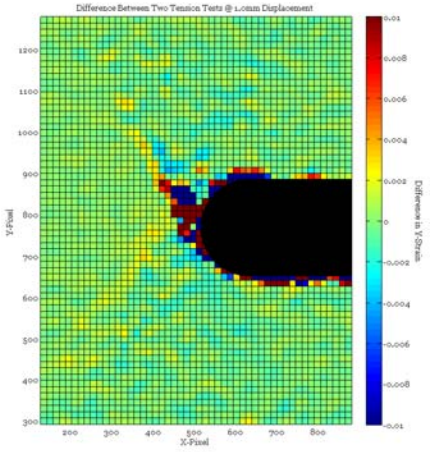

Figure 33. Strain Difference between Tests

By definition, composites are not homogenous so modeling them with homogeneity is inherently less valid as the scale decreases. This is not the only

source of inconsistency with the IC strain data, however. Perfectly repeatable alignment of the coupons within the IPL grips is not possible, and calculation of the strains near the edges of the coupon is intrinsically less accurate than at interior points due to round off error in the finite difference approximations. By design, damage originates at the edge of the notch so the strains calculated in what are arguably the most crucial areas are arguably the least reliable. In addition, cracking tends to dislodge the speckle paint by which the coupon is tracked. Eventually, this renders tracking impossible in damaged areas.

Initial Conditions and State Variables

While reasons have been discussed as to why the critical points in the bilinear curves might not correspond with the classic strains to failure, there are no better initial guesses for these unknowns than those values. For the IM7 8552 carbon fiber pre-preg, the published strain to failure is 1.56% in the fiber direction and 0.9% in the transverse direction [20]. These strains were calculated by dividing the longitudinal and transverse strength by the respective modulus. Similarly, the initial guess for shear strain to failure was 1.77%.

Guesses for the ultimate strains are far more speculative. These quantities are entirely nonphysical in the context of traditional testing so no precedent exists. Primarily, this is resolved through intuition and wide bounding. In the fiber direction, it is reasonable to project the brittle mechanism of fiber rupture onto a mathematical model that exhibits very rapid degradation following initial failure. Since the entire laminate is largely dominated by the fiber direction

modulus, this would also be conducive to explaining sudden damage events. Conjecturing about the ultimate strains in the transverse and shear directions is more complicated as a result of the comparably influential modes of failure there. However, matrix failures are generally borne from crack growth and, since they are typically not thought of as critical, that crack growth is stable. This indicates that a prolonged damage progression should be expected under a continuous model. Again, liberal constraints on the design variables alleviate much of the concern over well-posed initial conditions and, even then, design variables confined by constraints that are too strict will be observed as being pinned against the encumbering constraint.

Critical to the feasibility of this optimization are the relative positions of ε_c and ε_u. It is physically meaningless for the ultimate strain to occur prior to the critical strain, and indeed such a situation could be devastating to the stability of the model. Those two design variables are free to roam within their constraints in the optimization, but providing them with mutually exclusive constraints could bias their absolute positions. Therefore, a state variable s must be deployed in each direction to remove the possibility of overlap.

$$s_i = \varepsilon_{u,i} - \varepsilon_{c,i} > 0 \tag{49}$$

Optimized Results

Convergence of the six strain variables is akin to the convergence of the elastic constants. The random generation of design sets and assumed quadratic

shape of the design space using the SAM method produce little noticeable variation in convergent paths. Because it is nearly identical to Figure 14, a plot of the final convergence of the critical and ultimate strains is not shown here. Shown below are three of the seven load paths used in this optimization comparing the observed and predicted dissipated energy curves as well as the same comparison for associated load-displacement curves. The remaining four paths have been relegated to Appendix A.

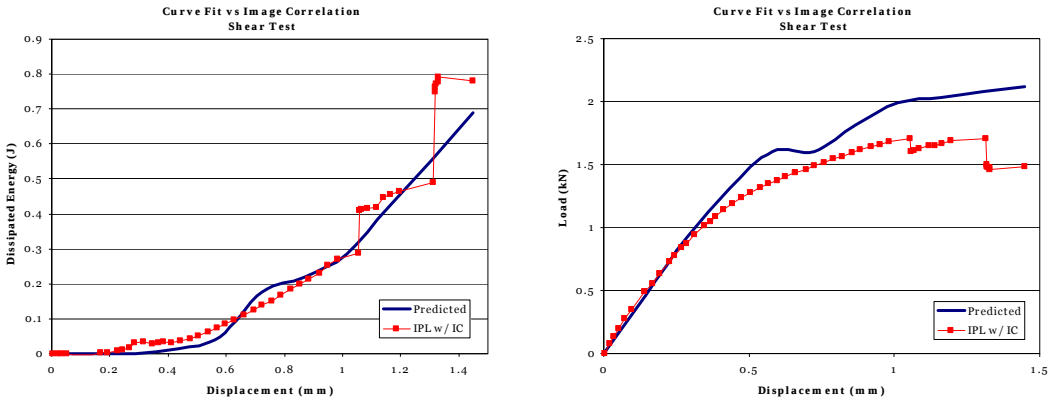

Figure 34. Nonlinear Results for Shear Test

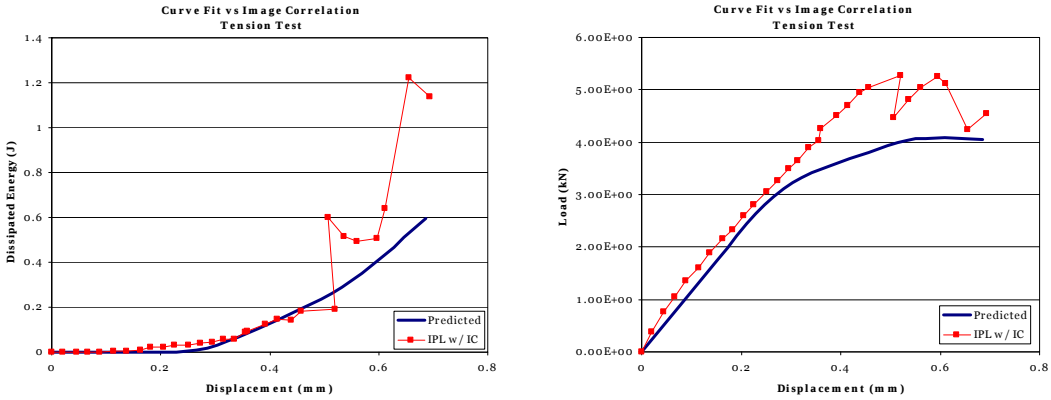

Figure 35. Nonlinear Results for Tension Test

In Figure 34 and Figure 35 can be seen several noteworthy characteristics of the bilinear response and the optimization. When compared to the IPL data, all of the curves from the modeled response are very smooth. How much of this discrepancy that is a result of the inability of the model to capture damage events is not clear. As mentioned throughout this thesis, the compliance of the IPL tends to exaggerate damage events. However, due to instability instigated in the model from a steeply degrading longitudinal modulus, the bounds of the ultimate strain in that direction may have been too stringent to accurately predict such events. A solution to this issue has not yet been found. However, it is likely that full recreation of damage events will involve changes to both the model and the IPL, which will be discussed later.

Also demonstrated in these figures is that the best fit to each DE curve must often be sacrificed in order to produce the best fit for the entire set of tests. If Figure 34 and Figure 35 were the only two tests included in the objection function, the fit to each would likely be much more satisfying, although the fit to the actual material would be far worse. Complicating this issue is the fact that as more intricate loading configurations are attempted with the IPL, less predictability can be expected from the results. Figure 36, representing a combination of tensile and shear loading, demonstrates this to a lesser degree than seen in the remaining four tests in the appendix. Paradoxically, the shear load is predicted to stiffen as heavy damage occurs in the tensile direction where the opposite is true in the observed results. This behavior is explicitly impossible with a purely linear finite element model (remembering that the nonlinear

material model is implemented as a series of degrading linear ones). The explanation for this incongruity is in the application of the boundary conditions. With tabs, a prescribed coupon displacement will generally require a combination of all three tab displacements. In this case, the desired displacements induced an above average tab rotation such that portions of the model deviated enough from the small angle approximation as to be noticeable. This could likely be remedied by allowing geometric nonlinearity. It is noted, however, that as damage occurs, the sample has softened as a whole, as required by thermodynamic constraints. That is, overall stiffening behavior cannot occur when energy is dissipated as a result of damage formation.

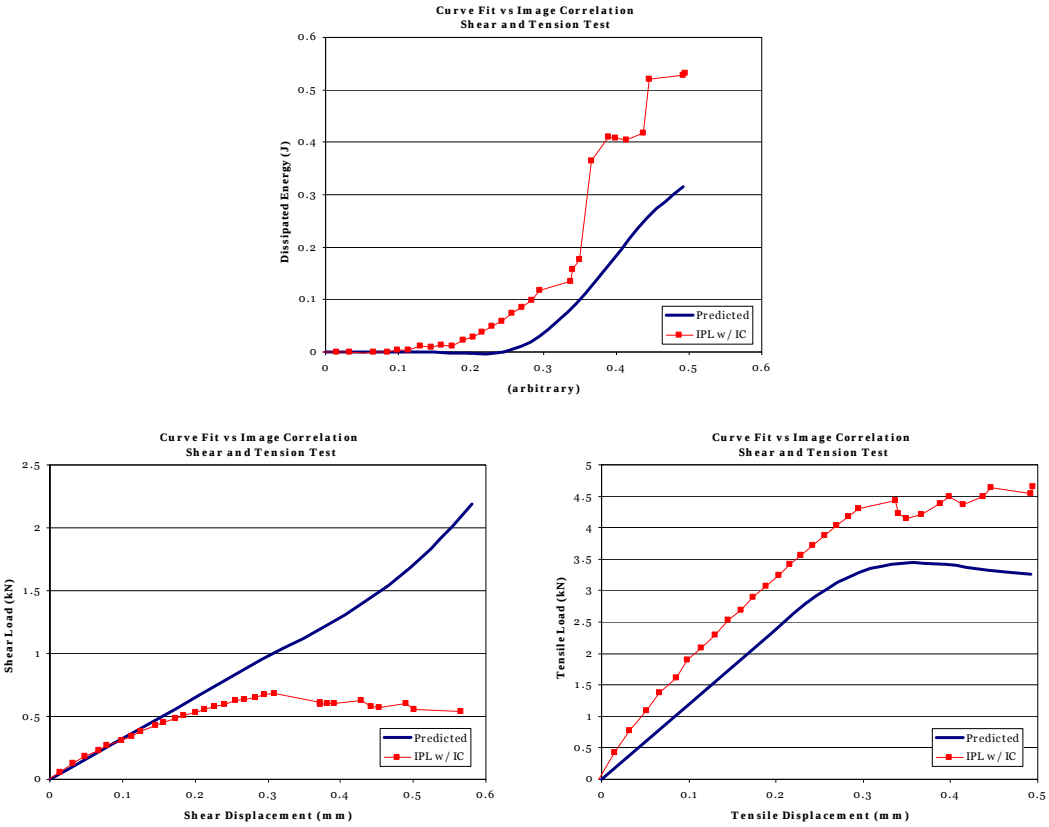

Figure 36. Nonlinear Results for Shear and Tension Test

The converged results for the six design strains can be seen in Table 4. While it has been explained that there are no existing values to which these can be reasonably compared, the longitudinal and transverse critical strains are strikingly near their classical counterparts mentioned earlier. It is very possible that this is a coincidence. Again, it is worth noting that the stability of the model was compromised when using values for the longitudinal ultimate strain that induced a steeper degradation than that shown. It is therefore possible that this strain and, consequently, the other strains could change substantially to improve the fit with a more stable model. As expected, the transverse and shear failure components of the model are protracted when compared to the fiber direction.

Table 4. Optimized Critical and Ultimate Strains

	ε_c	ε_u
Longitudinal	1.46%	2.55%
Transverse	0.91%	3.14%
Shear	0.94%	4.02%

Future Work

It is probably safe to say that the preceding results are at the boundary of what can be learned from the bilinear model that was intended as proof-of-concept. Several tasks remain, however. First, the model established will need to be verified. Second, a model based on damage initiation criteria that have a stronger correlation to experimental observations will need to be developed.

Finally, the equipment used to test the materials will need to be tailored to better suit the analysis.

Platform, Geometry, and Ply Independence

The entirety of this analysis was performed using ANSYS. While it is unlikely that any significant differences exist between the underlying methodologies of finite element modeling platforms, there is reason to be cautious about the translation of the bilinear algorithm. Once this translation has occurred, coupons with geometries differing from that of the standard IPL coupon should be tested and analyzed. Open hole compression and bearing tension tests were used to test the DED function, but those tests were poorly suited for that analysis due to the deliberate omission of compression data. A similar hazard exists for any database acquired through the testing of thin IPL coupons, including this nonlinear model. Regardless, some means of verifying that the optimized nonlinear properties are equally valid for any geometry will need to be found.

Since it is possible that layup-specific interlaminar interactions have been partially absorbed by the bilinear model, testing of other layups of the same material against the model will demonstrate the degree to which that interaction has been captured. The models presented in this thesis are intended to, and have their greatest utility when they can, be applied irrespective of—or with only minimal considerations for—layup. In the worst case, testing of other laminates will provide a threshold after which a new database must be created.

Alternative Material Models

Several alternatives to the simple bilinear model have been proposed and are in various stages of development. Fundamentally, only thee alterations can be adopted in the attempt to improve upon the basic model. The first modification is to allow a more detailed damage progression by increasing the number of parameters in the curve fit or by changing the polynomial order of the piecewise functions that makeup the general nonlinear curve. These changes alone are characterized by swiftly diminishing returns since added detail is often eclipsed by experimental uncertainty. The second modification available depends largely on qualitative observation of continuous fiber composites. In this case, discontinuous changes are applied to the material model based on an element's first ply failure. For instance, Chang's property degradation model proposes a modified stiffness tensor based on the first mode of failure encountered [28]. The Wen-Lin model is derived from the Chang model to suggest that transverse stiffness is maintained through matrix failure. "Due to interlock action with the neighboring plies, the damaged ply gradually loses its capability to support transverse stress until the fracture in shear or the breakage or buckling in the fiber on the same ply" [28].

Table 5. Stiffness Tensor Degradation Models

Failure Mode	Chang	Wen-Lin
Matrix Tension or Compression	$\begin{bmatrix} C_{11} & 0 & 0 \\ 0 & 0 & 0 \\ 0 & 0 & C_{66} \end{bmatrix}$	$\begin{bmatrix} C_{11} & 0 & 0 \\ 0 & C_{22} & 0 \\ 0 & 0 & C_{66} \end{bmatrix}$
Fiber Breakage or Buckling	$\begin{bmatrix} 0 & 0 & 0 \\ 0 & 0 & 0 \\ 0 & 0 & 0 \end{bmatrix}$	$\begin{bmatrix} 0 & 0 & 0 \\ 0 & 0 & 0 \\ 0 & 0 & 0 \end{bmatrix}$
Fiber-Matrix Shearing	$\begin{bmatrix} C_{11} & 0 & 0 \\ 0 & C_{22} & 0 \\ 0 & 0 & 0 \end{bmatrix}$	$\begin{bmatrix} C_{11} & 0 & 0 \\ 0 & 0 & 0 \\ 0 & 0 & 0 \end{bmatrix}$

In the Wen-Lin model, first ply failure is predicted using a reduced Tsai-Wu tensor criterion similar to equation (6) which begs the question of how the mode of failure is determined. The answer to this question leads to the third general modification that can be used to improve the basic nonlinear response: failure contribution factors. These factors attempt to quantify the effect that each available failure mechanism has had towards the overall failure of the element. For the Wen-Lin model, the reduced Tsai-Wu equation is broken down into the contributions from each component of stress.

$$\begin{aligned} d_1 &= F_1\sigma_1 + F_{11}\sigma_1^2 \\ d_2 &= F_2\sigma_2 + F_{22}\sigma_2^2 \\ d_{12} &= F_{66}\tau_{12}^2 \end{aligned} \tag{50}$$

These factors do not necessarily lose their significance following initial failure but, in the Wen-Lin model, they are then abandoned and the remaining coefficients of the stiffness tensor are calculated based on softening of the elastic constants. The fiber direction is affected by an initial softening followed by a brittle fracture; the transverse modulus also encounters an initial softening but terminates in a gradual degradation; and, as can be seen in Figure 37, the shear direction adheres to a quadratic path that ends in another brittle fracture. If this shear response was used prior to initial failure, then it would be nonlinear elastic and modeling it with the secant modulus technique would not be possible. However, these paths are not enforced until after the stiffness tensor has been degraded following first ply failure and could therefore all make use of the secant modulus.

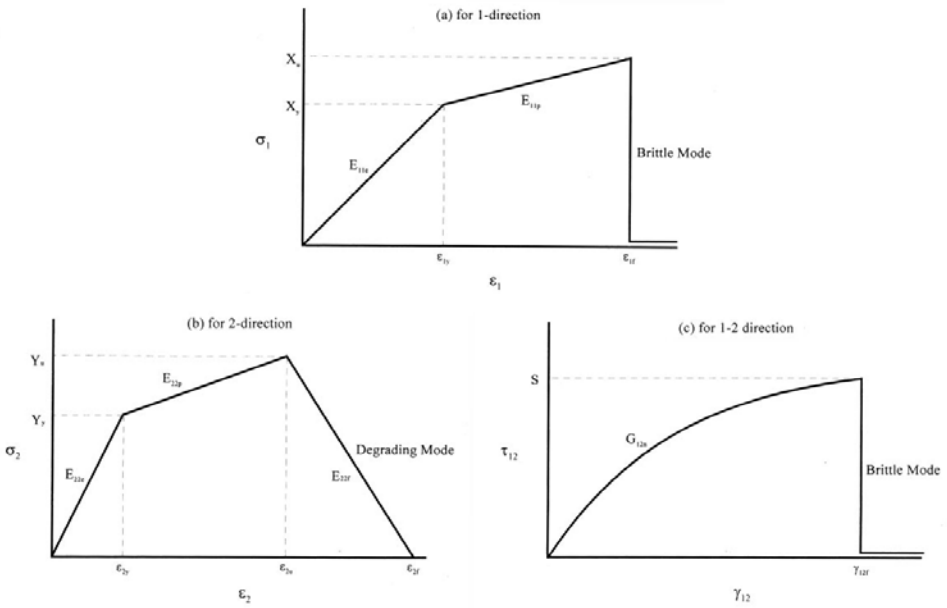

Figure 37. Multi-Stage Failure Modes [28]

As an aside, testing for this model made use of several layups including $[\theta/(90-\theta)]_s$, $[\pm\theta]_s$, and $[(\theta)_3/(\theta+45)/(\theta-45)]_s$ where the base angle θ was varied between 0° and 90°. While some of those coupons can be manufactured by cutting one laminate at appropriate angles, others require preparation for each individual angle. This approach to testing may be in opposition to the quick and inexpensive test methodology defended in this thesis.

Where the Wen-Lin model employs all three possible modifications to the basic nonlinear response, other methods attempt to forge a balance between complexity and reliability. In the ABAQUS finite element modeling program, for example, a bilinear approach is taken but coupling between directions is enabled through three failure contribution factors, referred to by ABAQUS as damage variables. "To alleviate mesh dependency during material softening, ABAQUS introduces a characteristic length into the formulation… L^c is computed as a square root of the integration point area" [29]. The characteristic length is used as the basis for the equivalent displacements of each element that are, in turn, used to formulate the damage variables. Since the Hashin model is used to predict initial failure, the equivalent displacements are separated according to that model into fiber and matrix tension and compression. These equations make use of the Macaulay bracket operator to account for the sign of the strain.

$$\langle \varepsilon \rangle = \frac{\varepsilon + |\varepsilon|}{2} = \begin{cases} 0 & if \quad \varepsilon < 0 \\ \varepsilon & if \quad \varepsilon \geq 0 \end{cases} \tag{51}$$

$$\delta_{eq}^{ft} = L^c \sqrt{\langle \varepsilon_1 \rangle^2 + \alpha \varepsilon_{12}^2} \qquad \delta_{eq}^{fc} = L^c \langle -\varepsilon_1 \rangle$$
$$\delta_{eq}^{mt} = L^c \sqrt{\langle \varepsilon_2 \rangle^2 + \varepsilon_{12}^2} \qquad \delta_{eq}^{mc} = L^c \sqrt{\langle -\varepsilon_2 \rangle^2 + \varepsilon_{12}^2} \tag{52}$$

Each equivalent displacement is then used to calculate the damage variable for the four failure modes. A piecewise function describes this dependence. The equivalent displacements that correspond to initial and complete damage in a particular mode are evident in Figure 38.

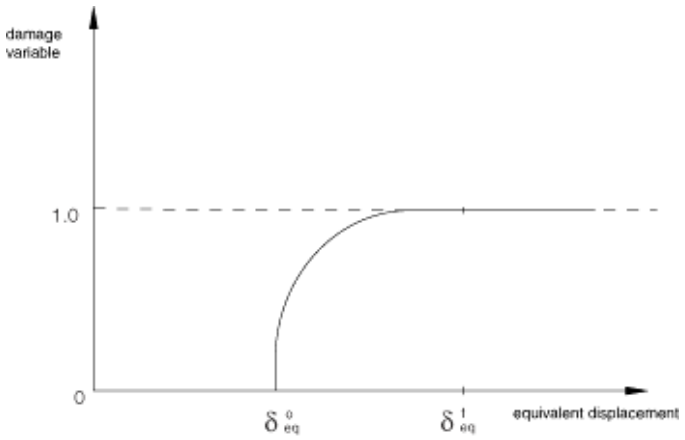

Figure 38. Damage Variable Evolution [29]

$$d = \begin{cases} 0 & if \quad \delta_{eq} < \delta_{eq}^0 \\ \dfrac{\delta_{eq}^f \left(\delta_{eq} - \delta_{eq}^0 \right)}{\delta_{eq} \left(\delta_{eq}^f - \delta_{eq}^0 \right)} & if \quad \delta_{eq}^0 \le \delta_{eq} < \delta_{eq}^f \\ 1 & if \quad \delta_{eq} \ge \delta_{eq}^f \end{cases} \tag{53}$$

After the damage variables for the four modes of failure have been found, they are reduced to three that represent the three in-plane directions. The damage variables in the fiber and matrix directions are chosen based on the sign

of the effective stress. Conversely, without more direct information, the damage variable in shear is a function of the damage variables from all four modes.

$$\begin{Bmatrix} \hat{\sigma}_1 \\ \hat{\sigma}_2 \\ \hat{\tau}_{12} \end{Bmatrix} = \begin{bmatrix} \frac{1}{1-d_f} & 0 & 0 \\ 0 & \frac{1}{1-d_m} & 0 \\ 0 & 0 & \frac{1}{1-d_s} \end{bmatrix} \begin{Bmatrix} \sigma_1 \\ \sigma_2 \\ \tau_{12} \end{Bmatrix} \tag{54}$$

$$d_f = \begin{cases} d_f^t & if \quad \hat{\sigma}_1 \geq 0 \\ d_f^c & if \quad \hat{\sigma}_1 < 0 \end{cases}$$

$$d_m = \begin{cases} d_m^t & if \quad \hat{\sigma}_2 \geq 0 \\ d_m^c & if \quad \hat{\sigma}_2 < 0 \end{cases} \tag{55}$$

$$d_s = 1-\left(1-d_f^t\right)\left(1-d_f^c\right)\left(1-d_m^t\right)\left(1-d_m^c\right)$$

Damage is applied to the elastic constants and a damaged stiffness tensor is assembled based on those properties as in equation (56).

$$C_d = \frac{1}{D}\begin{bmatrix} \left(1-d_f\right)E_1 & \left(1-d_f\right)\left(1-d_m\right)\nu_{12}E_2 & 0 \\ & \left(1-d_m\right)E_2 & 0 \\ symm. & & \left(1-d_S\right)G_{12}D \end{bmatrix}$$

$$D = 1-\left(1-d_f\right)\left(1-d_m\right)\nu_{12}\nu_{21} \tag{56}$$

Failure in this method is bilinear with respect to equivalent stress—which has an analog to the Hashin model similar to equation (52) that is not shown here—and equivalent displacement in each direction. This will only guarantee observed bilinear behavior under uniaxial loading which is to be expected when

coupling between directions is included. While the equivalent displacement for initial damage is input by the user, the equivalent displacement at which complete damage is assumed for a particular failure mode results from a value provided by the user for the maximum energy that can be dissipated in that mode. The maximum dissipated energy G^c is shown in Figure 39. This figure also demonstrates that, as has been done in this work, unloading and reloading occur along a linear path to the origin.

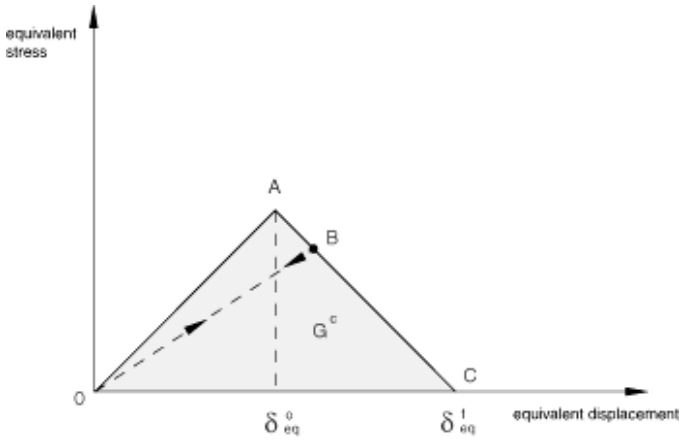

Figure 39. Equivalent Bilinear Response [29]

While seemingly very complicated, the damaged stiffness tensor used by ABAQUS does not directly depend on its inclusion of the Hashin damage criteria and could be readily adapted to any model where three failure contribution factors can be identified. The modified Tsai-Wu factors from equation (50) are one such an example. Due to its flexibility, equation (56) is a likely candidate for any future work on this topic. In fact, during this research, a switch to ABAQUS was considered but initial trials revealed that coupon tests with a comparable

level of detail consumed more time than was reasonable for optimization. A more plausible approach would be to modify the existing ANSYS code.

Modifications to the IPL

Currently, motion of the IPL is performed in steps. The desired load path is divided evenly into a predefined number of steps which are converged upon in a manner mimicked by the finite element model. This involves further division of the substeps but, ultimately, measurements are only collected at the step level. For the majority of the load path, this approach is perfectly adequate. However, the most critical parts of the data for post-damage analysis are the damage events. Using discrete steps, only the aftermath of such events can be observed. The events can be further obscured by controlled reversal of jumps in displacement from the release of frame strain energy. Backtracking is only apparent in the difference between displacements found through image correlation and those output by the IPL; this can be seen in Figure 40.

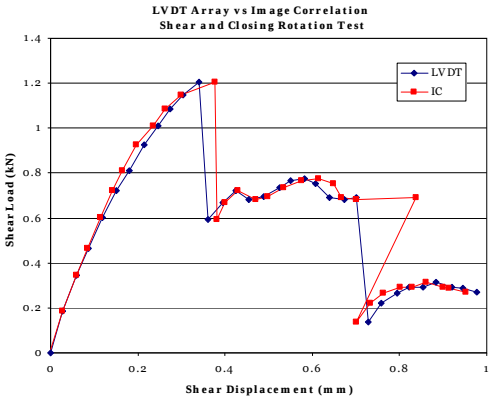

Figure 40. IPL Backtracking

Ideally, the IPL would be rebuilt or modified to increase the stiffness of the frame to minimize its capacity to store energy, but an interim solution could be to modify its control system to make data acquisition as continuous as possible. Rather than strictly adhering to discrete points on a load path that—because of discontinuous damage events—can never be identically reproduced, a continuously updating awareness of the displacement state could be combined with a continuously updating target displacement. It has been seen that none of the material characterization techniques in this thesis require specific load paths as long as a number of diverse load paths can be accurately surveyed.

The techniques required for this task have already been established. Equation (23) successfully achieves convergence for the boundary conditions of the tabbed finite element model with a shifting target displacement. In the case of continuous data acquisition, the target displacement is a portion of the full displacement based on the fraction of elapsed time. Equation (57) also lends itself readily to finding the rate of displacement.

$$\vec{u}_{act}^{\,j+1} = \vec{u}_{act}^{\,j} - \left(\vec{u}_{lvdt}^{\,j} - \frac{t_{j+1}}{t_n} \vec{u}_{total} \right) \tag{57}$$

$$\frac{\partial \vec{u}_{act}}{\partial t} \approx \frac{\vec{u}_{act}^{\,j+1} - \vec{u}_{act}^{\,j}}{t_{j+1} - t_j} \tag{58}$$

With the current control system, the rate of extension of each actuator is set as a constant. Consequently, actuators with a shorter distance to travel require less time to arrive, so the displacement between steps is inherently

nonlinear. While this may be reason enough to include velocity control, velocities would be considerably more important in a system that approximates continuity. Fortunately, the vector loop kinematic equations can be used to determine appropriate actuator speeds with accuracy sufficient for minute changes in displacement. Broader assignment of velocity is inadvisable due to large rotations in the actuators. With small angle approximations, equation (11) can be differentiated with respect to time to provide the necessary rate of change of length for each actuator.

CONCLUSIONS

One of the primary results of this work has been the demonstration of the versatility of multiaxial testing. With only a handful of tests and only one coupon geometry, multiaxial test data were used to predict elastic constants, an irregular damage initiation surface, and damage evolution for orthotropic materials. While still in development, the IPL has certainly been a prolific engineering tool. Its fruit is no less promising.

Determination of orthotropic constants becomes an almost trivial part of the full spectrum of the composite response. Since damage cannot be observed without first traversing through the linear region, those data are a subset of any post-damage database. With a refined process, the optimization of those constants is relatively straightforward.

The DED Function also has considerable potential—primarily as a metric of damage initiation. Were the modifications suggested in Chapter 5 implemented, a very detailed picture of the interactions between strain directions could emerge that is independent of all presupposed shapes. For any real-world application, however, extracting a constitutive response from the DED function is practically impossible. This task should therefore be left to nonlinear analysis.

The only true impediment to a nonlinear constitutive response is the disconnect between damage events in the test data and damage events in the model. This problem needs to be approached from the two directions that are its two major contributors. Undeniably, there are behaviors measured in the IPL

data that do not belong exclusively to the coupon. Image correlation has been enormously helpful to the end of acquiring viable data from the IPL but, as is the case for all testing machines, all variables but the coupon response must be minimized. Secondly, although damage events are exaggerated by the IPL, they are certainly present. The hindrance to recreating these damage events in the nonlinear model needs to be isolated and corrected. These two methods will work in opposite directions until they converge to an adequate correlation between prediction and observation.

As regards all of the above techniques, it is clear that a database ignorant of compression data is insufficient in nearly all practical cases. This is a conundrum when it comes to the continuing use of the IPL. The thin coupon was used because the maximum design load of the machine is approximately 25 kN—a load that would nearly be exceeded by a coupon only twice as thick. Reducing the gage length could also alleviate this problem, but doing so could potentially introduce three dimensional gripping effects into the notched area. The solution could be as simple as using other testing devices for the compression coupons, although this would not agree with the minimalist testing approach. One way or another, this issue needs to be addressed in the future.

Application to Composite Structures

Following verification at the coupon level, the nonlinear material model would be applied practically in a manner very similar to damage tolerant design. In addition to regular inspection intervals, however, it is likely that a

comprehensive post-damage-conscious design would include in situ load sensing devices. The reason for this is the difference in the cause of damage between the two design philosophies. In damage tolerant design, stable crack growth is assumed based on anticipated cyclic loading. With a nonlinear constitutive response or with the DED function, damage occurs during overload events.

With the DED function, the first step will be to determine whether any of the loads measured during the overload event exceeded the damage initiation envelope. Finite element modeling of the structure subjected to the observed loads can provide an indicator of where and to what severity damage has occurred when compared to the DED database. If this information is not sufficient—that is, if residual strength information is required—a nonlinear model should be employed; the DED function has the potential to provide a map of where inspection for damage should occur, but its utility towards the question of continued operation is minimal.

Sensors that are mounted on the surface of and embedded in composite laminates are currently under research at Montana State University. Their impact on the overall strength of components and the efficacy of their measurements are the focus of that research. For large, non-monolithic structures, the number of sensors required would be small since they could merely be aligned the component's primary loading directions. The information gathered at these points could be used to infer the deformation of the entire component using finite element analysis with a nonlinear model. That model would then predict several things: where damage has occurred, the degree to which damage has occurred,

the residual strength of the elements of the model and, by extension, the residual strength of the component. If that strength is adequate for normal operation with allowances for the possibility of subsequent overload events, then the component could remain in service. Otherwise, it would need to be repaired or replaced. A diagram of this process is shown in Figure 41.

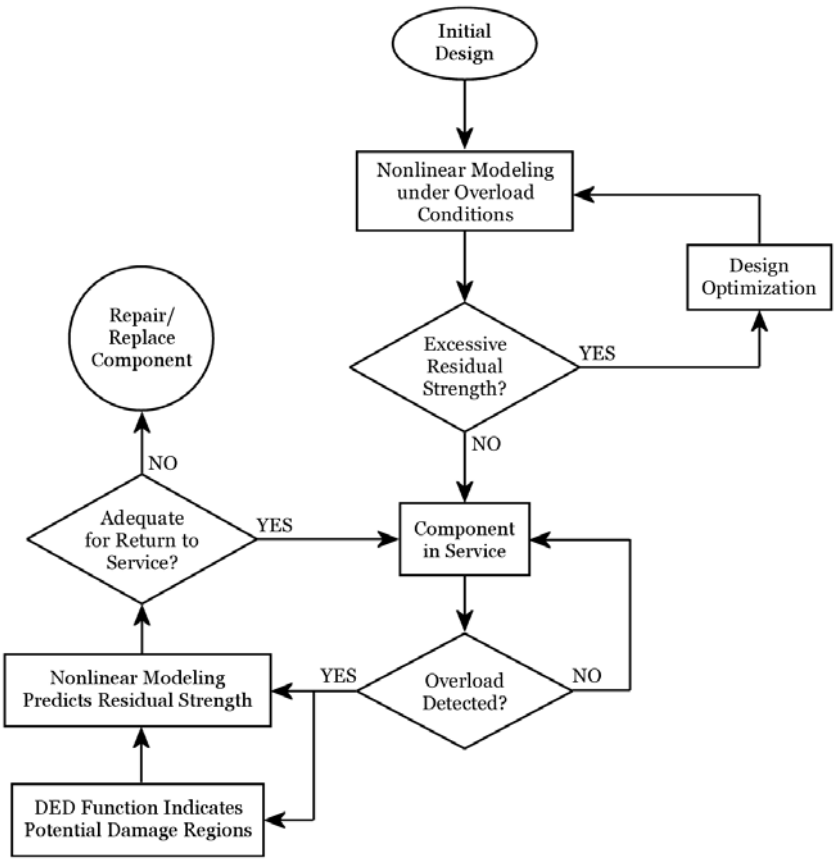

Figure 41. Residual-Strength-Considerate Component Life

The service life of a typical component would follow this sequence:

- Initial Design – Before design, a nonlinear material database is formed using multiaxial testing.

- Nonlinear Modeling and Design Optimization – Using the elastic parameters and post-damage response from the database, the component is optimized to minimize overdesign.
- Component in Service – Embedded sensors monitor the service loads of the component while remaining especially vigilant for overloads.
- DED Function and Post-Damage Analysis – The DED function predicts which sections of the component were most vulnerable to damage, and the residual strength of those components is predicted through nonlinear modeling.
- Repair/Retirement – Based on the calculated residual strength and other inspection of the damaged component, a decision would need to be made regarding its continued service.

REFERENCES CITED

[1] Strong, A. Brent. "History of Composite Materials." July 2002. Brigham Young University. 14 Jan 2008 <http://www.et.byu.edu/groups/strong/pages/articles/articles/history.pdf>

[2] Day, Dwayne A. “Composites and Advanced Materials.” U.S. Centennial of Flight Commission. 24 Sep 2008 <http://www.centennialofflight.gov/essay/Evolution_of_Technology/composites/Tech40.htm>

[3] Tomblin, John, Sam Bloomfield, and Lamia Salah. “Aging of Composite Aircraft Structures.” 7 Feb 2006. NetComposites. 24 Sep 2008 <http://www.netcomposites.com/news.asp?3830>

[4] Quilter, Adam. “Composites in Aerospace Applications.” IHS, Inc. 24 Sep 2008 <http://engineers.ihs.com/NR/rdonlyres/AEF9A38E-56C3-4264-980C-D8D6980A4C84/0/444.pdf>

[5] “787 Dreamliner Background.” 2008. Boeing. 24 Sep 2008 <http://www.boeing.com/commercial/787family/background.html>

[6] “Aircraft Museum—de Havilland Comet.” 21 Aug 2005. Aerospaceweb.org. 24 Sep 2008 < http://www.aerospaceweb.org/aircraft/jetliner/comet>

[7] “Handbook for Damage Tolerant Design.” 11 Dec 2002. Air Force Research Laboratory. 9 Apr 2008 <http://www.siresearch.info/projects/dtdh/index.php>

[8] Ritter, William Joseph. “Application of Energy Methods to Modeling Failures in Composite Materials and Structures.” Diss. Montana State University, 2004.

[9] “Classical Lamination Theory.” 2008. eFunda. 4 May 2008 <http://www.efunda.com/formulae/solid_mechanics/composites/comp_laminate.cfm>

[10] Jones, Robert M. Mechanics of Composite Materials. Second Edition. New York & London: Brunner-Routledge, 1999.

[11] París, Federico. A Study of Failure Criteria of Fibrous Composite Materials. Joint Institute for the Advancement of Flight Sciences NASA/CR-2001-210661. Hamption: Langley Research Center, 2001.

[12] Cairns, Douglas S., Larry B. Ilcewicz, and Tom Walker. “Far-Field and Near-Field Strain Response of Automated Tow-Placed Laminates to Stress Concentrations.” Composite Engineering Volume 3 #11 (1993): 1087-1097.

[13] Mast, P.W., et al. Experimental Determination of Dissipated Energy Density as a Measure of Strain-Induced Damage in Composites. U.S. Naval Research Laboratory NRL/FR/6383—92-9369. Washington: National Technical Information Service, 1992.

[14] Collett, Aaron Bruce. "A Validation Study of the Montana State University In-Plane Loader." Diss. Montana State University, 2006.

[15] Smith, Jay David. "Internal Damage Characterization for Composite Materials Under Biaxial Loading Configuration." Diss. Montana State University, 2007.

[16] Parker, John Wesley. "Development of a Low Cost Image Correlation System To Obtain Full-Field In-Plane Displacement and Strain Data." Diss. Montana State University, 2008.

[17] "OC Triaxial Fabrics Product Information." Oct 2003. Owens Corning. Publication 57946-D. 22 Sep 2008 <http://www.owenscorningchina.com/upload/File/466671169.pdf>

[18] "EPON Resin 826 Technical Data Sheet." Sep 2005. Hexion Specialty Chemicals, Inc. 22 Sep 2008 < http://www.hexion.com/Products/TechnicalDataSheet.aspx?id=3937>

[19] "EPI-CURE Curing Agent 3234 Technical Data Sheet." 2005. Hexion Specialty Chemicals, Inc. 22 Sep 2008 <http://www.resins.com/resins/am/pdf/sc1674.pdf>

[20] "HexPly 8552 Product Data." Mar 2007. Hexcel Composites. Publication FTA 072b. 11 Oct 2007 < http://www.hexcel.com/NR/rdonlyres/B99A007A-C050-4439-9E59-828F539B03A4/0/HEXPLY85528PPA4.pdf>

[21] Huang, Dongfang, and Douglas S. Cairns. "Constitutive Laws of Composite Materials via Multiaxial Testing and Numerical Optimization." Journal of Reinforced Plastics and Composites 25 (2006): 263-281.

[22] "DOE/MSU Composite Material Fatigue Database." 21 Mar 2008. Montana State University. 12 Aug 2008 <http://www.coe.montana.edu/composites/documents/March 2008 Database17pt0.pdf>

[23] "Design Optimization." ANSYS Theory Reference. Release 11.0 Documentation for ANSYS. SAS IP, Inc., 2007.

[24] Farebrother, R.W. Linear Least Squares Computations. New York & Basel: Marcel Drekker, Inc., 1988.

[25] "Standard Test Method for Bearing Strength of Plastics." Annual Book of ASTM Standards. Volume 8.01 Plastics (I). Designation 953-02. ASTM International, 2007.

[26] Booth, Eric Jason. "Progress and Challenges in Non-Linear Constitutive Modeling for Composite Materials." Montana State University, 2007.

[27] Furukawa, Tomonari, and John G. Michopoulos. "Computational Design of Multiaxial Tests for Anisotropic Material Characterization." International Journal for Numerical Methods in Engineering 74 (2007): 1872-1895.

[28] Lin, Wen-Pin, and Hsuan-Teh Hu. "Nonlinear Analysis of Fiber-Reinforced Composite Laminates Subjected to Uniaxial Tensile Load." Journal of Composite Materials 36 (2002): 1429-1450.

[29] "Damage Evolution and Element Removal for Fiber-Reinforced Composites." ABAQUS Analysis User's Manual. ABAQUS Version 6.5 Documentation. ABAQUS, Inc., 2004.

APPENDICES

APPENDIX A

IM7 8552 TEST DATA AND ANALYSIS

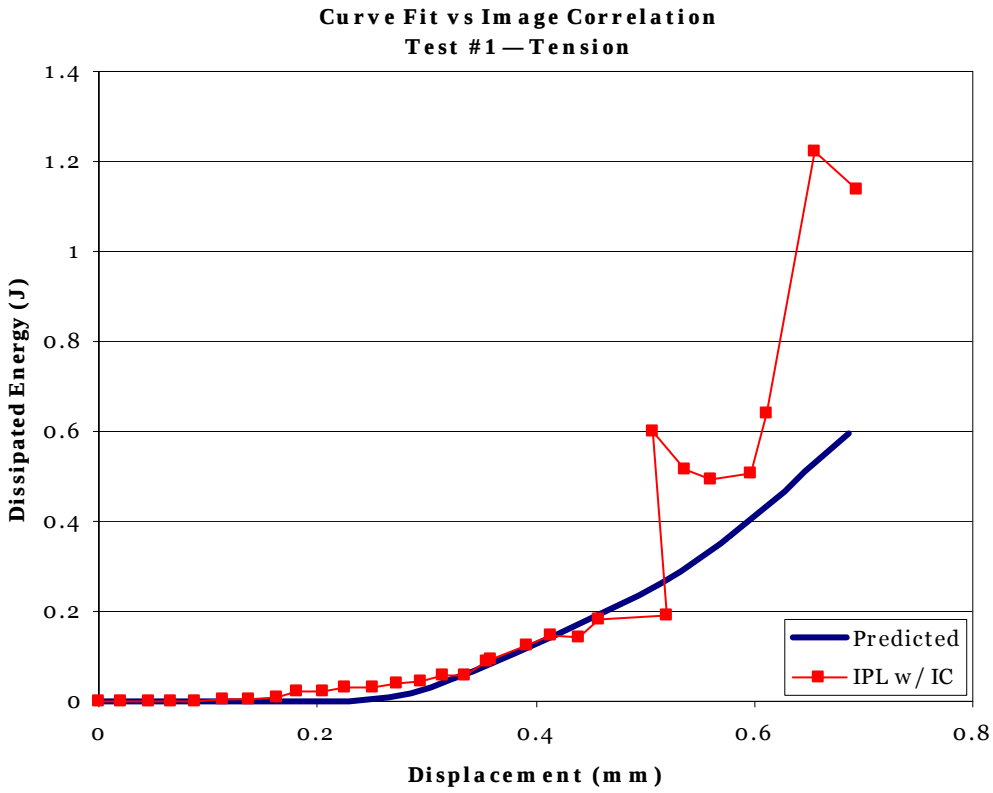
Curve Fit vs Image Correlation
Test #1 — Tension
Dissipated Energy (J)
1.4
1.2
1
0.8
0.6
0.4
0.2
0
0
0.2
0.4
0.6
0.8
Displacement (mm)
Predicted
IPL w/ IC

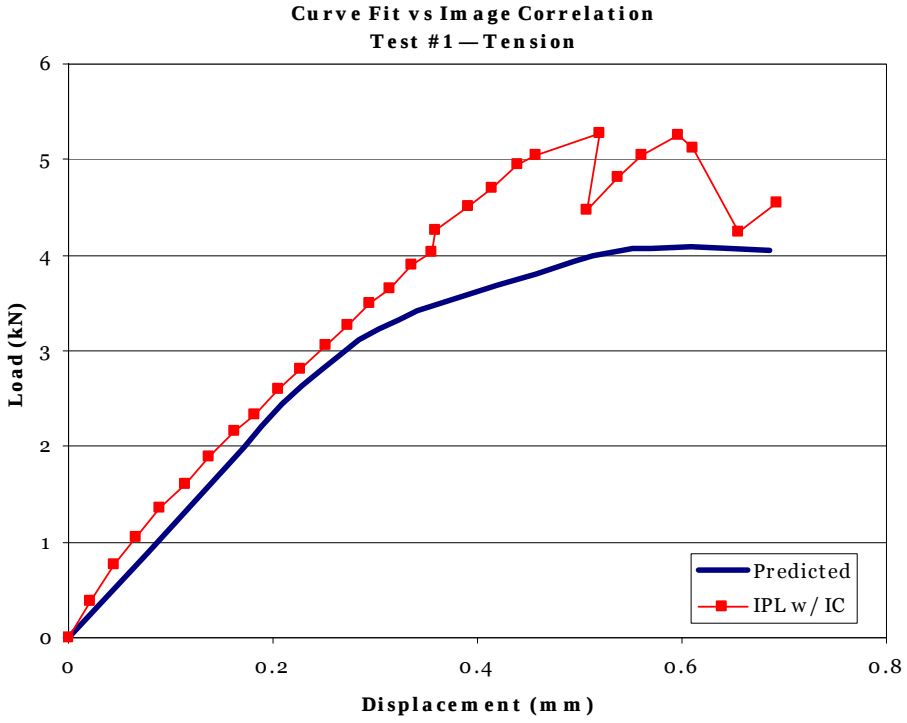
Curve Fit vs Image Correlation
Test #1 — Tension
Load (kN)
6
5
4
3
2
1
0
0
0.2
0.4
0.6
0.8
Displacement (mm)
Predicted
IPL w/ IC

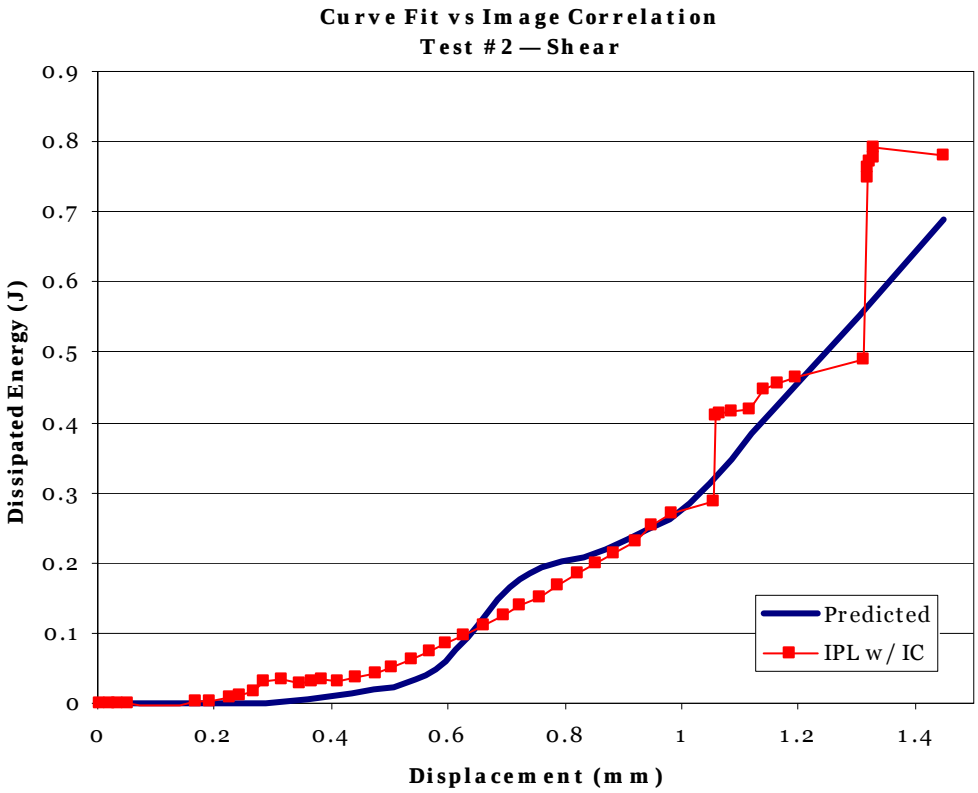
Curve Fit vs Image Correlation
Test #2 — Shear
Dissipated Energy (J)
0.9
0.8
0.7
0.6
0.5
0.4
0.3
0.2
0.1
0
0
0.2
0.4
0.6
0.8
1
1.2
1.4
Displacement (mm)
Predicted
IPL w/ IC

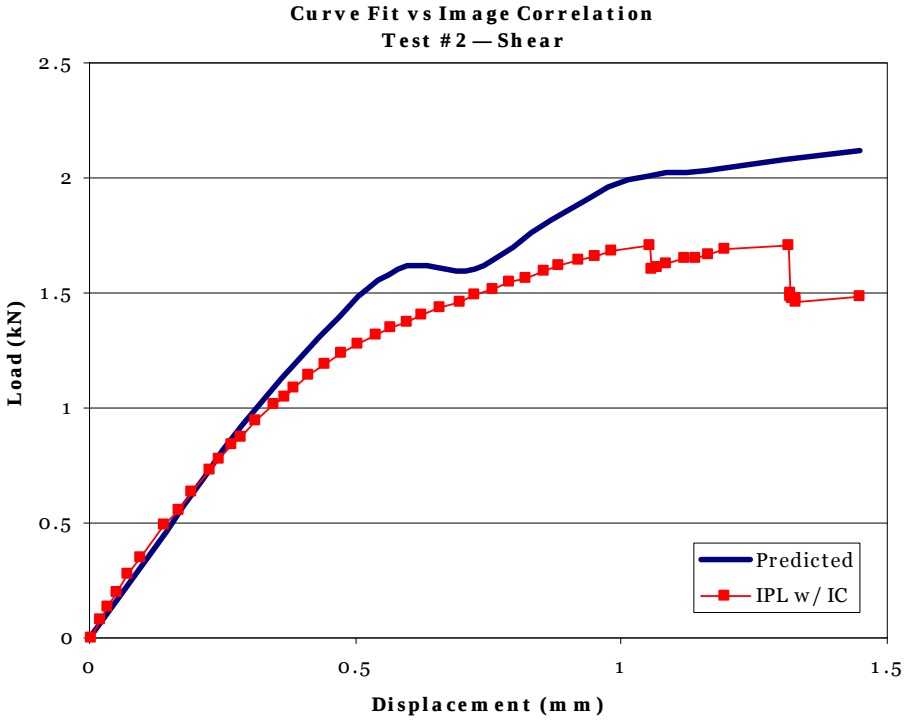
Curve Fit vs Image Correlation
Test #2 — Shear
Load (kN)
2.5
2
1.5
1
0.5
0
0
0.5
1
1.5
Displacement (mm)
Predicted
IPL w/ IC

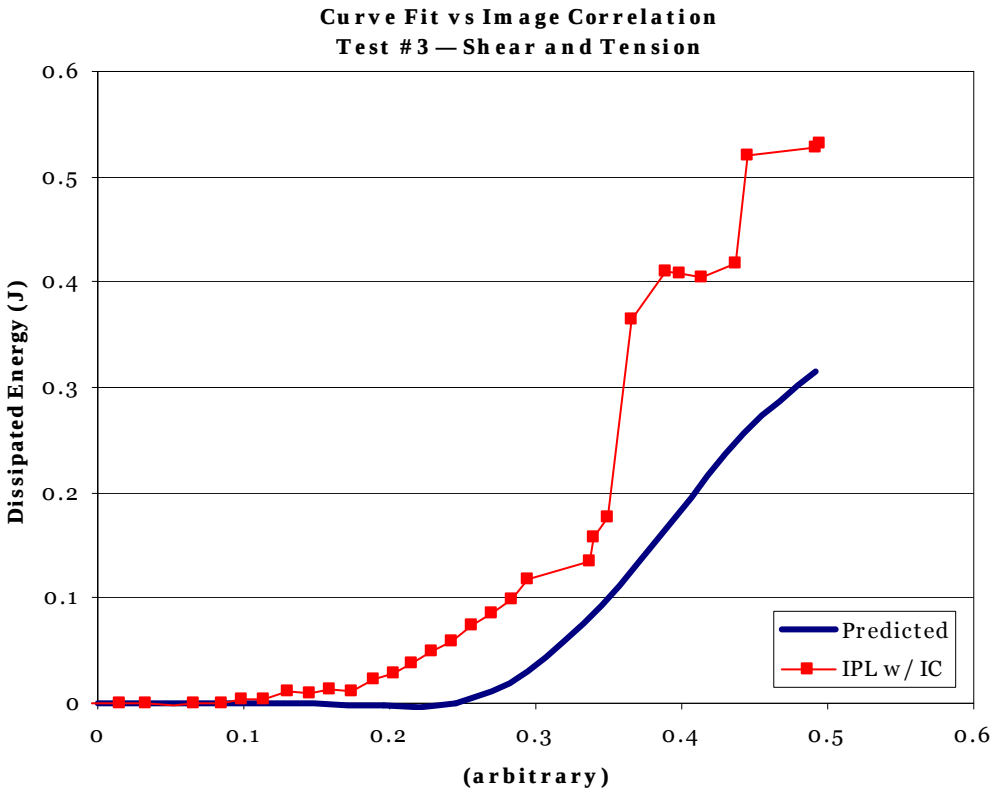
Curve Fit vs Image Correlation
Test #3 — Shear and Tension
Dissipated Energy (J)
0.6
0.5
0.4
0.3
0.2
0.1
0
0
0.1
0.2
0.3
0.4
0.5
0.6
(arbitrary)
Predicted
IPL w/ IC

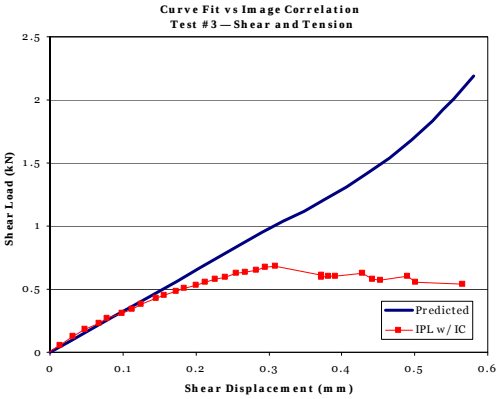
Curve Fit vs Image Correlation
Test #3 — Shear and Tension
Shear Load (kN)
2.5
2
1.5
1
0.5
0
0
0.1
0.2
0.3
0.4
0.5
0.6
Shear Displacement (mm)
Predicted
IPL w/ IC

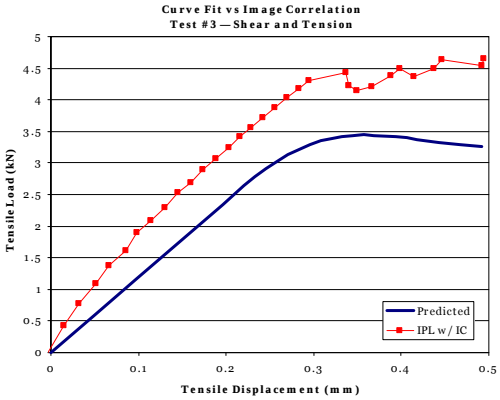
Curve Fit vs Image Correlation
Test #3 — Shear and Tension
Tensile Load (kN)
5
4.5
4
3.5
3
2.5
2
1.5
1
0.5
0
0
0.1
0.2
0.3
0.4
0.5
Tensile Displacement (mm)
Predicted
IPL w/ IC

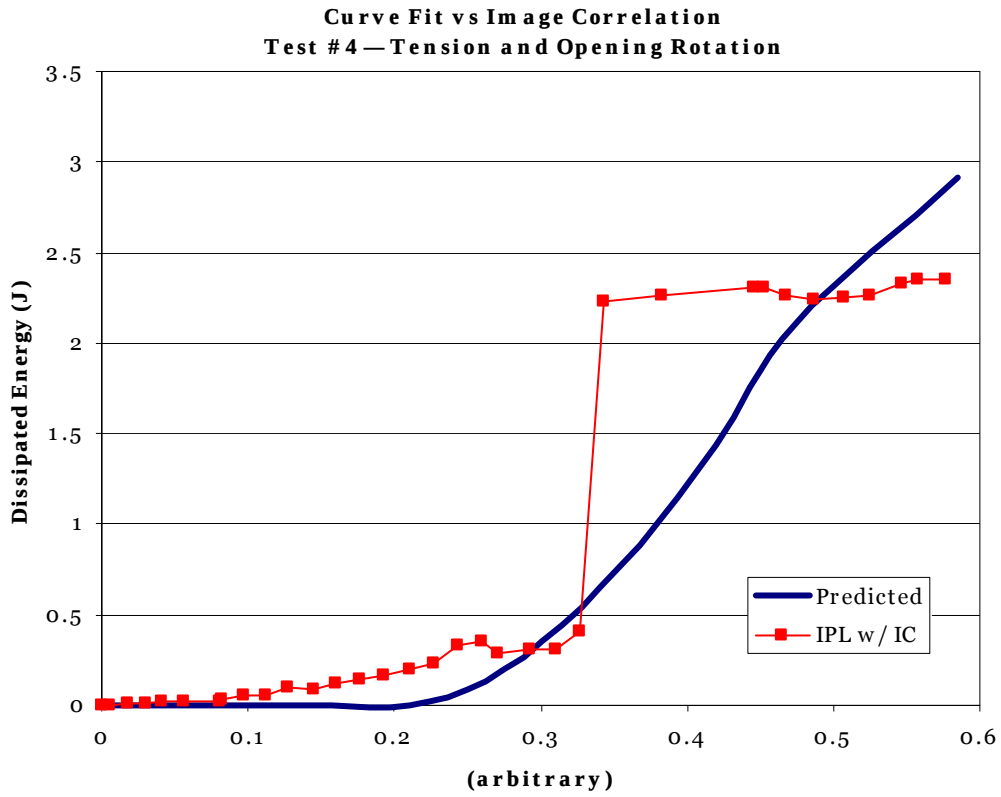
Curve Fit vs Image Correlation
Test #4 — Tension and Opening Rotation
Dissipated Energy (J)
(arbitrary)
Predicted
IPL w / IC
0
0.5
1
1.5
2
2.5
3
3.5
0
0.1
0.2
0.3
0.4
0.5
0.6

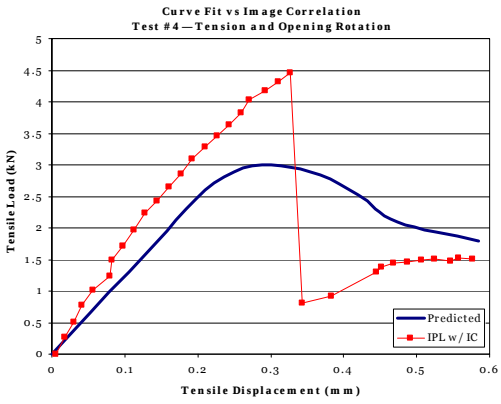
Curve Fit vs Image Correlation
Test #4 — Tension and Opening Rotation
Tensile Load (kN)
Tensile Displacement (mm)
Predicted
IPL w / IC

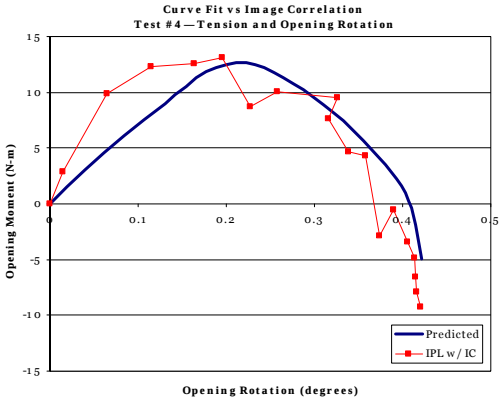
Curve Fit vs Image Correlation
Test #4 — Tension and Opening Rotation
Opening Moment (N-m)
Opening Rotation (degrees)
Predicted
IPL w / IC

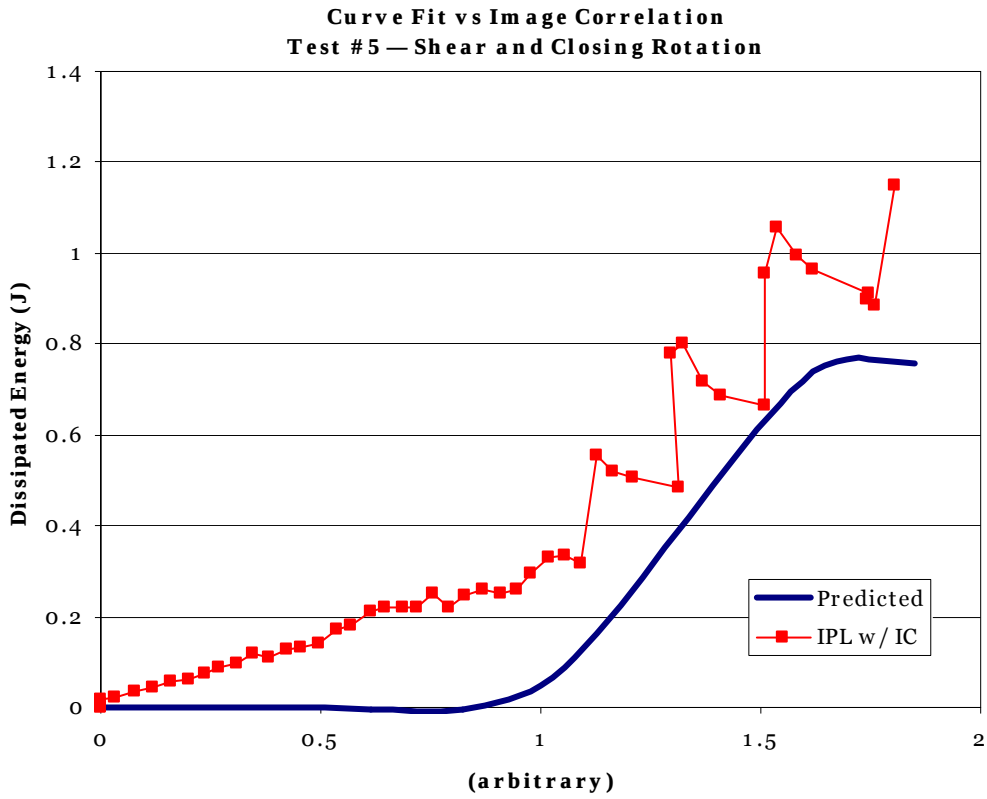
Curve Fit vs Image Correlation
Test #5 — Shear and Closing Rotation
Dissipated Energy (J)
1.4
1.2
1
0.8
0.6
0.4
0.2
0
0
0.5
1
1.5
2
(arbitrary)
Predicted
IPL w/ IC

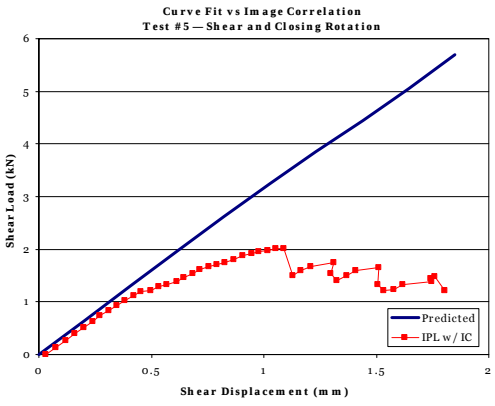
Curve Fit vs Image Correlation
Test #5 — Shear and Closing Rotation
Shear Load (kN)
6
5
4
3
2
1
0
0
0.5
1
1.5
2
Shear Displacement (mm)
Predicted
IPL w/ IC

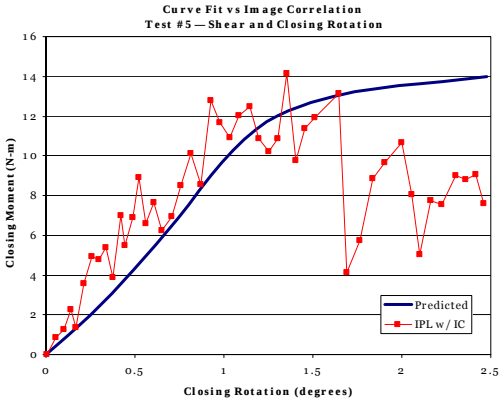
Curve Fit vs Image Correlation
Test #5 — Shear and Closing Rotation
Closing Moment (N-m)
16
14
12
10
8
6
4
2
0
0
0.5
1
1.5
2
2.5
Closing Rotation (degrees)
Predicted
IPL w/ IC

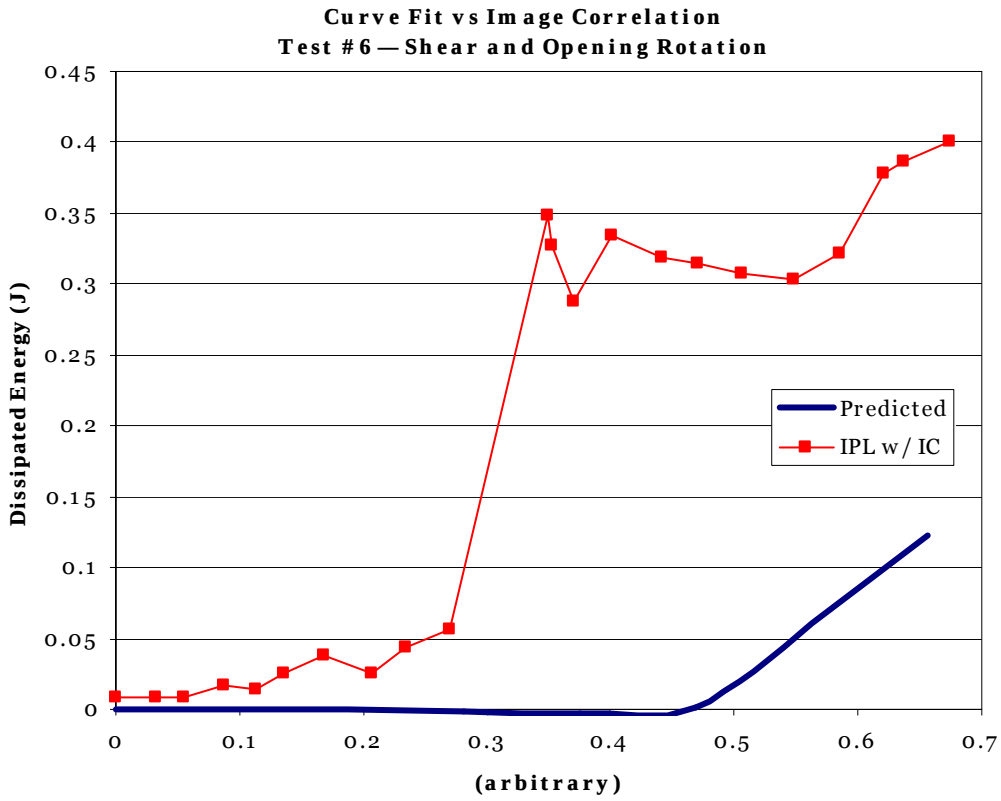
Curve Fit vs Image Correlation
Test #6 — Shear and Opening Rotation
Dissipated Energy (J)
0.45
0.4
0.35
0.3
0.25
0.2
0.15
0.1
0.05
0
0
0.1
0.2
0.3
0.4
0.5
0.6
0.7
(arbitrary)
Predicted
IPL w/ IC

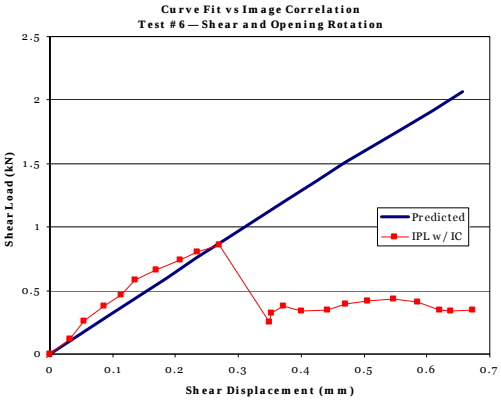
Curve Fit vs Image Correlation
Test #6 — Shear and Opening Rotation
Shear Load (kN)
2.5
2
1.5
1
0.5
0
0
0.1
0.2
0.3
0.4
0.5
0.6
0.7
Shear Displacement (mm)
Predicted
IPL w/ IC

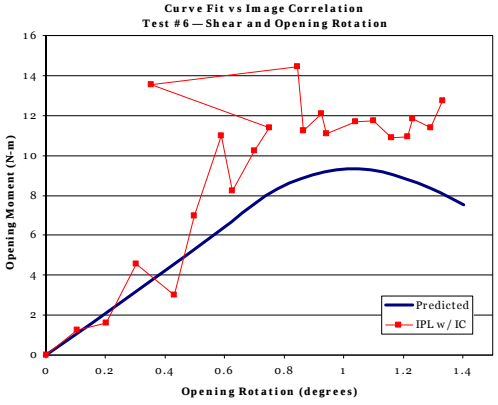
Curve Fit vs Image Correlation
Test #6 — Shear and Opening Rotation
Opening Moment (N-m)
16
14
12
10
8
6
4
2
0
0
0.2
0.4
0.6
0.8
1
1.2
1.4
Opening Rotation (degrees)
Predicted
IPL w/ IC

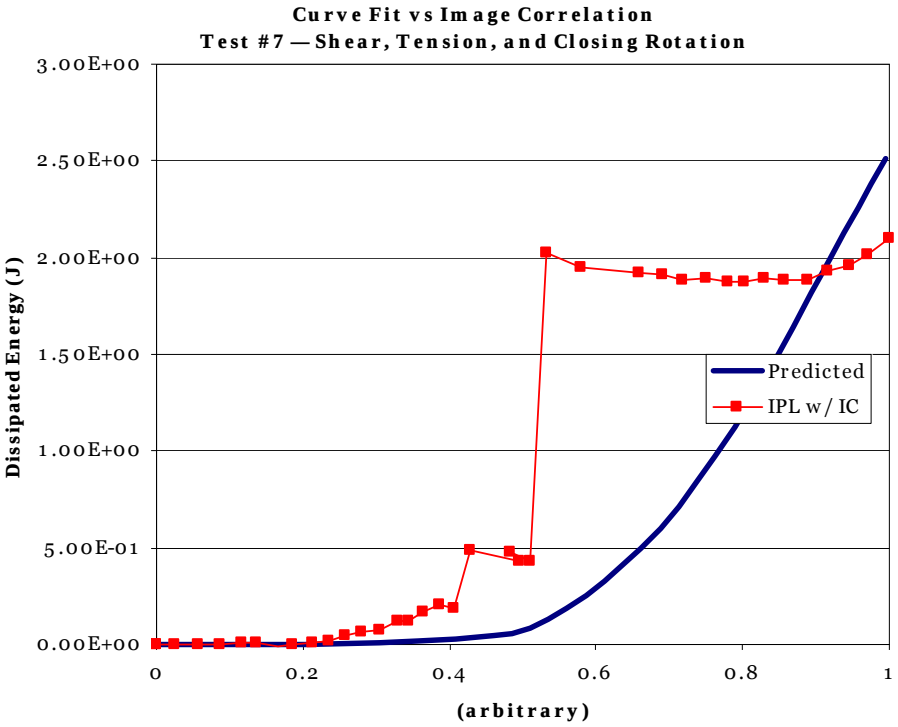
Curve Fit vs Image Correlation
Test #7 — Shear, Tension, and Closing Rotation
Dissipated Energy (J)
3.00E+00
2.50E+00
2.00E+00
1.50E+00
1.00E+00
5.00E-01
0.00E+00
0
0.2
0.4
0.6
0.8
1
(arbitrary)
Predicted
IPL w/ IC

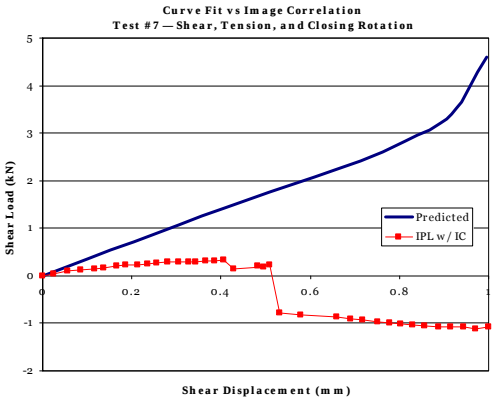
Curve Fit vs Image Correlation
Test #7 — Shear, Tension, and Closing Rotation
Shear Load (kN)
Shear Displacement (mm)
Predicted
IPL w/ IC

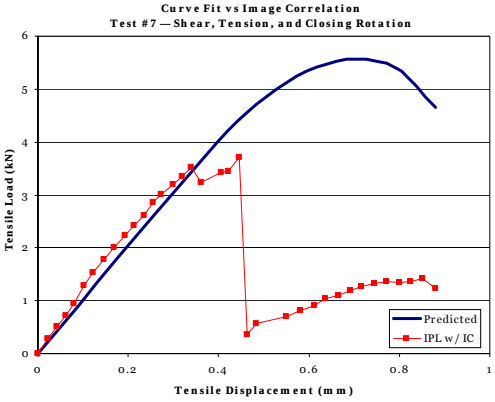
Curve Fit vs Image Correlation
Test #7 — Shear, Tension, and Closing Rotation
Tensile Load (kN)
Tensile Displacement (mm)
Predicted
IPL w/ IC

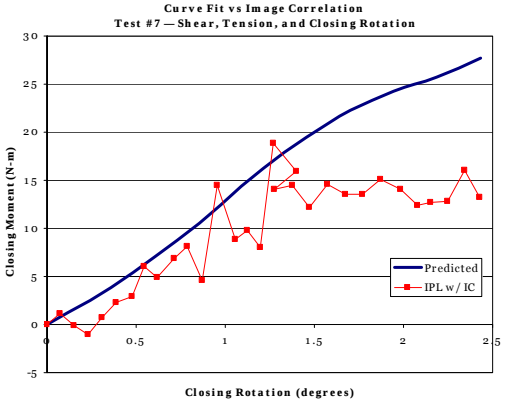
Curve Fit vs Image Correlation
Test #7 — Shear, Tension, and Closing Rotation
Closing Moment (N-m)
Closing Rotation (degrees)
Predicted
IPL w/ IC

APPENDIX B

DED FUNCTION MATLAB FILES

```
%DED_func_symm.m

%Define the total number of load paths.
nl = 17;

%Define minimum total points on all load paths
total_points = 1000;  % off by 3 or 4

%Define the number of plys in the test coupon.
plys = [2 2 2];

%{
Define a vector containing the different ply orientations in IPL
coordinates.
%}
theta_vec_deg = [90 45 -45];

%Get the combined results from the FEA model and IPL data.
global n_elem; global VE; global DET; global u_paths
[epsilon_global,DET,VE,n_elem,u_paths] =
ANSYS_test_proj(nl,total_points);

%Calculate the ply principal strains.
global epsilon_local
[epsilon_local] = Ply_Pricipal_Strain(epsilon_global,theta_vec_deg);

%Calculate the fraction of each ply in the laminate.
global frac_plys
frac_plys = plys/sum(plys);

%Get the extreme strain values to define the solution space.
global Y
index = 0;
for i = 1:size(epsilon_local,1)
    for j = 1:size(epsilon_local,2)
        if ~isempty(epsilon_local{i,j})
            index = index + 1;
            %symm
            epsilon_local{i,j}(:,3,:) = abs(epsilon_local{i,j}(:,3,:));
            Y(index,1) = DET{i,j}(1,1);
            min_cell(index,:,:) = min(epsilon_local{i,j});
            max_cell(index,:,:) = max(epsilon_local{i,j});
            size_A_dim1 = index;
        end
    end
end
global e_max; global e_min
e_min = min(min(min_cell,[],3));
e_max = max(max(max_cell,[],3));

%symm
e_min(3) = 0;
```

```
%Define the number of nodes that span the solution space.
global n_nodes
%symm
n_nodes = [5 5 4];

%Mesh each strain direction with nodes.  Origin is a required node.
global e_mesh

for i = 1:3
    e_mesh{i} = linspace(e_min(i),e_max(i),n_nodes(i));
    if ~((e_min(i) == 0) || (e_max(i) == 0))
        [m,j] = min(abs(e_mesh{i}(2:(end-1))));
        e_mesh{i} = unique([linspace(e_min(i),0,j+1)
linspace(0,e_max(i),n_nodes(i) - j)]);
    end
end

%{
Assemble the element dimensions vector. (Assume each element has the
same dimensions.
%}
global a
a{1} = (e_mesh{1}(2:end) - e_mesh{1}(1:end-1))/2;
a{2} = (e_mesh{2}(2:end) - e_mesh{2}(1:end-1))/2;
a{3} = (e_mesh{3}(2:end) - e_mesh{3}(1:end-1))/2;

%Assemble the local coordinate location vector.
global d
d{1} = (e_mesh{1}(2:end) + e_mesh{1}(1:end-1))/2;
d{2} = (e_mesh{2}(2:end) + e_mesh{2}(1:end-1))/2;
d{3} = (e_mesh{3}(2:end) + e_mesh{3}(1:end-1))/2;

%Define the global node numbers.
global global_nodes
for i = 1:length(n_nodes)
    for k = 1:(n_nodes(i)-1)
        global_nodes{i}(k,:) = cat(2,k,k+1);
    end
end

%Define the linear interpolation functions.
Nm =@(Xi) (1/8)*(1+Xi(1))*(1+Xi(2))*(1-Xi(3));
Nn =@(Xi) (1/8)*(1-Xi(1))*(1+Xi(2))*(1-Xi(3));
No =@(Xi) (1/8)*(1+Xi(1))*(1-Xi(2))*(1-Xi(3));
Np =@(Xi) (1/8)*(1-Xi(1))*(1-Xi(2))*(1-Xi(3));

Nq =@(Xi) (1/8)*(1+Xi(1))*(1+Xi(2))*(1+Xi(3));
Nr =@(Xi) (1/8)*(1-Xi(1))*(1+Xi(2))*(1+Xi(3));
Ns =@(Xi) (1/8)*(1+Xi(1))*(1-Xi(2))*(1+Xi(3));
Nt =@(Xi) (1/8)*(1-Xi(1))*(1-Xi(2))*(1+Xi(3));
```

```
%Define a strain tolerance for the extreme interpolation nodes.
global epsilon
epsilon = 1e-5;

%Define a function handle to calculate the local coordinate index.
loc_coord_index =@(t1,t2,t3) t1+(n_nodes(1)-1)*(t2-1)+(n_nodes(1)-
1)*(n_nodes(2)-1)*(t3-1);

%Define a function handle to calculate the global node number.
g_node =@(t1,t2,t3) t1+n_nodes(1)*(t2-1)+n_nodes(1)*n_nodes(2)*(t3-1);

times(1) = toc;

tic
A = zeros(size_A_dim1,prod(n_nodes));
global loc_coord
kdx = 0;
jdx = 0;
%Build the set of equations to solve.
for j = 1:size(epsilon_local,1)       %load paths
    for m = 1:size(epsilon_local,2)       %points on load path
        if ~isempty(epsilon_local{j,m})
            jdx = jdx + 1;
            temp_A = zeros(1,prod(n_nodes));
            for k = 1:n_elem      %elements
                for i = 1:length(plys)        %plys

                    kdx = kdx+1;

                    %Define an arbitraty x point in the solution space.
                    x0 = epsilon_local{j,m}(k,:,i);

                    %Compute the local coordinate indices.
                    i0 = loc_index_new(x0);

%!!!!!!!!!!!!!!!!!!!!!!!!!!!!!!!!!!!!!!!!!!!!!!!!!!!!!!!!!!!!!!!!!!!!!!!

                    %Calculate the correct local coordinates.
                    under = find(epsilon > abs(x0 - e_min));
                    over = find(epsilon > abs(x0 - e_max));
                    inside = setdiff(1:3,[under over]);

                    Xi(under) = -1;
                    Xi(over) = 1;
                    for mdx = inside
                        Xi(mdx) = (x0(mdx) -
d{mdx}(i0(mdx)))/a{mdx}(i0(mdx));
                    end;
                    if ~isempty(find((abs(Xi) - 1) > epsilon))
                        display('Incorrect local coordinate system is
selected, out of bounds.')
                        return
```

```
                    end

%!!!!!!!!!!!!!!!!!!!!!!!!!!!!!!!!!!!!!!!!!!!!!!!!!!!!!!!!!!!!!!!!!!!!!!!!

                    N = zeros(1,prod(n_nodes));

                    %Determine n and m in global node numbers.
                    q1 = global_nodes{1}(i0(1),1);
                    q2 = global_nodes{1}(i0(1),2);
                    e1 = global_nodes{2}(i0(2),1);
                    e2 = global_nodes{2}(i0(2),2);
                    v1 = global_nodes{3}(i0(3),1);
                    v2 = global_nodes{3}(i0(3),2);

                    g_m = g_node(q2,e2,v1);
                    g_n = g_node(q1,e2,v1);
                    g_o = g_node(q2,e1,v1);
                    g_p = g_node(q1,e1,v1);

                    g_q = g_node(q2,e2,v2);
                    g_r = g_node(q1,e2,v2);
                    g_s = g_node(q2,e1,v2);
                    g_t = g_node(q1,e1,v2);

                    N(g_m) = Nm(Xi);
                    N(g_n) = Nn(Xi);
                    N(g_o) = No(Xi);
                    N(g_p) = Np(Xi);

                    N(g_q) = Nq(Xi);
                    N(g_r) = Nr(Xi);
                    N(g_s) = Ns(Xi);
                    N(g_t) = Nt(Xi);

                    %Build the A matrix.
                    temp_A = temp_A + N*VE{j,m}(k)*frac_plys(i);

                    %Define the element number for each strain point.
                    loc_coord(kdx,1) =
loc_coord_index(i0(1),i0(2),i0(3));
                end
            end
        end
        A(jdx,:) = temp_A;
    end
end
times(2) = toc;

%Select solution technique.
solve_full
%solve_part
```

APPENDIX C

ANSYS OPTIMIZATION BATCH FILES

File Page

opt_nonlin.txt 156
Performs optimization. Establishes initial conditions and constraints.

run_all_nonlin.txt 157
Runs model for all experimental load paths. Sets coupon dimensions and laminate properties. Calculates residuals.

load_data.txt 161
Loads all experimental data. Data files are named test#.csv with three comma-delimited columns for the displacements and a fourth for the total dissipated energy.

geom.txt 162
Builds coupon model.

mesh.txt 164
Meshes coupon model.

pre_info.txt 166
Determines the location of critical nodes and components throughout the model and calculates weighting factors for displacements.

dim.txt 168
Allocates space for array variables needed in the various convergence loops.

elem.txt 169
Initializes element material properties.

sup_strain.txt 170
Finds the strains for each element under reference displacements for use in superposition.

converge.txt 171
Converges on target boundary displacements.

bound_cond.txt 172
Sets displacements of tab edge nodes.

post_info.txt 173
Performs curve fitting to find boundary displacements. Adjusts displacements and loads to coincide with IPL directions.

bilin.txt 176
Enforces bilinear constitutive response on damaged elements.

```
!opt_nonlin.txt

FINISH
/CLEAR
/TITLE, Optimize Nonlinear Properties for IPL Coupon


      EC1 = 0.0156
      EC2 = 0.0091
      EC12 = 0.0176
      EU1 = 0.03
      EU2 = 0.04
      EU12 = 0.04

      /INPUT, RUN_ALL_NONLIN, TXT

/OPT

      OPCLR
      OPANL, RUN_ALL_NONLIN, TXT


      OPVAR, EC1, DV, 0.01, 0.02
      OPVAR, EC2, DV, 0.005, 0.015
      OPVAR, EC12, DV, 0.01, 0.025
      OPVAR, EU1, DV, 0.02, 0.04
      OPVAR, EU2, DV, 0.025, 0.05
      OPVAR, EU12, DV, 0.025, 0.05

      !OPVAR, S1, SV, 0
      !OPVAR, S2, SV, 0
      !OPVAR, S12, SV, 0


      OPVAR, RESEN, OBJ,,, 1    !Residual Dissipated Energy

      OPKEEP, ON                !Save best design
      OPTYPE, SUBP
      OPEXE
      OPLIST, ALL
      PLVAROPT, EC1, EC2, EC12

      PLVAROPT, RESEN
      FINISH

!Plot the best design.

/POST1

RESUME,, BDB
FILE,, BRST
SET
PLNSOL, S, EQV
```

```
!run_all_nonlin.txt

/filename,run_all_nonlin

/plopts,logo,off

/Title, Composite IPL Coupon, Non-linear Material Properties

/prep7

/nerr,,,-1
/uis,msgpop,4

!Load path data.
/input,load_data,txt

pi = 3.1415962

!!!!!!! User defined parameters !!!!!!!!!!!!!!!!!!!!!!!!!!!!!!!!!!!!!!

num_plys = 4

*dim,theta,array,num_plys
theta(1) = 60,-60,-60,60      !deg.

t_layer = 0.031/4         !ply thickness (in)

E1 = 21.2E6             !(psi)
E2 = 1.85E6             !(psi)
E3 = 1E6                !(arbitrary)
G12 = 6.04E5            !(psi)
G13 = 1E6               !(arbitrary)
G23 = 1E6               !(arbitrary)
pr12 = 0.322
pr13 = 0
pr23 = 0

Lpath = 2


!Displacement convergence tolerances.
conv_steps = 8
conv_tol = 0.0001

S1 = EU1 - EC1
S2 = EU2 - EC2
S12 = EU12 - EC12

!Define critical and ultimate strains.
*dim,epsilon_c_initial,array,3
epsilon_c_initial(1) = EC1,EC2,EC12
*dim,epsilon_u_initial,array,3
epsilon_u_initial(1) = EU1,EU2,EU12


!!!!!!!!!!!!!!!!!!!!!!!!!!!!!!!!!!!!!!!!!!!!!!!!!!!!!!!!!!!!!!!!!!!!!!!

/com *** Model parameters ***

l = 1.25          !coupon test length (in)
w = 1.03006       !coupon width (in)
D = 0.2295        !Notch diameter (in)
```

```
n_length = 0.4579 !Notch length (in)

!Define the distance between the coupon notch center and the top grip.
arm = l/2


!Create the model geometry.
/input,geom,txt


!Create the model mesh.
/input,mesh,txt


!Calculate prerequisite information
/input,pre_info,txt


!Dimension the arrays within the do loop.
/input,dim,txt

!!!!!!!!!!!!!!!!!!!!!!!!!!!!!!!!!!!!!!!!!!!!!!!!!!!!!!!!!!!!!!!!!!!!!!!!!!!

!OOO! Model all load paths. !OOO!
!test_data(step,displacement,path)

RESEN = 0

*do,path_num,1,num_paths

      !Initialize element material properties.
      /input,elem,txt

      !Initialize critical/ultimate strains and moduli.
      *do,wdx,1,3
            *do,jdx,1,total_coupon_elem
                  *do,idx,1,num_plys
                        ref_num = idx + num_plys*(jdx-1)
                        epsilon_c(ref_num,wdx) = epsilon_c_initial(wdx)
                        epsilon_u(ref_num,wdx) = epsilon_u_initial(wdx)
                        E_current(ref_num,wdx) = E_initial(wdx)
                  *enddo
            *enddo
      *enddo


      !OOO! Calculate strains for superposition !OOO!
      !strain_sup(load_dir,ref_num,strain_dir)

      ref_disp = 0.1

      load_dir = 1
      target_disp(1) = ref_disp,0,0
      /input,sup_strain,txt

      load_dir = 2
      target_disp(1) = 0,ref_disp,0
      /input,sup_strain,txt

      load_dir = 3
      target_disp(1) = 0,0,ref_disp
      /input,sup_strain,txt
```

```
      !OOO! Check path displacements for damage initiation !OOO!

      undamaged = 1
      step = 0
      *dowhile,undamaged

            step = step + 1

            scale(1) = test_data(step,1,path_num)/ref_disp
            scale(2) = test_data(step,2,path_num)/ref_disp
            scale(3) = test_data(step,3,path_num)/ref_disp

            *do,ref_num,1,total_coupon_elem*num_plys

                  eps(1) = 0,0,0
                  *do,load_dir,1,3
                        eps(1) = eps(1) +
strain_sup(load_dir,ref_num,1)*scale(load_dir)
                        eps(2) = eps(2) +
strain_sup(load_dir,ref_num,2)*scale(load_dir)
                        eps(3) = eps(3) +
strain_sup(load_dir,ref_num,3)*scale(load_dir)
                  *enddo

                  *if,eps(1),abgt,EC1,then
                        undamaged = 0
                        step = step – 1
                  *elseif,eps(2),abgt,EC2,
                        undamaged = 0
                        step = step – 1
                  *elseif,eps(3),abgt,EC12
                        undamaged = 0
                        step = step – 1
                  *endif
            *enddo

            *if,step,eq,path_length(path_num),then
                  undamaged = 0
            *endif
      *enddo

      initiation = max(1,step)


      !OOO! Begin damage evolution !OOO!

      strain_E(1) = 0,0,0
      diss_E(1) = 0,0,0
      old_disp_sqr = 0

      last(1) = 0,0,0,0,0,0

      *do,step,initiation,path_length(path_num)

            disp_sqr = 0
            *do,load_dir,1,3
                  target_disp(load_dir) =
test_data(step,load_dir,path_num)
                  disp_sqr = disp_sqr + target_disp(load_dir)**2
            *enddo
```

```
            !Ignore steps with backtracking.
            *if,disp_sqr,gt,old_disp_sqr,then
                  old_disp_sqr = disp_sqr

                  *if,step,eq,initiation,then
                        *voper,disp,target_disp,mult,model_frac
                  *endif

                  !Iterate until the displacements converge.
                  /input,converge,txt

                  !Check Load step for failure.
                  /input,bilin,txt


                  data_out(step,1) = -disp_x_true
                  data_out(step,2) = -f_x_true
                  data_out(step,3) = disp_y_true
                  data_out(step,4) = f_y_true
                  data_out(step,5) = disp_arc_true
                  data_out(step,6) = moment

                  *do,load_dir,1,3
                        udx = load_dir*2
                        ldx = load_dir*2-1
                        strain_E(load_dir) = strain_E(load_dir) +
(data_out(udx)-last(udx))*(data_out(ldx)+last(ldx))/2

                        diss_E(load_dir) = strain_E(load_dir) -
data_out(udx)*data_out(ldx)/2

                        last(udx) = data_out(udx)
                        last(ldx) = data_out(ldx)
                  *enddo

                  TDE = diss_E(1) + diss_E(2) + diss_E(3)

                  RESEN = RESEN + (TDE - test_data(step,4,path_num))**2
            *endif
      *enddo
*enddo
```

```
!load_data.txt

!Loads Test Data, 3 columns displacement, 1 column TDE
!Files named test#.csv

num_paths = 7

*dim,path_length,array,num_paths

path_length(1) = 33,51,51,36,51,34,44

max_length = 51

*dim,test_data,array,max_length,4,num_paths

*do,eval,1,num_paths
      *vread,test_data(1,1,eval),test%eval%,csv,,jik,4,path_length(eval
)
(E9.4,',',E9.4,',',E9.4,',',E9.4)
*enddo
```

```
!geom.txt

/com *** Define the geometrical keypoints ***

!  #    x                      y
k, 1,   n_length-w,          -l/2
k, 2,   n_length-w,           l/2
k, 3,   n_length,            -l/2
k, 4,   n_length,             l/2
k, 5,   n_length,             D/2
k, 6,   n_length,            -D/2
k, 7,   D/2,                   0
k, 8,   n_length,              0
k, 9,   D/2,                  l/2
k, 10,  D/2,                 -l/2
k, 11,  n_length-w,           0
k, 12,  n_length-w/2,         0
k, 13,  n_length-w/2,         l/2

!Keypoints to make up additional extension tabs.

ext_length = 0.25*l

k, 19,  n_length-w,     l/2+ext_length
k, 20,  n_length-w,     -(l/2+ext_length)
k, 21,  n_length,       l/2+ext_length
k, 22,  n_length,       -(l/2+ext_length)
k, 23,   D/2,           l/2+ext_length
k, 24,   D/2,           -(l/2+ext_length)


/com *** Define coordinate systems ***
cskp,11,1,7,8,9         !Notch centered cylindrical
cskp,12,0,7,8,9         !Notch centered cartesian
cskp,13,0,12,8,13       !Coupon centered cartesian
csys,0                  !Notch tip cartesian

circle,7,D/2,,9,180,4


/com *** Define Lines ***
l,10,18
l,1,17
l,11,16
l,2,15
l,9,14
l,4,5
l,3,6
l,3,10
l,10,1
l,1,11
l,11,2
l,2,9
l,9,4
l,4,5
l,5,14
l,6,18

!Lines to make up additional extension tabs.
l,2,19
l,9,23
l,4,21
```

```
l,19,23
l,23,21

l,3,22
l,10,24
l,1,20
l,20,24
l,24,22

/com *** Define Areas ***

al,7,2,8,15
al,8,1,9,16
al,9,18,10,17
al,6,3,7,14
al,5,4,6,13
al,11,19,5,12

!Areas to make up additional extension tabs.
al,16,21,23,20
al,17,22,24,21
al,13,27,28,26
al,12,26,29,25

/com *** Create Boundary Line Components ***

lsel,s,line,,13
lsel,a,line,,12
cm,bottom_boundary,line
alls

lsel,s,line,,16
lsel,a,line,,17
cm,top_boundary,line
alls

lsel,s,line,,28
lsel,a,line,,29
cm,tab_bottom_boundary,line
alls

lsel,s,line,,23
lsel,a,line,,24
cm,tab_top_boundary,line
alls
```

```
!mesh.txt

/com *** Define the mesh spacing ***

et,1,shell99,,0
keyopt,1,11,0
keyopt,1,10,1
keyopt,1,8,1


*get,length_13,line,13,leng

e_arc_length = pi*D/8

aspect = 1

ratio_8_6 = aspect*(e_arc_length/length_13)
ratio_7 = aspect*(e_arc_length/length_13)
ratio_9_5_10_11 = aspect*(e_arc_length/length_13)

ratio_18_19_12_17 = 1
ratio_14_15 = 1
ratio_13_16 = 1

ediv_radial = 11
ediv_wing = 6
ediv_out = 5

!Radial Lines
lesize,8,,,ediv_radial,ratio_8_6
lesize,6,,,ediv_radial,ratio_8_6
lesize,7,,,ediv_radial,ratio_7
lesize,5,,,ediv_radial,ratio_9_5_10_11
lesize,9,,,ediv_radial,ratio_9_5_10_11
lesize,10,,,ediv_radial,ratio_9_5_10_11
lesize,11,,,ediv_radial,ratio_9_5_10_11

!Vertical Lines
lesize,14,,,ediv_out,ratio_14_15
lesize,15,,,ediv_out,ratio_14_15

!Horizontal Lines
lesize,13,,,ediv_out,ratio_13_16
lesize,16,,,ediv_out,ratio_13_16
lesize,12,,,ediv_wing,ratio_18_19_12_17
lesize,17,,,ediv_wing,ratio_18_19_12_17
lesize,18,,,ediv_wing,ratio_18_19_12_17
lesize,19,,,ediv_wing,ratio_18_19_12_17

!Circumferential Lines
lesize,1,,,ediv_out
lesize,2,,,ediv_out
lesize,3,,,ediv_out
lesize,4,,,ediv_out

!Tab lines
lesize,20,,,5
lesize,21,,,5
lesize,22,,,5

lesize,25,,,5
lesize,26,,,5
```

```
lesize,27,,,5

lesize,28,,,ediv_out,ratio_13_16
lesize,29,,,ediv_wing,ratio_18_19_12_17
lesize,23,,,ediv_out,ratio_13_16
lesize,24,,,ediv_wing,ratio_18_19_12_17


/com *** Mesh Selected Areas ***

!Mesh the coupon areas.

asel,s,area,,1,6
cm,coupon_area,area

type,ref_num
mat,ref_num
real,ref_num
amesh,all
alls

!Mesh the tab areas.

asel,s,area,,7,10
mshkey,0
amesh,all
alls

!Orient all the element coordinate systems with coordinate system 12.

csys,12
emodif,all,esys,12
csys,13
```

```
!pre_info.txt

/com *** Get model information for data extraction ***


!Get node numbers and x-positions along bottom coupon boundary.
cmsel,s,bottom_boundary,lines
nsll,s,1

*get,num_nodes,node,,count
*get,b_min,node,,num,min

*dim,b_nnum,array,num_nodes
*dim,x_pos,array,num_nodes

b_nnum(1) = b_min
*get,x_pos(1),node,b_min,loc,x
*do,eval,2,num_nodes,1
      b_nnum(eval) = ndnext(b_min)
      *get,x_pos(eval),node,ndnext(b_min),loc,x
      b_min = ndnext(b_min)
*enddo
alls


!Get node numbers along top coupon boundary.
cmsel,s,top_boundary,lines
nsll,s,1

*get,t_min,node,,num,min

*dim,t_nnum,array,num_nodes

t_nnum(1) = t_min
*do,eval,2,num_nodes,1
      t_nnum(eval) = ndnext(t_min)
      t_min = ndnext(t_min)
*enddo
alls


!Sort list of boundary nodes by x-position.
*dim,n_weight,array,num_nodes

*do,eval,1,num_nodes-1
      lowest = eval
      *do,eval2,eval+1,num_nodes
            *if,x_pos(eval2),lt,x_pos(lowest),then
                  lowest = eval2
            *endif
      *enddo
      temp = x_pos(lowest)
      x_pos(lowest) = x_pos(eval)
      x_pos(eval) = temp

      temp = b_nnum(lowest)
      b_nnum(lowest) = b_nnum(eval)
      b_nnum(eval) = temp

      temp = t_nnum(lowest)
      t_nnum(lowest) = t_nnum(eval)
      t_nnum(eval) = temp
```

```
*enddo


!Calculate nodal weights for post_info boundary displacement.
calculation
n_weight(1) = (x_pos(2) - x_pos(1))/2
*do,eval,2,num_nodes-1,1
      n_weight(eval) = (x_pos(eval+1) - x_pos(eval-1))/2
*enddo
n_weight(num_nodes) = (x_pos(num_nodes) - x_pos(num_nodes-1))/2


!Get node numbers and positions along top tab boundary.
cmsel,s,tab_top_boundary,lines
nsll,s,1

*get,tt_min,node,,num,min

*dim,tt_nnum,array,num_nodes_tab

tt_nnum(1) = tt_min
*do,eval,2,num_nodes_tab,1
      tt_nnum(eval) = ndnext(tt_min)
      tt_min = ndnext(tt_min)
*enddo
alls

*dim,tt_xloc,array,num_nodes_tab
*dim,tt_yloc,array,num_nodes_tab

*do,eval,2,num_nodes_tab,1
      tt_xloc(eval) = nx(tt_nnum(eval))
      tt_yloc(eval) = ny(tt_nnum(eval))
*enddo


!Determine the total number of elements in the model.
*get,total_elem,elem,0,count

!Determine the number of elements in the coupon excluding the tabs.
cmsel,s,coupon_area,area
nsla,s,1
esla,s
*get,total_coupon_elem,elem,0,count
*get,max_coupon_elem,elem,0,num,max

!Define the tab model scale factor.
model_frac = (l+2*ext_length)/l
```

```
!dim.txt

/com *** Define the dimensions of parameters within loop ***


!OOO! For main !OOO!

!Set the initial change in displacement to zeros.
*dim,delta_disp,array,3

*dim,E_initial,array,3
E_initial(1) = E1,E2,G12

*dim,epsilon_c,array,total_coupon_elem*num_plys,3
*dim,epsilon_u,array,total_coupon_elem*num_plys,3
*dim,E_current,array,total_coupon_elem*num_plys,3

*dim,strain_sup,array,3,total_coupon_elem*num_plys,3
*dim,eps,array,3
*dim,scale,array,3

*dim,target_disp,array,3
*dim,disp,array,3

*dim,strain_E,array,3
*dim,diss_E,array,3
*dim,last,array,6


*dim,data_out,array,max_length,6


!OOO! For bound_cond !OOO!
n_points = 10
*dim,y_bc_table,table,n_points,1,1,x,,,13
*dim,x_bc_table,table,n_points,1,1,x,,,13


!OOO! For post_info !OOO!
*dim,b_disp_x,array,num_nodes
*dim,b_disp_y,array,num_nodes
*dim,t_disp_x,array,num_nodes
*dim,t_disp_y,array,num_nodes
*dim,t_ave,array,2
*dim,b_ave,array,2
*dim,lsq_mat,array,2,2
*dim,lsq_rhs,array,2
*dim,ms_b,array,2
*dim,center,array,2
*dim,ms_t_rot,array,2
*dim,ms_t_true,array,2
*dim,disp_true,array,2
*dim,rot_true,array,2,2
```

```
!elem.txt

/com *** Define the element type ***

*do,jdx,1,total_elem

      esel,s,elem,,jdx

      r,jdx,num_plys,0

      *do,idx,1,num_plys

            ref_num = idx + num_plys*(jdx-1)

            mp,ex,ref_num,E1
            mp,ey,ref_num,E2
            mp,ez,ref_num,E3
            mp,gxy,ref_num,G12
            mp,gyz,ref_num,G23
            mp,gxz,ref_num,G13
            mp,prxy,ref_num,pr12
            mp,pryz,ref_num,pr23
            mp,prxz,ref_num,pr13

            rmodif,jdx,13+(idx-1)*3,ref_num,theta(idx),t_layer

      *enddo

*enddo

alls
```

```
!sup_strain.txt

!Scale the target displacement for tabs.
*voper,disp,target_disp,mult,model_frac

!Iterate until the desired displacement is equal to the true
displacement.
/input,converge,txt

*do,idx,1,num_plys
      /post1

      layer,idx
      rsys,lsys

      etable,11_strain,epel,x
      etable,22_strain,epel,y
      etable,12_strain,epel,xy

      /solution
      *do,jdx,1,total_coupon_elem
            ref_num = idx + num_plys*(jdx-1)

            *get,strain_sup(load_dir,ref_num,1),etab,1,elem,jdx
            *get,strain_sup(load_dir,ref_num,2),etab,2,elem,jdx
            *get,strain_sup(load_dir,ref_num,3),etab,3,elem,jdx
      *enddo
*enddo
```

```
!converge.txt

delta_disp(1) = 0,0,0
un_conv = 1
count = 0
*dowhile,un_conv
      /prep7

      !Define the change in displacement for a given iteration.
      *voper,delta_disp,delta_disp,mult,model_frac

      !Defines the current model displacements.
      *voper,disp,disp,sub,delta_disp


      !Define the boundary conditions. Requires disp(1..3).
      /input,bound_cond,txt

      /solution
      solve
      finish
      /post1


      !Find the true boundary displacements.
      /input,post_info,txt

      delta_disp(1) = disp_x_true-target_disp(1)
      delta_disp(2) = disp_y_true-target_disp(2)
      delta_disp(3) = disp_arc_true-target_disp(3)

      count = count + 1

      *if,delta_disp(1),ablt,conv_tol,then
            *if,delta_disp(2),ablt,conv_tol,then
                  *if,delta_disp(3),ablt,conv_tol,then
                        un_conv = 0
                  *endif
            *endif
      *endif

      *if,count,gt,conv_steps,then
            un_conv = 0
      *endif
*enddo
```

```
!bound_cond.txt

/com *** Apply the boundary conditions ***

cmsel,s,tab_bottom_boundary,line
dl,all,,ux,0
dl,all,,uy,0
dk,20,uz,0
alls

!Define the length of the top boundary in coordinate system 13.

csys,13
*get,x_kp_19,kp,19,loc,x
*get,x_kp_21,kp,21,loc,x
top_length = x_kp_21-x_kp_19

!Define the number of points to represent the boundary condition.

delta_point = top_length/(n_points-1)

disp_theta = disp(3)/(arm+ext_length)

*do,eval,1,n_points,1
      x_eval = ((eval-1)*delta_point)*(x_kp_21-x_kp_19)+x_kp_19

      !Define the y boundary values.

      y_bc_table(eval,0) = x_eval
      y_bc_table(eval,1) = (l/2+ext_length)*(cos(disp_theta)-1)-
x_eval*sin(disp_theta)+disp(2)

      !Define the x boundary values.

      x_bc_table(eval,0) = ((eval-1)*delta_point)*(x_kp_21-
x_kp_19)+x_kp_19
      x_bc_table(eval,1) =
(l/2+ext_length)*sin(disp_theta)+x_eval*(cos(disp_theta)-1)+disp(1)
*enddo
y_bc_table(0,1) = 1
x_bc_table(0,1) = 1


cmsel,s,tab_top_boundary,line
dl,all,,ux,%x_bc_table%
dl,all,,uy,%y_bc_table%
alls
```

```
!post_info.txt

/com *** Find desired quantities ***

!Select nodes and elements of the coupon.
!cmsel,s,coupon_area,area
!esla
!nsla,s,1
!rsys,0
!/dscale,1
!plesol,epto,y
!alls


!Define arrays of  boundary displacements.
b_ave(1) = 0,0
t_ave(1) = 0,0
*do,eval,1,num_nodes
      b_disp_x(eval) = ux(b_nnum(eval))
      b_disp_y(eval) = uy(b_nnum(eval))
      b_ave(1) = b_ave(1) + b_disp_x(eval)*n_weight(eval)/w
      b_ave(2) = b_ave(2) + b_disp_y(eval)*n_weight(eval)/w

      t_disp_x(eval) = ux(t_nnum(eval))
      t_disp_y(eval) = uy(t_nnum(eval))
      t_ave(1) = t_ave(1) + t_disp_x(eval)*n_weight(eval)/w
      t_ave(2) = t_ave(2) + t_disp_y(eval)*n_weight(eval)/w
*enddo


!Solve for slopes at boundaries using least squares.
lsq_mat(1,1) = 0,0
lsq_mat(1,2) = 0,0
lsq_rhs(1) = 0,0

*do,eval,1,num_nodes
      lsq_mat(1,1) = lsq_mat(1,1) + n_weight(eval)*(x_pos(eval) +
b_disp_x(eval))**2
      lsq_mat(1,2) = lsq_mat(1,2) + n_weight(eval)*(x_pos(eval) +
b_disp_x(eval))
      lsq_mat(2,1) = lsq_mat(2,1) + n_weight(eval)*(x_pos(eval) +
b_disp_x(eval))
      lsq_mat(2,2) = lsq_mat(2,2) + n_weight(eval)

      lsq_rhs(1) = lsq_rhs(1) + (x_pos(eval) +
b_disp_x(eval))*n_weight(eval)*b_disp_y(eval)
      lsq_rhs(2) = lsq_rhs(2) + n_weight(eval)*b_disp_y(eval)
*enddo

determ = lsq_mat(1,1)*lsq_mat(2,2) - lsq_mat(1,2)*lsq_mat(2,1)

b_slope = (lsq_mat(2,2)*lsq_rhs(1) - lsq_mat(1,2)*lsq_rhs(2))/determ

lsq_mat(1,1) = 0,0
lsq_mat(1,2) = 0,0
lsq_rhs(1) = 0,0

*do,eval,1,num_nodes
      lsq_mat(1,1) = lsq_mat(1,1) + n_weight(eval)*(x_pos(eval) +
t_disp_x(eval))**2
      lsq_mat(1,2) = lsq_mat(1,2) + n_weight(eval)*(x_pos(eval) +
t_disp_x(eval))
```

```
      lsq_mat(2,1) = lsq_mat(2,1) + n_weight(eval)*(x_pos(eval) +
t_disp_x(eval))
      lsq_mat(2,2) = lsq_mat(2,2) + n_weight(eval)

      lsq_rhs(1) = lsq_rhs(1) + (x_pos(eval) +
t_disp_x(eval))*n_weight(eval)*t_disp_y(eval)
      lsq_rhs(2) = lsq_rhs(2) + n_weight(eval)*t_disp_y(eval)
*enddo

determ = lsq_mat(1,1)*lsq_mat(2,2) - lsq_mat(1,2)*lsq_mat(2,1)

t_slope = (lsq_mat(2,2)*lsq_rhs(1) - lsq_mat(1,2)*lsq_rhs(2))/determ


!Determine the angular displacement.
theta_t = -atan(t_slope)
theta_b = -atan(b_slope)
disp_theta_true = theta_t-theta_b


!Determine the x and y displacements.
ms_b(1) = b_ave(1)
ms_b(2) = b_ave(2) - l/2

center(1) = ms_b(1)+l/2*sin(theta_b)
center(2) = ms_b(2)+l/2*cos(theta_b)

ms_t_rot(1) = center(1)+l/2*sin(theta_t)
ms_t_rot(2) = center(2)+l/2*cos(theta_t)

ms_t_true(1) = t_ave(1)
ms_t_true(2) = t_ave(2) + l/2

disp_true(1) = ms_t_true(1)-ms_t_rot(1)
disp_true(2) = ms_t_true(2)-ms_t_rot(2)


! Negative accounts for -theta_b rotation
rot_true(1,1) = cos(theta_b),-sin(theta_b)
rot_true(1,2) = sin(theta_b),cos(theta_b)


!Determine x and y displacements parallel and perp. with bottom grip.
disp_x_true = disp_true(1)*rot_true(1,1)+disp_true(2)*rot_true(1,2)
disp_y_true = disp_true(1)*rot_true(2,1)+disp_true(2)*rot_true(2,2)
disp_arc_true = disp_theta_true*arm


!Get the reaction forces.
cmsel,s,tab_bottom_boundary,lines
nsll,s,1

moment = 0
x_force = 0
y_force = 0


!Define an array of bottom boundary displacements.
*do,eval,1,num_nodes_tab,1
      *get,temp_fx,node,tt_nnum(eval),rf,fx
      *get,temp_fy,node,tt_nnum(eval),rf,fy
```

```
      x_force = temp_fx+x_force
      y_force = temp_fy+y_force

      temp_m = -
(tt_xloc(eval)+ux(tt_nnum(eval)))*temp_fy+(tt_yloc(eval)+uy(tt_nnum(eva
l)))*temp_fx

      moment = temp_m+moment

*enddo
alls


!Determine the x and y forces parallel and perp. with bottom grip.
f_x_true = x_force*rot_true(1,1)+y_force*rot_true(1,2)
f_y_true = x_force*rot_true(2,1)+y_force*rot_true(2,2)
```

```
!bilin.txt

! Define minimum modulus as a fraction of original
min_mod = 0.01

*do,idx,1,num_plys
      /post1

      layer,idx
      rsys,lsys

      etable,11_strain,epel,x
      etable,22_strain,epel,y
      etable,12_strain,epel,xy

      /solution
      *do,jdx,1,total_coupon_elem

            ref_num = idx + num_plys*(jdx-1)

            *get,temp_11,etab,1,elem,jdx
            *get,temp_22,etab,2,elem,jdx
            *get,temp_12,etab,3,elem,jdx


            *if,temp_11,abgt,epsilon_c(ref_num,1),then
                  *if,temp_11,ablt,epsilon_u(ref_num,1),then
                        E_current(ref_num,1) =
(E_current(ref_num,1)*epsilon_c(ref_num,1)/abs(temp_11))*(((epsilon_c(r
ef_num,1)-abs(temp_11))/(epsilon_u(ref_num,1)-epsilon_c(ref_num,1)))+1)
                        epsilon_c(ref_num,1) = abs(temp_11)
                  *else
                        E_current(ref_num,1) = min_mod*E1
                  *endif
                  *if,E_current(ref_num,1),lt,min_mod*E1,then
                        E_current(ref_num,1) = min_mod*E1
                  *endif
                  mp,ex,ref_num,E_current(ref_num,1)
            *endif

            *if,temp_22,abgt,epsilon_c(ref_num,2),then
                  *if,temp_22,ablt,epsilon_u(ref_num,2),then
                        E_current(ref_num,2) =
(E_current(ref_num,2)*epsilon_c(ref_num,2)/abs(temp_22))*(((epsilon_c(r
ef_num,2)-abs(temp_22))/(epsilon_u(ref_num,2)-epsilon_c(ref_num,2)))+1)
                        epsilon_c(ref_num,2) = abs(temp_22)
                  *else
                        E_current(ref_num,2) = min_mod*E2
                  *endif
                  *if,E_current(ref_num,2),lt,min_mod*E2,then
                        E_current(ref_num,2) = min_mod*E2
                  *endif
                  mp,ey,ref_num,E_current(ref_num,2)
            *endif

            *if,temp_12,abgt,epsilon_c(ref_num,3),then
                  *if,temp_12,ablt,epsilon_u(ref_num,3),then
                        E_current(ref_num,3) =
(E_current(ref_num,3)*epsilon_c(ref_num,3)/abs(temp_12))*(((epsilon_c(r
ef_num,3)-abs(temp_12))/(epsilon_u(ref_num,3)-epsilon_c(ref_num,3)))+1)
                        epsilon_c(ref_num,3) = abs(temp_12)
                  *else
```

```
                        E_current(ref_num,3) = min_mod*G12
                    *endif
                    *if,E_current(ref_num,3),lt,min_mod*G12,then
                        E_current(ref_num,3) = min_mod*G12
                    *endif
                    mp,gxy,ref_num,E_current(ref_num,3)
                *endif

            *enddo

        *enddo
```